

The Pennsylvania State University
The Graduate School
Department of Electrical Engineering

**RESONANCE RAMAN SPECTROSCOPY IN THE
ULTRAVIOLET USING A TUNABLE LASER**

A Dissertation in
Electrical Engineering

by

Adam H. Willitsford

© 2008 Adam H. Willitsford

Submitted in Partial Fulfillment
of the Requirements
for the Degree of

Doctor of Philosophy

August 2008

The dissertation of Adam H. Willitsford was reviewed and approved* by the following:

C. Russell Philbrick
Professor of Electrical Engineering
Thesis Advisor
Chair of Committee

Stewart Kurtz
Professor of Electrical Engineering

Kultegin Aydin
Professor of Electrical Engineering

Sven G. Bilén
Associate Professor of Electrical Engineering

H. Nels Shirer
Associate Professor of Meteorology

Zhiwen Liu
Assistant Professor of Electrical Engineering

Hans Hallen
Professor of Physics North Carolina State University
Special Member

W. Kenneth Jenkins
Professor of Electrical Engineering
Head of the Department of Electrical Engineering

*Signatures are on file in the Graduate School

ABSTRACT

The characterization of minor atmospheric constituents, such as pollutants, bio-hazards, and other rogue materials has been a difficult task for the research community. Raman scattering techniques have been employed to detect and identify materials in both a laboratory and field settings; however, Raman scattering processes have an extremely small scattering cross section; however, which limits its utility. Through the use of the resonance enhancement it is possible to extend the utility of the Raman scattering technique.

This dissertation presents a novel Raman scattering experiment that was designed and developed in collaboration with the research group of Professor Hans Hallen and performed at The North Carolina State University Optics Lab. Measurements of resonance-enhanced Raman scattering were made on multiple samples. In particular, this dissertation reports an investigation of the phenomenon of resonance-enhanced Raman scattering in two aromatic hydrocarbons: benzene and toluene.

Algorithms were developed for the analysis of the Raman data that included removing the noise background and normalizing data to remove fluctuations in laser power and detector efficiencies. An algorithm for calculating the resonance gain was developed and applied to both benzene and toluene. The resonance-enhanced Raman scatter of benzene and toluene was found to be 100-10,000 \times larger than their normal Raman scattering spectrum when the molecules are excited by radiation at peaks in their respective electronic resonance excitation bands. Further analysis of the resonant Raman spectra of benzene was performed, and the Raman scattered lines

observed were assigned to the modes of vibration. The resultant spectra are in good agreement with the earlier work performed by Zeigler and Hudson[1981] and Asher [1984].

The original goal of the investigation of the resonance enhancement was to seek improved capability for lidar based on the experiments. It can be argued that the absorption of energy in the energetic double bonds of carbon which form the benzene ring can be used for resonance Raman enhanced scatter, and future investigations should result in demonstrations of our ability to remotely detect a number of interesting species.

Several achievements from my research described in this dissertation include:

- 1) A new experiment has investigated resonance-enhanced Raman scattering for the first time using small steps in excitation wavelength [~ 0.12 nm].
- 2) Excitation at wavelengths in the ultraviolet spectrum resulting in resonance-enhanced Raman scattering in both benzene and toluene occur over extremely narrow wavelength bands.
- 3) A high resolution (fine-tuning) of the ultraviolet excitation has been used to investigate the enhancement, and to isolate the gain region for resonance-Raman scattering in benzene.
- 4) The peak resonance enhancement is found to correlate with the vapor-phase absorption peaks of both benzene and toluene, when the experiments were performed in liquid phase.

- 5) The resonance Raman spectra of benzene has been analyzed and vibrational modes associated with the scattering have been assigned.
- 6) An algorithm is described for use in the analysis of the Raman spectra, including noise removal and normalization corrections for source and detector wavelength dependence, and it is applied in analyzing the data collected.
- 7) An algorithm was developed for the calculation of the resonance enhancement to determine the gain factor for the resonance Raman scattered signals.

TABLE OF CONTENTS

LIST OF FIGURES	xi
LIST OF TABLES	xvi
ACKNOWLEDGEMENTS	xviii
CHAPTER 1: Introduction.....	1
1.1 Goals and Current Work.....	3
1.2 Outline of Research Accomplishments and Hypothesis.....	4
CHAPTER 2: A Historical Perspective	6
CHAPTER 3: Optical Scattering	13
3.1 C.V. Raman and Raman Scattering.....	15
3.1.1 Stokes and Anti-Stokes Raman Scattering.....	16
3.1.2 Vibrational Raman Spectral ‘Fingerprints’.....	18
3.1.3 Rotational Raman Scattering.....	20
3.2 Coherent Anti-Stokes Raman Spectroscopy.....	22
3.2.1 Pump, Probe, 4-wave mixing.....	23
3.2.2 White Light Laser (Stokes Probe).....	24
3.3 Fluorescence.....	25
3.4 Resonance Raman Scattering.....	27
3.5 Lidar.....	29
3.5.1 Lidar Fundamentals.....	30
3.5.2 LAPS.....	30
3.7 Summary.....	32

CHAPTER 4: Theory of Resonance Enhanced Raman Scattering.....	34
4.1 Classical Light Scattering – Dipole Scattering.....	34
4.1.1 Rayleigh and Raman Scatter.....	35
4.2 Infrared Active and Raman Active Selection Rules.....	38
4.3 Dirac Notation – Bra-Ket Operators.....	38
4.4 Quantum Mechanical Treatment of Dipole Scattering.....	39
4.5 Theory of Resonant Enhanced Raman Scattering.....	40
4.6 Qualitative Description of the A and B Terms for Resonant Raman Scattering.....	44
4.7 Summary.....	47
 CHAPTER 5: Raman and Resonance Enhanced Raman Spectroscopy: The Experimental Setup.....	 49
5.1 Resonance Enhancement.....	50
5.2 Experimental Setup Overview.....	51
5.2.1 Laser Excitation.....	52
5.2.2 Optical Scattering Arrangement.....	59
5.2.3 Spectrometer Basics.....	62
5.2.4 Jobin Yvon Spex Triplemate 1877.....	63
5.2.5 CCD Camera.....	67
5.2.6 Spectrometer Calibration (Mercury Lamp).....	68
5.2.7 Sample Holder.....	71
5.2.8 Sample Handling and Preparation.....	73

5.3 Summary.....	75
CHAPTER 6: Raman Data Processing: Noise Removal and Data Normalization.....	77
6.1 Preliminary Data Processing – Noise Removal	77
6.2 Signal Averaging.....	79
6.3 Complete Raman Spectrum Presentation.....	80
6.4 Normalization of Raman Data.....	82
6.5 Summary.....	84
CHAPTER 7: Raman Data Processing: Resonance Absorption Correction and Gain Calculation.....	86
7.1 Absorption Correction for Resonance Raman Spectra.....	87
7.1.1 Absorption Correction for Benzene.....	88
7.1.1.1 Gas Phase Absorption Correction for Benzene.....	89
7.1.1.2 Liquid Phase Absorption Correction for Benzene.....	97
7.1.2 Absorption Correction for Toluene.....	99
7.1.2.1 Gas Phase Absorption Correction for Toluene.....	99
7.1.2.2 Liquid Phase Absorption Correction for Toluene....	102
7.2 Peak Fitting.....	104
7.3 Benzene Resonance Raman Final Gain Figure.....	112
7.4 Summary.....	113
CHAPTER 8: Resonance Raman Spectra.....	115
8.1 Benzene Vibrational Raman Modes.....	116

8.2 Benzene Resonance Raman Spectra.....	120
8.2.1 Concentration Effects.....	126
8.2.2 Theoretical Mechanism of Scattering in Benzene $^1B_{2u}$ Region.....	128
8.2.3 Comparison of Resonant Raman Spectra of Benzene.....	129
8.3 Toluene Raman Scatter.....	130
8.3.1 Resonance Enhanced Raman Scattering in Toluene.....	132
8.4 Summary.....	134
CHAPTER 9: Summary, Conclusions, and Future Work.....	135
9.1 Summary.....	135
9.2 Conclusions.....	137
9.3 Future Work.....	138
REFERENCES.....	141
APPENDIX A: Picture of C.V. Raman.....	163
APPENDIX B: Characteristic Raman Scattering Frequencies.....	164
APPENDIX C: Ultraviolet (200 nm – 400 nm) – Mercury Vapor Emission Lines and Relative Intensities.....	166
APPENDIX D: UV Excitation Laser – Optical Parametric Oscillator.....	167
APPENDIX E: Teflon Sample Holders for 90^0 Raman Scattering Experiment.....	170
APPENDIX F: MATLAB code for corrections and Noise Reduction.....	174

APPENDIX G: MATLAB Code for the reading, normalization, and stitching of multiple files	179
APPENDIX H: Etzkorn absorption Spectra of Benzene from the MPI-Mainz Spectral Atlas.....	190
APPENDIX I: Etzkorn absorption Spectra of Toluene from the MPI-Mainz Spectral Atlas.....	191
APPENDIX J: MATLAB code for absorption correction and gain calculation.....	192
APPENDIX K: Comparison of Herzberg and Wilson vibrational mode labels.....	200

LIST OF FIGURES

Figure 3.1. Rainbow (contributed by David Willitsford).....	14
Figure 3.2. Left: Sundog (New Ulm, MN., Erik Axdahl) Right: Green Flash (San Francisco, CA., Mila Zincova)	14
Figure 3.3. Optical scattering, v_0 is the ground state, v_e is the vibrationally excited state, and Δv is the energy of the scattered photon. [Inaba, 1976].....	17
Figure 3.4. Vibrational Raman Shift Q-branch [Inaba, 1976].....	19
Figure 3.5. Vibrational and Rotational Energy diagram.....	20
Figure 3.6. Rotational Raman lines for Oxygen and Nitrogen at 200K.....	21
Figure 3.7. Rotational Raman lines for Oxygen and Nitrogen at 300K.....	22
Figure 3.8. Coherent anti-Stokes Raman Spectroscopy.....	24
Figure 3.9. Dispersion of the supercontinuum white light laser in the Ultra-fast Optics Lab at Penn State University.....	25
Figure 3.10. Broadband emission due to fluorescence, S_0 is ground state and S_1 is the excited state.....	27
Figure 3.11. Optical Scattering Mechanisms [Inaba, 1975].....	28
Figure 3.12. Lidar Atmospheric Profile Sensor (LAPS) at Penn State University.....	32
Figure 4.1. Four conditions for A-term scattering [After Clark and Dines, 1986; Long, 2001].....	46
Figure 5.1. Excitation Laser arrangement for Raman Scattering Setup [Chawick, 2008]	54
Figure 5.2. OPO Cavity at North Carolina State University laboratory.....	55
Figure 5.3. OPO Schematic.....	55
Figure 5.4. OPO Laser output from the North Carolina State University, approximate wavelength range shown 420-710 nm (white center portions due to saturation of digital camera).....	57

Figure 5.5. Typical β -BBO Transmission Curve.....	58
Figure 5.6. OPO Laser Linewidth at 240 nm.....	58
Figure 5.7. Arrangement of the 90° Raman scattering setup with 430 nm excitation.	60
Figure 5.8. Optical Scattering Schematic [Chadwick, 2008].....	61
Figure 5.9. Reflection type diffraction grating.....	62
Figure 5.10. Filter stage of Triple Spex 1877.....	64
Figure 5.11. Spectrometer stage of Triple Spex 1877.....	65
Figure 5.12. Triple Spex 1877 overall throughput efficiency [Chadwick, 2008]....	67
Figure 5.13. Andor Ixon EM-CCD quantum efficiency.....	68
Figure 5.14. Mercury Vapor Lamp Spectra 2400gr/mm Triple Spex Spectrometer...	69
Figure 5.15. Rough diamond for calibration, color observed is due to fluorescence..	70
Figure 5.16. Raman scatter from diamond with 260 nm excitation.....	70
Figure 5.17. Sample holders: Open back, Teflon stopper removed (left), dual windowed (right).....	71
Figure 5.18. Raman spectra of Teflon as collected in Raleigh (Top), and a comparison to the Raman spectra of Teflon collected by Sedlacek <i>et al.</i> , 2001 (bottom).....	72
Figure 5.19. Teflon sample holder in 90° scattering configuration (left) and absorption measurement configuration (right).....	73
Figure 5.20 Molecular structure of benzene, toluene and naphthalene.....	75
Figure 6.1. Raw camera image of liquid benzene Raman scatter with ‘meteors’	78
Figure 6.2. Processed camera image of liquid benzene Raman scatter with ‘meteors’ removed.....	79
Figure 6.3. Vertical average of CCD image with ‘meteors’ removed.....	80
Figure 6.4. The full Raman spectra of benzene using 259 nm (resonance) excitation	82

Figure 7.1. Benzene absorption cross section Etzkorn [1999].....	90
Figure 7.2. Absorption on the laser of excitation.....	91
Figure 7.3. Absorption on the Raman scattered signal.....	91
Figure 7.4. Absorption loss for a molecule at a distance of X from the laser entry point.....	92
Figure 7.5. Benzene resonance Raman spectra.....	96
Figure 7.6. Resonance Raman scatter as seen in Figure 7.5, with absorption Correction.....	96
Figure 7.7. Liquid benzene absorption [Du <i>et al.</i> , 1998, Inagaki, 1972, API 1970]..	97
Figure 7.8. Toluene vapor-phase absorption cross section Etzkorn [1999].....	100
Figure 7.9. Liquid toluene absorption in cyclohexane [Friedel <i>et al.</i> , 1951].....	102
Figure 7.10. Fityk (258.88 nm) original data.....	105
Figure 7.11. Fityk multi-point spline background removal for 258.88 nm excitation.	107
Figure 7.12. Fityk background removal and peak fits for 258.88 nm excitation.....	107
Figure 7.13. Gaussian fit to 258.88 nm (resonance) Raman data using Fityk.....	108
Figure 7.14. Raman scatter from 258.88nm (blue) with full-width at half-maximum (red) from original data for each Raman line.....	110
Figure 7.15. Gaussian fit to 430 nm (non-resonant) Raman data using Fityk.....	111
Figure 7.16. Raman scatter from 430 nm (blue) with full-width at half-maximum (red) from original data.....	112
Figure 8.1. Benzene Raman spectra with 488 nm excitation http://riodb01.ibase.aist.go.jp/sdbs/ (National Institute of Advanced Industrial Science and Technology, 10/11/2006)	119
Figure 8.2. High resolution vapor-phase absorption spectra ${}^1B_{2u}$ band (blue, [Etzkorn, 1999], and laser excitation wavelengths (red).....	120
Figure 8.3. Benzene resonant and non-resonant Raman comparison.....	122

Figure 8.4. Resonant Raman spectra of benzene for nine different wavelengths of excitation 258–260 nm.....	123
Figure 8.5. Resonance-Raman spectrum of benzene.....	124
Figure 8.6. Resonance enhanced Raman spectra around 247.2 nm.....	125
Figure 8.7. Resonance enhanced Raman spectra around 253 nm.....	126
Figure 8.8. Concentration effects on Raman scattered intensity for resonance excitation.....	127
Figure 8.9. Concentration effects on Raman scattered intensity for visible Excitation.....	127
Figure 8.10. Benzene Raman spectra 354.7 nm excitation (Top) and 212.8 nm Excitation (Bottom) dotted lines are spectra due to the solvent acetonitrile. (The original plot has been changed to reflect the naming convention of Herzberg) [Ziegler and Hudson, 1981].....	130
Figure 8.11. Toluene Raman spectra with 488 nm excitation.....	131
Figure 8.12. Toluene Raman spectra with 514.4 nm excitation.....	131
Figure 8.13. Toluene Raman spectra for excitation wavelengths around 266.83 nm	132
Figure 8.14. Resonance enhanced Raman scattering in toluene.....	133
Figure A.1. C.V. Raman and first Raman Spectra.....	163
Figure D.1. Overall Schematic of UV excitation Laser [Chadwick, 2008].....	168
Figure D.2. Spectra Physics Nd:YAG laser with 2 nd and 3 rd harmonic generator.....	168
Figure D.3. Optical Parametric Oscillator cavity and tunable 2 nd harmonic generator.....	169
Figure D.4. Pellin-Broca prism.....	169
Figure E.1. Teflon sample holder for 90° scattering and absorption measurements.....	170
Figure E.2. Teflon sample holder for 90 ⁰ scattering measurements.....	171

Figure E.3. Breakdown of Teflon sample holder (Quartz windows, Teflon O-rings, Teflon container, and Teflon end caps.....	171
Figure E.4. Close-up of Teflon sample holder with Teflon coated O-ring.....	172
Figure E.5. Close-up of 90 ⁰ scattering holder with aluminum foil surround and Teflon stopper removed.....	172
Figure E.6. Teflon holder with stopper.....	173

LIST OF TABLES

Table 3.1. Raman Spectral Range.....	20
Table 3.2. Optical scattering cross sections, Inaba [1975].....	29
Table 4.1. Summary of Raman and resonant Raman scattering [Smith and Dent, 2005].....	48
Table 5.1. Harmonic generation wavelengths of the Nd:YAG laser.....	52
Table 5.2. Phase matching angle of the optical parametric oscillator.....	53
Table 5.3. Spectrometer Operating Range.....	66
Table 5.4. UV cut-off wavelengths for common solvents.....	75
Table 7.1. Raman peak parameters from Fityk for peaks shown in Figure 7.13.....	109
Table 7.2. Raman peak parameters from MATLAB for peaks shown in Figure 7.14.....	110
Table 7.3. Raman peak parameters from Fityk for peaks shown in Figure 7.15.....	111
Table 7.4. Raman peak parameters from Fityk for peaks shown in Figure 7.16.....	112
Table 8.1. Benzene normal vibrational modes (3N-6, totaling 30) from www.chem.purdue.edu/ghelp/vibs/c6h6.html	117
Table 8.2. Herzberg and Wilson mode assignment comparison.....	118
Table 8.3. Benzene vibrational modes using Herzberg notation.....	119
Table 8.4. Resonant Raman modes in benzene for Figure 8.3.....	121
Table 8.5. Benzene experimental concentration.....	126
Table B.1. Characteristic Raman Group Frequencies.....	164
Table C.1. Mercury Vapor Lamp Emission Spectra.....	166
Table H.1. Benzene Vapor Phase Absorption Cross Section.....	190
Table I.1. Toluene Vapor Phase Absorption Cross Section.....	191

Table J.1. Toluene Vapor Phase Absorption Cross Section.....	192
Table K.1. Benzene mode assignment comparison of Wilson and Herzberg.....	200

ACKNOWLEDGMENTS

Thank you to all the faculty, friends, and family members who have helped me to complete not only this dissertation but another step in my lifelong learning process. Each deserves thanks:

Thank you to my thesis advisor C. Russell Philbrick. Dr. Philbrick has been a wonderful mentor, role model, and friend throughout my graduate career. Dr. Philbrick has taught me to “paint the picture” and see the forest for the trees without losing track of the details. I am forever grateful for the experience and diverse opportunities that I was afforded while working with Dr. Philbrick. The knowledge, skills, and thoughtfulness that he has imparted to me will be forever cherished.

Thank you to Dr. Hans Hallen of the North Carolina State University Physics Department. During the experimental portion of my dissertation, I worked hand-in-hand with the Optics Lab at NC State. I was welcomed with open arms into Dr. Hallen’s lab and found I quickly felt like a member of the “Wolf Pack”. Dr. Hallen quickly became another mentor and friend whose knowledge in optics, mechanics, and experimental design were paramount.

Thank you to Dr. Stewart Kurtz for his ever-present optimism and excitement. It was his passion for the study of benzene that moved my experiments forward. I had limited success with water as a resonant material, and Dr. Kurtz urged me to characterize benzene, the results of which are detailed in this dissertation. His wealth of knowledge on benzene and its structure have proven to be of great help.

Thank you to Todd Chadwick, the only other person who truly understands the trials and tribulations of using a tunable OPO. During my time at NC State, Todd and I worked extensively to create a novel and successful resonance experiment. He and I spent many, many long hours in the lab aligning, tweaking, breaking, building, and reconstructing various portions of the resonance Raman experiment. The opportunity to bounce ideas and thoughts off of Todd was of incalculable value. Todd is a brilliant physicist who understands hard work as well as the need for stress relief. The nightly exercise, be it at the gym or on the tennis court was a wonderful respite from the laboratory atmosphere. His friendship became a shining light during the dissertation process.

Thank you to the members of the Penn State University Lidar Lab. Thanks to Dave Brown for his continued hard work and friendship throughout our time together at Penn State. Also thanks to the other members of the PSU Lidar lab: Joe Begnoché, Jason Collier, Perry Edwards, Guangkun (Homer) Li, Jin Park, Sameer Unni, Sachin Verghese, and Andrea Wyant.

Thank you to the members of the North Carolina State University Optics Lab who helped me to feel at home during my visit. Special thanks to Ryan Neely for his friendship, computer expertise, and electrical wiring prowess. Thank you also to Robert Daniels for making me feel at home in North Carolina.

Thank you to the members of my Ph.D. committee for their constructive criticism and feedback: Dr. C. Russell Philbrick, Dr. Hans Hallen, Dr. Stewart Kurtz, Dr. Kultegin Aydin, Dr. Sven Bilén, Dr. Zhiwen Liu, Dr. Nels Shirer, and Dr. Kenneth Jenkins.

Thank you to Michigan Aerospace Corporation for their generous loan of the EMCCD camera. Thank you to Diane Knight for loaning us the diamond that was so important during the calibration of the experiment.

Thank you to Dr. Craig Bohren of Penn State and Dr. Sanford Asher of the University of Pittsburgh, and Dr. Arthur Sedlacek of Brookhaven National Lab, for their constructive input and feedback during the investigation.

Thank you to my all my 'gym buddies' for their inspiration and perspiration during the many needed hours of stress relief. Also thank you to my good friend Cory Smith, with whom I have spent many hours both in the gym and on the running road sharing ideas, thoughts, and stories.

Thank you to all my friends at Centre Soccer with whom I enjoyed hours and hours of fun on and off the field, giving me a much needed break from what they have dubbed the "Laserology" lab. Thank you to Mike Renz for your friendship and generosity, and for always keeping me honest and humble.

Thank you to Dr. Neil and Marlene Stringer who have provided me with continued support and encouragement throughout my time at Penn State. They have been a wonderful source of knowledge and experience that has helped me to grow and learn. Thank you to Marlene for your help with editing many of my writings. Thank you to my sisters-in-law, Elizabeth and Katharine Stringer, who exude laughter and love. Thank you to my brother-in-law, Daniel Stringer, for his support, friendship, and grilling mastery.

Thank you to my brother, Noah Willitsford, for the love and support he has given me throughout my life. From the time we were kids it was always wonderful to have a partner-in-crime; I could not have asked for a better brother.

Special thanks to my parents, Mr. David and Brenda Willitsford, who have provided me with continuous love, support, and encouragement throughout my life. They have given me everything that I could ever need to succeed and I am forever in their debt.

Special thanks to my wife, Abigail Stringer, who has made my life complete. She has been the proverbial light at the end of the tunnel, supporting me, loving me, and helping me in every aspect of my graduate career. She has shown me the meaning of hard work, and I have done my best to emulate her work ethic during this journey.

Chapter 1: Introduction

The need for improved techniques for measuring chemical species has never been more pronounced. The problems in need of attention include monitoring air pollutants, obtaining additional evidence for global warming, measuring toxins, detecting and measuring chemical-biological agents, and finding explosive materials due to the threat of international terrorism.

Improvements also are needed for the measurements and studies of greenhouse gas pollutants. These gases are found most commonly in small concentrations, which are either spread throughout the atmosphere in the case of pollutants, or are found in low concentrations around a small source such as an explosive material or toxic chemical. Detection, identification, and quantification of trace constituents spread throughout the atmosphere are posing a challenge to the research community. Currently, point measurements from balloon sondes and ground-based systems provide high quality measurements of the local atmosphere; they are poor in spatial and temporal resolution however.

Lidar has made it possible to measure and analyze the atmospheric constituents with increased spatial and temporal resolution [Alpers *et al.*, 2004; Inaba, 1976; Kobayasi and Inaba, 1970; Measures, 1991; Penney, 1974; Philbrick, 1985; Rosen, 1975; Sedlacek 1995]. Lidar has limitations because it employs Raman scattering for the detection and identification of atmospheric constituents. Although Raman scattering has been used routinely to detect, identify, and quantify molecular concentrations in both laboratory and field settings, the extremely small scattering

cross sections associated with the Raman signals limit the measurements to relatively large concentrations of molecules. It is even more difficult to remotely detect and measure unknown chemical species located at significant ranges. Background optical signals in the atmosphere, such as scattered sunlight, also limit the detection. Lidar techniques are often used to detect remotely major atmospheric constituents using their backscattered Raman signal because of the uniqueness of the spectral signature representing each molecular species. In order to extend the utility of lidar remote sensing, a means to enhance the extremely small Raman scattering signals is needed. Some common solutions include simply using more powerful laser transmitters, larger telescope receivers, narrower band filters, and more sensitive detectors; all of these improvements have the capability to enhance the signal-to-noise ratio. There are limits as to how far each technological improvement can be taken however. Another means to enhance the signal-to-noise ratio may be found in using resonance enhancements to increase the Raman scattered signal.

With the advent of more powerful and lower cost tunable ultraviolet sources, it is now possible to consider using the resonance Raman effect on a more routine basis. The resonant enhancement of the scattering intensity occurs as the excitation frequency approaches the energy corresponding to an electronic state of a molecule. This phenomenon has been found to enhance the Raman scattering cross section between 3 and 8 orders of magnitude [Chamberlain *et al.*, 1976]. The increase in sensitivity occurs because of the stronger coupling of optical energy into the molecular vibrational modes. With this increase in Raman scattered signal, it may become possible to detect and quantify significantly smaller concentrations of

chemical and biological species as well as trace pollutants, bio-contaminants, and explosives.

1.1 Goals and Current Work

The primary goal of this thesis is to extend the knowledge and database of the resonant-enhanced Raman scattering effect, so that the technique can be developed for laser standoff detection (lidar) in future measurements of hazardous materials. The work performed in this dissertation finds new features in the resonance enhanced Raman scatter of both benzene and toluene. The enhancement is unique within its extremely narrow enhanced excitation bandwidth of less than 1 nm. This measurement is achieved using the fine-tuning capability of an Optical Parametric Oscillator (OPO) that has a continuous tuning range through the ultraviolet electronic absorption bands between 230 and 300 nm of both benzene and toluene. In most resonance Raman studies, only a few discreet excitation wavelengths are typically chosen, and these are widely separated in significantly large steps (5 nm - 20 nm) [Ziegler, 1980, 1981, 1983; Asher, 1984, 1988, 1993; Gerrity *et al.*, 1985; Sedlacek, 1995]. The large steps in excitation wavelength result from using several common UV laser wavelengths that are readily available. These studies commonly make a point of comparing off-resonance Raman scatter (typically in the visible wavelength region) to near-resonance Raman scatter (typically in the UV wavelength region). Very few studies have actually matched the absorption peak in the molecule of interest; therefore, most investigations never obtain a measure of the resonance

enhancement, but merely a measure of the pre-resonance enhanced Raman scatter signal.

Our investigations using an OPO make it possible to tune the laser with sequential steps as small as 0.12 nm. This fine tuning of the laser center wavelength make it possible to study extremely small changes in excitation wavelength affecting the Raman scatter. Both benzene and toluene exhibited an enhancement in Raman scattered signals on the order of 100 to 10,000 \times , and the enhancement peak occurred within a narrow range of excitation wavelengths of ± 0.25 nm.

1.2 Outline of Research Accomplishments and Hypothesis

My research work has explored the processes and properties of several interesting molecules to understand the characteristics of the resonance Raman technique. The hypotheses examined in this dissertation are that:

- 1) The characteristics of the molecular structure, for example the carbon ring, result in a distinct resonance enhancement of Raman scatter associated with the peaks in the absorption spectrum.
- 2) The resonance enhanced Raman spectra couples significant energy into a number of overtones and combination modes, and additional energy levels are observed in the resonance Raman scattered spectra.
- 3) Resonance enhanced Raman scattering exhibits a significant increase in the amplitude of spectral features representing the energy states that uniquely identify the molecule. At low concentrations the Raman scattering signal

may be detectable with resonance excitation in the ultraviolet region where absorption is strong.

The primary accomplishments of the research are to:

- 1) Investigate the processes and properties of the phenomena of pre-resonance and resonance enhanced Raman scatter in two aromatic hydrocarbons: benzene and toluene.
- 2) Calculate the resonance enhancement gain in the Raman scattered intensity for benzene and toluene.
- 3) Describe the effects of the resonance enhancement of the Raman spectrum by investigating additional spectral features, including combination and overtones were identified for benzene.

Chapter 2: A Historical Perspective

Shortly after C.V. Raman's 1928 discovery of the process that we today call Raman scattering [Raman, 1928], Synge proposed the initial concept of optical remote sensing in 1930. He suggested that atmospheric density measurements could be made by observing the optical scattering produced by a search light [Synge, 1930]. Until this point, upper atmospheric soundings were performed primarily through the use of balloon observations. Balloon soundings above 50 km are not feasible, and the only alternative was the use of rockets [Synge, 1930]. In 1951, Elterman put Synge's idea to the test, and performed quantitative measurements of the stratospheric density with a searchlight [Elterman, 1951]. By using a shutter mechanism, Elterman was able to create a method for pulsing light that provided distinction between the transmitted and backscattered light which used a bistatic arrangement that pointed the receiving telescope along the beam to assign range values based on geometry. The concepts of using lasers to generate Raman scattering and the 'searchlight' technique are combined into current use of Raman lidars.

With the first demonstration of the laser in 1960, Theodore Maiman introduced a new tool for research to scientists around the world [Maiman, 1960]. Maiman's demonstration was the stimulated emission from a ruby crystal 1 cm in length and coated with silver on two parallel faces. Ruby absorbs the green, blue, and ultraviolet energy from a high-power flash-lamp and excites the ruby into a relatively long lifetime metastable state, which then decays as a red (694.3 nm) phosphorescent emission. The initial spontaneous emission spawns the stimulated emission of a powerful, nearly

monochromatic output at 694.3 nm along the axis established by the cavity gain; thus the laser was born.

Lasers have become well known and widely used in many areas because they provide a high-power controllable light transmitter. Lasers, which have a divergence of one milliradian or less, are significantly more collimated than the best search light (typically 0.1 radian divergence), and allow large power densities to be transmitted over longer ranges. In 1962, Smullin and Fiocco used a ruby laser to measure optical scattering from the moon, thereby demonstrating the capability of both the laser and detection optics of that time [Smullin and Fiocco, 1962]. Following their experiments using “moon echoes”, they made measurements of scattering layers in the upper atmosphere [Smullin and Fiocco, 1963]. In 1964, Collis and Ligda performed backscattering measurements over the San Francisco Bay, where even during clear-sky conditions it was possible to distinguish areas aerosol scattering [Collis and Ligda, 1964]. The first work focused on elastic, or Rayleigh, scattering where the wavelength transmitted equals the wavelength received. Leonard performed the first lidar measurements of the Raman scattering from atmospheric molecular nitrogen and oxygen using a pulsed nitrogen laser at 337.1 nm, and analyzed the Raman scattered returns using a tunable filter with a bandwidth of 3.5 nm [Leonard, 1967]. This measurement was a great step forward because of the species’ unique scattering wavelength; however, the Raman scattering-cross section is typically three orders of magnitude weaker than the Rayleigh-scattered component. A year later, measurements of atmospheric density with greatly improved accuracy were performed using the Raman return signal of nitrogen [Cooney, 1968].

By the early 1970s, the future of laser remote sensing measurements for the atmospheric monitoring of pollutants was developing. Inaba and Kobayasi [1970], Hirshfeld *et al.*, [1972], Melfi and McCormick [1969, 1972] and Penney *et al.* [1974], had each performed their own experiments looking at water vapor, carbon dioxide, carbon monoxide, sulfur dioxide, and molecular nitrogen (N₂) and oxygen (O₂). Melfi and McCormick [1969] made measurements of water vapor by using a frequency-doubled ruby laser output from an ADP (ammonium di-hydrogen phosphate) crystal. By simultaneously measuring the atmospheric nitrogen and water vapor Raman signals, Melfi and McCormick obtained a measurement of the water vapor mixing ratio. Inaba and Kobayasi [1970] probed smoke plumes created by the burning of paraffin oil. With the smoke plume present, they identified the presence of both sulfur dioxide and carbon monoxide at a range of 20 m. Hirschfeld [1972] examined the means of improving the signal-to-noise ratio by taking advantage of the wavelength dependence of Raman scattering (λ^{-4}), as well as by using higher efficiency detectors and better filters for rejection of scattered signals from the fundamental laser wavelength. Hirschfeld [1972] was able to detect CO₂, SO₂, and water vapor at varying ranges and number densities in full daylight conditions. This work showed, for the first time, the experimental capability of Raman lidar to detect and quantify trace atmospheric pollutants in broad daylight. Penney *et al.*, [1974] made measurements of the absolute Raman scattering cross sections of N₂, O₂, and CO₂. In addition, they made observations of the temperature dependence of the rotational Raman scattering spectra, which today are used as a method to retrieve atmospheric temperature profiles.

Following these early experiments, many researchers [Poultney *et al.* 1977; Inaba 1976; and many others] continued to improve Raman lidar, making it possible to remotely detect a large array of chemicals and species in the atmosphere. Raman scattering provides a reliable ability to uniquely identify molecules. However, its very small scattering cross section decreases its utility with increased range and for small concentrations of the species. Therefore, in order to detect remotely small concentrations, it is necessary to find methods for increasing the signal. There are a number of ways to improve the detection of smaller quantities of chemical species with hardware improvements, or with other techniques such as fluorescence detection, Differential Absorption Lidar (DIAL), and resonance-enhanced Raman scattering.

We focus our efforts on the resonance-Raman technique that was demonstrated more than 60 years ago [Shorygin, 1947]. When the wavelength of optical excitation is tuned near an electronic absorption band, an increase in the Raman scattering efficiency is possible. Shorygin [1947] observed a resonance enhancement of Raman scattering through the use of mercury arc lamp radiation. Behringer and Brandmüller [1956] continued extensive studies of resonance Raman scattering into the mid 1950s. Laser developments in the early 1960s made it possible to probe molecular structures with a nearly monochromatic source, thus alleviating problems associated with wideband sources that mask Raman signals.

During the 1970s, Penney and Morey [1973] as well as Chamberlain *et al.* [1976], Rosen *et al.*, [1975] performed resonant Raman experiments on SO₂ and NO₂, and they demonstrated 3 to 5 orders of magnitude increase in Raman scattering compared with that of the background molecular nitrogen. These results pointed to the possibility of utilizing

Raman lidar as a means for detecting smaller concentrations of common air pollutants. Although the number densities of SO₂ and NO₂ were in the 1 to 100 ppm range, it was still feasible to detect them using the large increase in Raman scattering intensity from the resonant enhancement [Chamberlain *et al.*, 1975]. Hirschfeld *et al.* [1972] successfully detected SO₂ (30 ppm) in field experiments that examined plumes from smokestacks at a range of 200 m, and demonstrated this capability of the Raman lidar. Ziegler and Albrecht [1978] went on to perform the first measurements of the pre-resonant Raman scattering effects in benzene derivatives (e.g., benzene and toluene) and pioneered this work in organic chemistry. They followed that work with a resonance-enhanced Raman scatter measurements of benzene, utilizing the deep ultraviolet excitation at 212.8 nm (5th harmonic Nd:YAG) [Ziegler and Albrecht, 1980]. Their research revealed strong resonant spectra with many combination modes and overtones present in the spectra.

Resonance fluorescence measurements of upper atmospheric sodium [Gardner *et al.*, 1988] were used to study the upper mesopause wave structure and temperature. The technique was extended to astronomy for atmospheric turbulence compensation by making use of the development of a solid state laser at 589 nm that coincided with electronic absorption of sodium [Philbrick *et al.*, 1985]. Clark and Dines [1986] made a comprehensive analysis of resonance Raman scattering and extended the work by detailing the theory of resonance-enhanced Raman scattering. Asher *et al.* [1993] used a new CW (continuous wave) laser source which —maintained hundreds of milliwatts of power in the deep UV at 257 nm, 248 nm, 244 nm, 238 nm and 228.9 nm— to study the resonance Raman process. This new CW laser source is ideal for Raman spectroscopy

because it avoids nonlinear and saturation problems that occur in materials when high peak intensity is used for excitation. By 1994, Sedlacek *et al.* [1994] created a resonance Raman lidar capable of detecting and measuring SO₂ pollutants in a plume at a range of 500 m, and demonstrated that it was possible to detect concentrations of 70 ppm-m with integration times as short as seven seconds.

With the development of several Raman lidars at Penn State University during the 1990s, a technique for measuring and analyzing ozone with sensitivity to a few parts per billion (ppb) level was developed [Esposito and Philbrick, 1998]. This high sensitivity resulted from using the Raman scattered signals of the fourth harmonic Nd:YAG laser (266 nm) from the atmospheric molecular nitrogen and oxygen, which coincidentally lie on the steep side of the Hartley absorption band in ozone. These signals provide a direct DIAL (Differential Absorption Lidar) measurement to retrieve profiles of ozone concentrations greater than about 10 parts per billion [Esposito and Philbrick, 1998]. This technique relies on the fact that the O₂-to-N₂ ratio in the atmosphere is stable to one part in 10⁵, and only the absorption of ozone makes any substantial change in the measured ratio. Temperature measurements from 1 to 105 km have been demonstrated by combining Rayleigh and Raman scattering measurements in the lower region 1 to 80 km with resonance fluorescence of free metal atoms in the 80 to 105 km altitude region by using the Doppler width of the fluorescence returns [Alpers *et al.* 2004].

Resonance-enhanced Raman scattering is proposed as a likely solution to push the limits of remote detection for measuring minor atmospheric constituents or contaminants. When compared with classical Raman scattering in the visible, the resonance Raman

enhancements have shown increases in the scattered signals by several orders of magnitude [Chamberlain *et al.*, 1976].

Chapter 3: Optical Scattering

Optical scattering is responsible for many atmospheric phenomena. As light waves propagate through the atmosphere, they scatter off of the molecules in the air. The most well-known effect is the blue sky, which is due to atmospheric molecular scattering, often referred to as Rayleigh scattering. Most of the photons incident on molecules are elastically scattered and the cross section is proportional to λ^{-4} . One might then argue that the sky should be purple, but the solar spectrum is peaked at yellow wavelengths, and the human eye is also more responsive to blue than purple; therefore, the scattered light in the eye's photometric response appears blue. There are many other phenomena that result from optical scattering, such as a rainbow, which is produced by the refractive dispersion of light at the air-water interface of the nearly spherical water droplets, as seen in Figure 3.1. Figure 3.2 shows a sundog that is the result of refraction at the surface of small ice crystals in the air. The phenomenon known as the green flash, which results from the fact that shorter wavelengths scatter through larger angles than do the longer wavelengths, is shown in Figure 3.2. As the Sun sets, the red end of the spectrum no longer bends enough to be seen above the horizon, and then the green and blue portions of the spectrum are left to create a flash of green light for a brief moment of time the green intensity is larger than blue. Each of these phenomena is a result of light scattering from particles, without any change in energy or wavelength of the scattered photon. A far less probable form of light scattering, and one more difficult to observe, was discovered

by C.V. Raman, and thus has become known as Raman scattering. Raman scattering occurs when there is a difference in incident and scattered energy that involves the exchange of energy between the incident photon and the energy states of a molecule, and therefore results in a significant difference between the incident and scattered wavelengths.



Figure 3.1. Rainbow (contributed by David Willitsford)

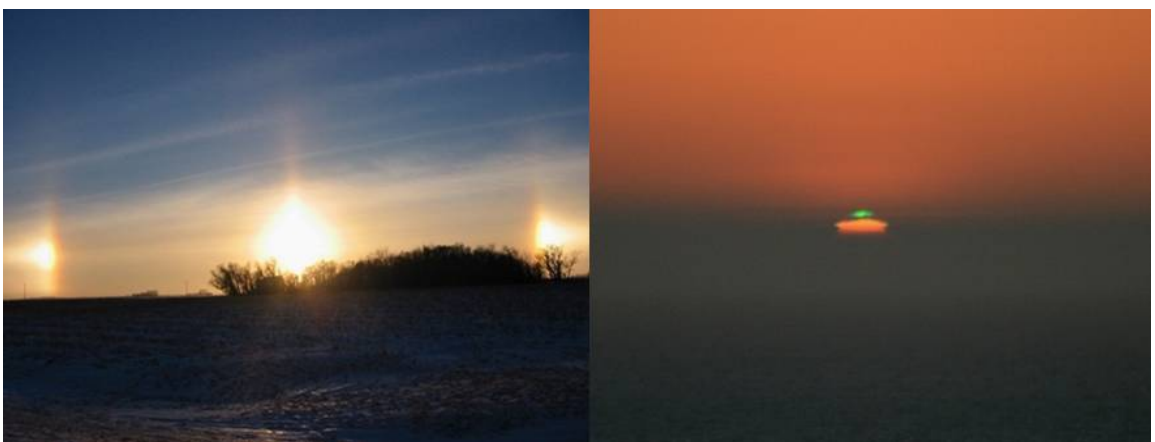


Figure 3.2. Left: Sundog (New Ulm, MN, Erik Axdahl)

Right: Green flash (San Francisco, CA, Mila Zinkova)

3.1 C.V. Raman and Raman Scattering

Raman scattering has been developed into a standard laboratory technique since its discovery in 1928 by C.V. Raman [Raman, 1928]. Because there was such a great interest in the newly discovered phenomenon by the end of 1928, the year of the discovery, 70 publications were in print. The following year saw continued growth in this research topic with more than 200 papers published. By the end of the 1930s more than 1800, papers documenting the spectra of over 2500 samples, had been published [Fabelnskii, 1998].

Appendix A shows the first photograph of the molecular vibration spectra taken by C.V. Raman. This discovery was so profound and useful to the advancement of science, that in 1930 Raman was awarded the Nobel Prize for his efforts in optical scattering [Nobel Prize, 1930]. Raman scattering is a process by which light scatters from a molecule at a different wavelength or energy than that which was incident on the molecule. The change in wavelength of the scattering photon results from energy exchange with the molecules' energy states, including vibration, bending, stretching, or rotational transitions. Early studies using Raman spectroscopy provided much data on the vibrational energy states and spectra of many molecules [Hibben, 1939]. The vibrational spectrum provides the traditional 'fingerprint' that is used in the identification of molecules from their infrared absorption and/or Raman scattering. Because the vibrational states of a molecule are determined by the mass of the atoms as well as their bond strengths and bond angles, the quantized modes are unique for each molecule. By exciting these different vibrational and rotational modes and then analyzing the resultant Raman scattered

spectra, one can use Raman spectroscopy as a powerful tool for uniquely locating, identifying, and quantifying unknown molecular species.

3.1.1 Stokes and Anti-Stokes Raman Scattering

Raman scattering is subdivided into Stokes and anti-Stokes Raman scattering components. A Stokes shift results when the scattered radiation appears at a lower energy, or a longer wavelength (red-shifted), relative to the incident radiation, and anti-Stokes scattering results when the scattered radiation occurs at a higher energy, or shorter wavelength (blue-shifted). Figure 3.3 illustrates a virtual energy diagram showing the difference between Rayleigh scattering, Stokes scattering and anti-Stokes scattering. In the diagram ν_0 , is the ground state, ν_e is the vibrationally excited state, and $\Delta\nu$ is the energy of the scattered photon. Rayleigh scattering results when the initial and final state of the molecule is the same, and no loss or gain of energy occurs. Stokes Raman occurs when the molecule keeps some of the incident energy and scatters a photon with lower energy, red-shifting the scattered light. Anti-Stokes Raman occurs when the molecule starts in an excited state and the donates energy to the scattered photon, blue-shifting the scattered light.

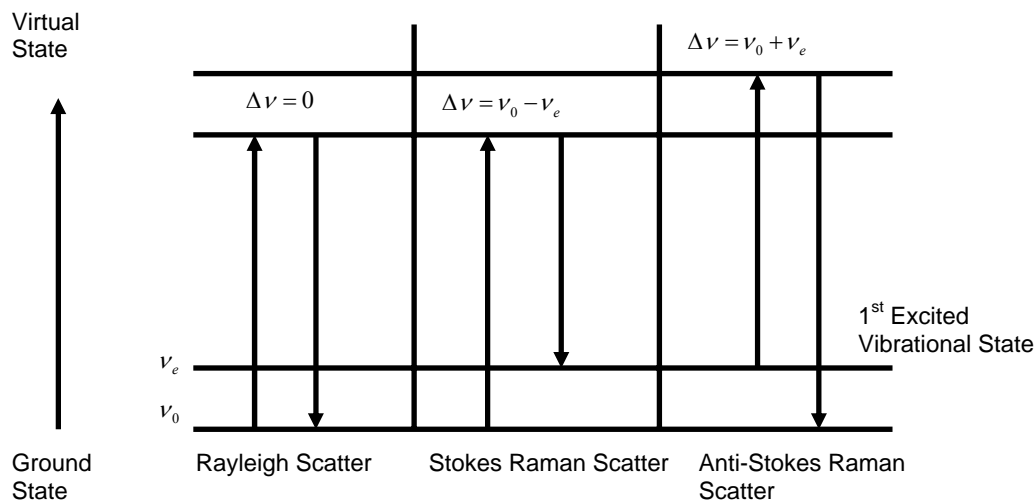


Figure 3.3. Optical scattering, ν_0 is the ground state, ν_e is the vibrationally excited state, and $\Delta\nu$ is the energy of the scattered photon [Inaba, 1976]

The Stokes Raman scattering is more probable because most molecules are in their ground state; however, with increasing temperature more of the molecules will be elevated to an excited state, as predicted by the Boltzmann distribution,

$$f(E) = Ae^{-\frac{E}{kT}},$$

where the probability that a molecule will have energy, E , depends on its temperature T , and a normalization constant, A . With increasing temperature, the Boltzmann distribution results in a higher probability that the molecule will reside in an excited state, and so scattering may result in an anti-Stokes component. Because Raman scattering is dependent on the initial state of the molecule, it is possible to retrieve the temperature by taking the ratio of the Stokes to anti-Stokes Raman signals [Alpers *et al.*, 2004]. The changes in the probability distribution function of the rotational states will also yield in the rotational Raman scattered signals that permit calculations of the temperature.

3.1.2 Vibrational Raman Spectral ‘Fingerprints’

Raman scatter depends on the initial state of the molecule and on the set of quantized energy states associated with the vibration, rotation, stretching, and bending of the molecules bonds, which determine the spectral fingerprint. Each molecule has a unique structure, mass, bond length, and bond strength, and therefore maintains its own set of unique Raman shifts associated with the quantized energy levels of each dynamical mode of a molecule. Using the molecule’s physical characteristics, the energy shift associated with the vibrational or rotational transitions within the simple molecules can be calculated. The energy shifts associated with the quantized transitions can be imparted to the molecule and thereby subtract from the incident energy in the case of Stokes scattering (red-shift). Alternatively, the energy of a vibration (or rotation) may be released or added to the incident energy when the molecule resides in an energy state above the ground state, and this process is referred to as anti-Stokes scattering (blue-shift). Figure 3.4 displays the vibrational shift for an array of molecules. It should be noted that the largest shift, 4160 cm^{-1} (wavenumbers) is associated with H_2 because the hydrogen bond is the strongest, thus exchanging the most excitation energy. Because hydrogen has the strongest bond that can participate in Raman scattering, the bandwidth is typically taken to be $\sim 4200\text{ cm}^{-1}$ and corresponds to the $2.4\text{ }\mu\text{m}$ end of the optical spectrum. Thus, any Raman scattered light (excluding multiple phonons, combination modes, or overtones) will occur within 4200 cm^{-1} of the excitation wavenumber. Appendix B shows typical Raman scattering energies for different vibrational groups.

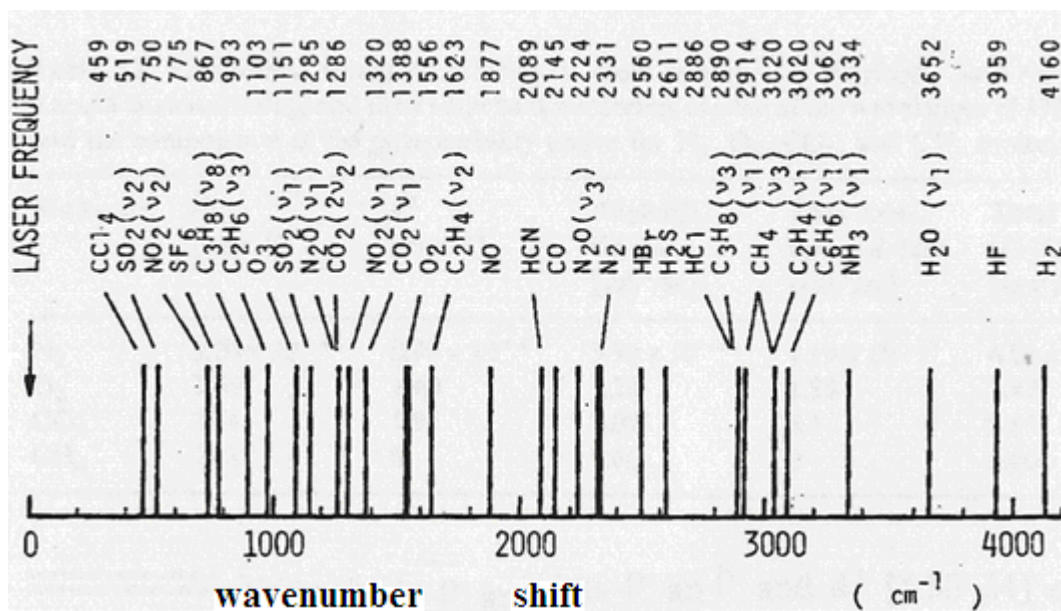


Figure 3.4. Vibrational Raman shift of a collection of molecules [Inaba 1976]

The energy shifts noted above are part of the vibrational spectral fingerprint of the molecules. The spectrum of the scattered radiation provides an easy method to distinguish the different molecules, because the scattered wavelength is Raman-shifted by a vibrational energy level specific to each molecule's properties. For example, if a laser beam from the 2nd harmonic of the Nd:YAG laser is Raman scattered by hydrogen,

Incident Wavelength = 532 nm (2nd Harmonic Nd : YAG Laser)

H₂ RamanShift = 4160 cm⁻¹

18797 cm⁻¹ - 4160 cm⁻¹ = 14637 cm⁻¹

$\frac{14637}{\text{cm}} * \frac{100 \text{ cm}}{1 \text{ m}} = 2403280 \text{ m}^{-1}$, corresponding to 683.2 nm.

The first vibrational shift for H₂ occurs at 4160 cm⁻¹. When hydrogen is excited by a laser at a wavelength of 532 nm, this excitation wavelength will result in a vibrationally scattered wavelength of ~ 683.2 nm. With the detection of scattered radiation at 683.2 nm, the presence of hydrogen is confirmed. The magnitude of the

signal may also be used to make calculations of the quantity of hydrogen present.

With shorter excitation wavelengths, the Raman scattered spectra spanning ~ 4000 cm^{-1} becomes compressed to the wavelengths shown in Table 3.1 for excitation at 250 nm and 500 nm.

Table 3.1. Raman Spectral Range

Excitation Wavelength	4000 cm^{-1}	$\Delta\lambda$
250 nm	277.8 nm	27.8 nm
500 nm	625 nm	125 nm

3.1.3 Rotational Raman Scattering

Energy shifts associated with rotational modes of a molecule are significantly smaller in energy than are the vibrational modes. Typical rotational Raman shifts are in the range from 5 cm^{-1} to 200 cm^{-1} , and the rotational spectral lines thus appear close to the Rayleigh (elastically) scattered line [Penney, 1974]. Figure 3.5 shows a Morse potential diagram depicting the energy levels of a typical atom or molecule. The ν levels represent the vibrational states of the molecule, and the R -levels represent the rotational states of the molecule, with ν_0 being the rest state.

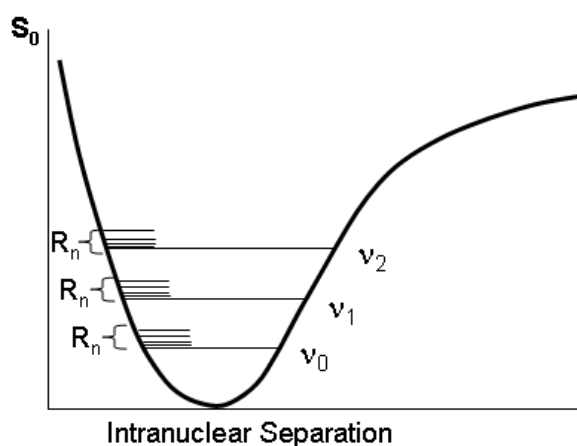


Figure 3.5. Vibrational and rotational energy diagram, ν levels correspond to vibrational states and R_n levels correspond to rotational states

It is relatively straight-forward to model and calculate the rotational Raman scatter of simple two-atom rotors, which typically represent the atmospheric molecules, nitrogen (N_2) and oxygen (O_2) [Behrendt and Nakamura, 2002]. The rotational lines occur on both the Stokes and anti-Stokes sides of the incident radiation; the Stokes features will have larger cross-sections, because of the larger probability that the molecules reside in lower energy states. Figure 3.6 shows the calculated rotational Raman spectra for a simple two-atom rotor such as nitrogen and oxygen at 200 K. For comparison, Figure 3.7 shows the rotational Raman spectra for nitrogen and oxygen at 300 K; notice that rotational states further from the center (Rayleigh line) are populated as the higher temperature broadens the distribution, also notice that the populations of the lowest energy states —those closer to the Rayleigh line— decrease as the higher states are populated. There is also a change in the magnitude of each state, as more of the energy is coupled into the higher energy states.

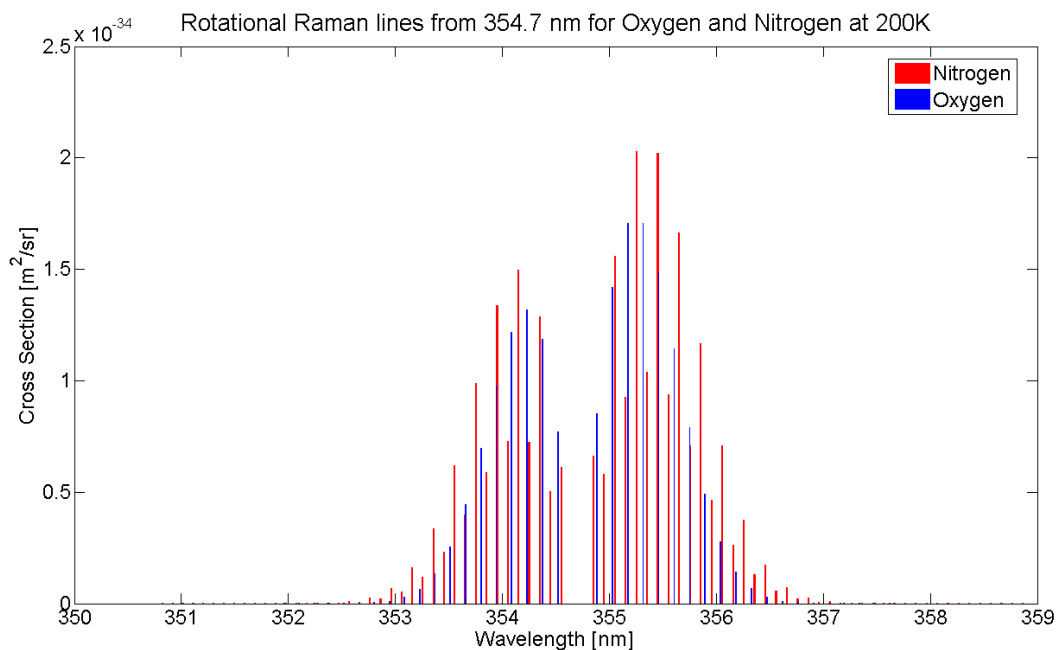


Figure 3.6. Rotational Raman lines for oxygen and nitrogen at 200K

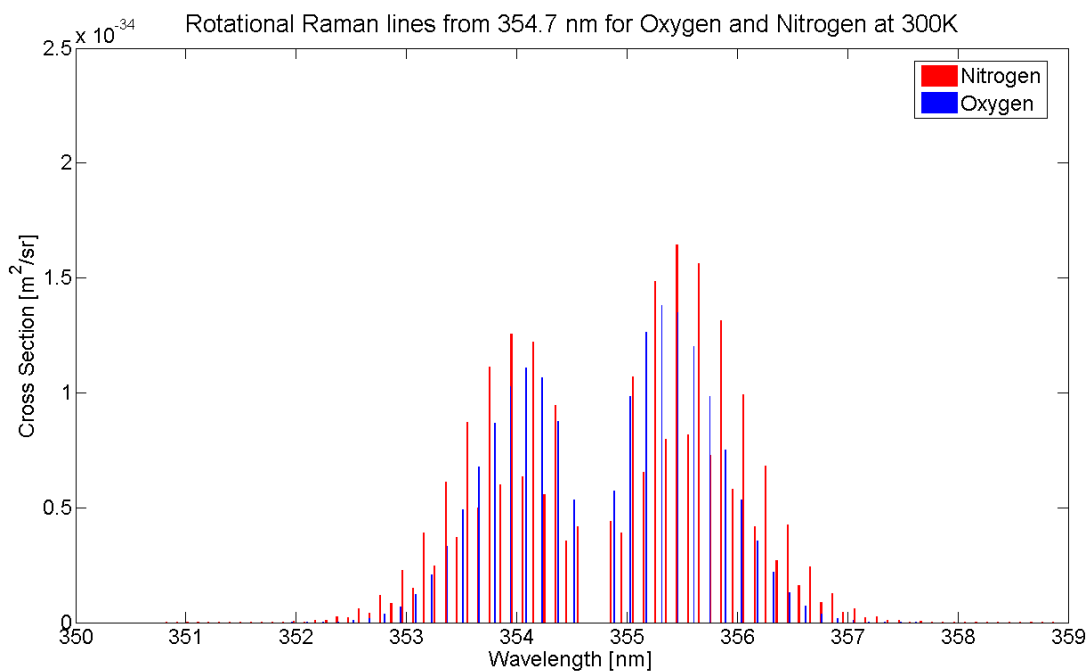


Figure 3.7. Rotational Raman lines for oxygen and nitrogen at 300K

3.2 Coherent Anti-Stokes Raman Spectroscopy

Coherent anti-Stokes Raman scattering, or CARS, is a nonlinear optical process typically described as four-wave mixing [Tolles *et al.*, 1977]. Coherent Raman spectroscopy yields similar information to normal Raman scattering; due to the efficient transfer of energy to the scattering medium however, signal levels may be improved by as much as nine orders of magnitude [Melveger, 1978]. CARS is a useful tool for probing chemicals in a laboratory situation, but there are several obstacles when applying this technique to remote sensing. The coherent anti-Stokes Raman scatter is exclusively a forward-scatter process, meaning that a traditional Raman lidar that relies on back-scattered signals would not be possible. Also, in order for the coherent Raman scattering process to occur, the pump and probe beams must be perfectly overlapped, both spatially and temporally.

3.2.1 Pump, Probe, and Four-wave Mixing

The coherent process known as four-wave mixing involves the interaction of three electromagnetic fields to create a fourth field, in this case it is the anti-Stokes Raman scatter. The process of electromagnetic interaction with a material can be expanded using a Taylor series of the induced polarization \vec{P} , in terms of the applied local electric field,

$$\vec{P} = \varepsilon_0 \chi^{(1)} \vec{E} + \varepsilon_0 \chi^{(2)} \vec{E}^2 + \varepsilon_0 \chi^{(3)} \vec{E}^3 + \dots,$$

where $\chi^{(1)}$ is known as the linear electro-optic effect or Pockels effect. The Pockels effect is used in Pockels cells to provide a linear voltage-controlled optical polarization rotator. The $\chi^{(2)}$ effect is known as the quadratic electro-optic effect or Kerr Effect. Although the Kerr effect is typically weaker than the Pockels effect, it was discovered first in 1875, because it is present in all materials. In contrast, the Pockels effect was only discovered in 1893, because it is only found in noncentrosymmetric materials. The study of CARS involves utilizing the $\chi^{(3)}$ effect, in which three electromagnetic fields interact to form sum and difference frequencies coherently to generate an anti-Stokes photon. Although there are only two different beams, the process is still considered to be four-wave mixing as the incident radiation is degenerate and is used twice during the coherent Raman process. Figure 3.8 shows the CARS process that generates the anti-Stokes signal. In the CARS process,

$$\nu_c = 2\nu_p - \nu_s,$$

where

ν_p is the incident (pump) radiation energy,
 ν_s is the Stokes (probe) radiation energy,
 ν_c is the scattered radiation or CARS energy.

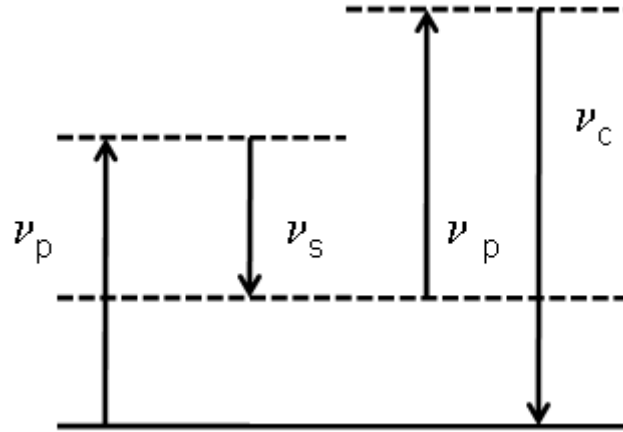


Figure 3.8. Coherent anti-Stokes Raman spectroscopy. Two pump photons ν_p are mixed with the Stokes photon ν_s to retrieve the scattered photon ν_s

When the difference between ν_p and ν_s is equal to a vibronic energy level, a resonant enhancement is seen in the CARS signal.

$$\nu_r = \nu_p - \nu_s \quad (\text{resonant enhancement})$$

The resonant enhancement will occur when this relation is satisfied, thus increasing the CARS signal by several orders of magnitude.

3.2.2 White Light Laser (Stokes Probe)

As is mentioned above, in order to see the large signal increase associated with scanning CARS, it is necessary to scan the Stokes (probe) laser beam. However, by utilizing a supercontinuum “white light” laser there is no need to scan the probe because the laser energy is already present in each pulse. A white light laser is an extremely broadband laser source that is spatially coherent but temporally incoherent.

Spatial coherence means that it is possible to focus and collimate the laser beam, while temporal incoherence means that it has a broadband emission. It is commonly called a white light laser because the laser is white due to the presence of laser light throughout the visible spectrum.[†] By utilizing an ultra-fast laser pulse (~femtosecond) propagated through a highly nonlinear fiber, it is possible to generate a laser beam with a supercontinuum spectrum. Figure 3.9 shows a prism expansion of a supercontinuum white light laser developed in the Ultra-fast Optics Lab at The Pennsylvania State University.

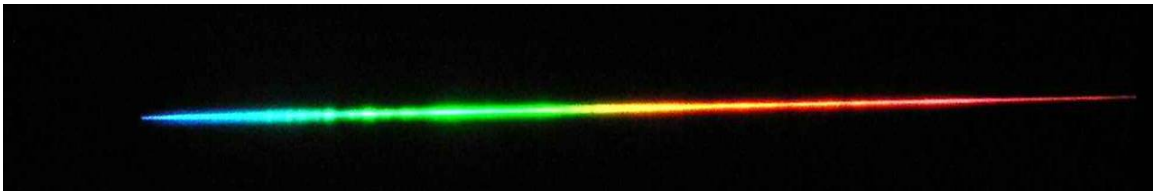


Figure 3.9. Dispersion of the supercontinuum white light laser in the Ultra-fast Optics Lab at Penn State University

3.3 Fluorescence

Fluorescence is a serious obstacle in Raman scattering studies because even low levels of photoemission can mask the much weaker Raman effect. The fluorescence cross section can exceed the Raman scattering cross sections by as many as 12 orders of magnitude [Inaba, 1978]. Fluorescence is the spontaneous emission of a photon following excitation of electronic states by the absorption of incident radiation. Non-radiative transitions following the absorption result in spontaneous re-emission in a band of wavelengths and often create a broadband emission (fluorescence), which can mask the Raman return. The schematic Figure 3.10

[†] Supercontinuum is more commonly accepted because it applies to any broadband laser source, either in the ultraviolet, visible, or infrared without the need for an actual beam to appear white.

represents the mechanism by which broadband emission occurs, when creating the fluorescent effect. The fluorescent process in many molecules experiences a *quenching* effect in the lower atmosphere, where the scattering intensity is lowered by several orders of magnitude due to collisions that dissipate energy without the emission of a photon. In a low-pressure situation either in a laboratory chamber or in the upper atmosphere (where collisions are less frequent), this quenching effect is greatly reduced. Although the quenching effects reduce the intensity of fluorescence, the signal may still be too strong to distinguish any underlying Raman scattered light.

Other means of reducing fluorescence and other unwanted signals, must be employed to measure the weaker Raman scattered signals. A common method of reducing background signals is accomplished by the use of narrowband filters centered on the wavelength of the expected Raman scattered signals. Another method for reducing the interference of fluorescence is through the use of time gating of the scattered signals for pulsed laser excitation [Matousek, 2000]. Raman scattering is nearly instantaneous; however, the broadband process of fluorescence is much slower and can be partially separated by preventing the detector from counting photons beyond the interval corresponding to immediate scattering of the fundamental laser pulse.

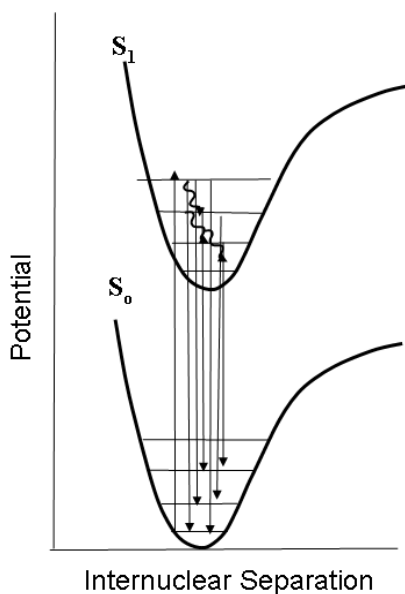


Figure 3.10. Broadband emission due to fluorescence, S_0 is the ground state and S_1 is the excited state

3.4 Resonance Raman Scattering

Resonance Raman scattering occurs when the wavelength of excitation falls near or within an electronic or vibrational absorption band of the molecule, and thereby enhances the coupling of energy into the vibrational modes of the absorbing species. This scattering enhancement can be as much as 3-to-8 orders of magnitude larger than that of classical Raman scattering [Chamberlain *et al.*, 1976]. Although the resonance effect greatly enhances the scattering power, this effect is not always observed easily because the simultaneous higher absorption, combined with the interfering effects of fluorescence, may hide the enhanced Raman scattered radiation. Figure 3.11 shows a comparison of Raman scattering, pre-resonance Raman, resonance Raman, and fluorescence interactions. The upward portion of the arrows represents the incident energy with the curved peak being the point where the scattering results and the downward portion of the arrow represents the Raman

scattered wavelength. The approximate scattering cross sections for each of the different scattering mechanisms are listed in Table 3.2.

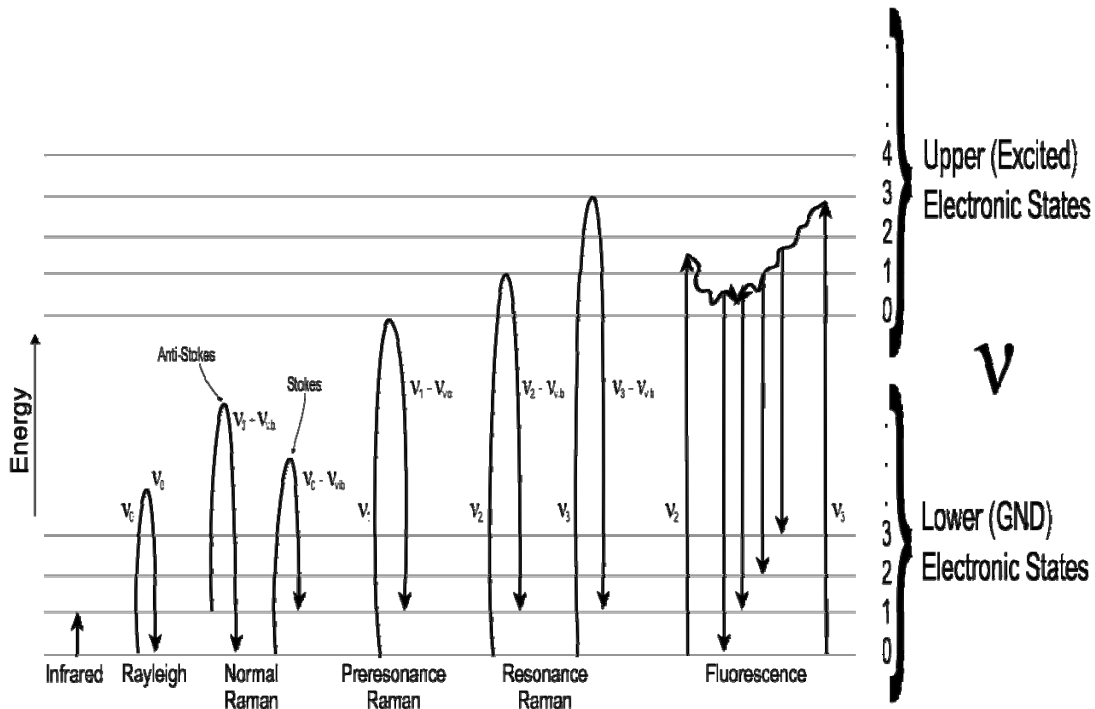


Figure 3.11. Optical scattering mechanisms [Inaba, 1975]

The fluorescent signal may be quite large and is also very broad, resulting in little opportunity to identify it due to its broadband emission. Fluorescence occurs in many different chemical and biological molecules, however, its specificity is lost due to the non-radiative transitions occurring in the scattering medium. As a result, it is often possible to use fluorescence as a means for detection of a broad class of materials, but not as a means to identify a specific material. The fluorescent emission is very slow relative to Raman scattering, and allows the vibrational energy of the electronic states to degenerate back to its lower vibrational levels. Therefore, the wavelengths of the fluorescence photons are mostly independent of the incident

radiation; thus the Raman signals do reflect the energy states unique to the scattering molecules [Levenson, 1989]. Most molecules do not generally fluoresce with any significant intensity when the excitation energies are below about 280 nm, and this factor can be very important for investigations of the resonance Raman properties.

Table 3.2. Optical scattering cross sections [Inaba, 1975]

Interaction	Process	Frequency Relation	Cross-Section ($\frac{cm^2}{sr}$)	Detectable Constituents
Scattering	Mie	$\nu_r = \nu_0$	$10^{-26} - 10^{-8}$	Particulate Matter
	Rayleigh	$\nu_r = \nu_0$	10^{-26} (NR) 10^{-23} (R)	Atoms & Molecules
	Raman	$\nu_r \neq \nu_0$	10^{-29} (NR) 10^{-26} (R)	Molecules (atoms)
Emission	Fluorescence	$\nu_r = \nu_0$	10^{-26} (Quenched)	Atoms & Molecules
		$\nu_r \neq \nu_0$	10^{-24} (Quenched)	
Absorption		$\nu_r = \nu_0$	10^{-20}	Atoms & Molecules

ν_r : Detection Frequency, ν_0 : Laser Frequency; NR: Non-Resonance, R: Resonance, (Inaba)

3.5 Lidar

Lidar (Light Detection And Ranging), commonly referred to as laser radar, has been developed as a method of remotely detecting several of the chemical species in the atmosphere. The Penn State Lidar Lab has developed a number of Raman lidar instruments, and used them for the investigations of the properties and processes in the atmosphere. The focus of recent studies has been on the investigations of atmospheric properties, and molecular species [Brown *et al.*, 2008, Philbrick *et al.*, 2006, Willitsford *et al.* 2005].

3.5.1 Lidar Fundamentals

A lidar system transmits a pulsed laser beam into the atmosphere where it is scattered from molecules and aerosols. The molecules in the atmosphere —primarily nitrogen (N_2), oxygen (O_2) and water vapor (H_2O)— scatter the energy from a laser beam, this scattered energy is collected and analyzed. A monostatic lidar transmits and receives on the same axis, while bistatic or multistatic receivers are located off of the transmit axis to provide information on the angle dependence of the scattered radiation. In either setup, the scattered signals are generally measured with a photomultiplier tube (PMT) in analog or digital counting mode, or with a solid state detector. The collected signals are then analyzed to obtain results on the concentration of atmospheric constituents, or to determine one of several meteorological properties. The backscattered return signals contain information from both Rayleigh and Raman scattering processes. The rotational Raman scattered signals carry the specific information on atmospheric temperature, and the vibrational scattered signals contain information on the concentration of molecular species, such as water vapor and ozone.

3.5.2 LAPS

The LAPS (Lidar Atmospheric Profile Sensor) instrument, shown in Figure 3.12, was developed at Penn State by faculty, staff, and graduate students as an operational prototype for the United States Navy. The LAPS unit was initially constructed to measure atmospheric temperature and water vapor profiles to support meteorological forecasting, to correct radar returns affected by RF refraction, and to

demonstrate a replacement for cumbersome radiosonde[‡] measurements. The LAPS unit was successfully tested in September and October of 1996 in the Gulf of Mexico and the Atlantic Ocean [Philbrick, 1996]. Following these tests, the LAPS unit has been used as a research tool for investigating and characterizing the evolution of air pollution episodes. The LAPS lidar has proven its utility with extensive studies of atmospheric water vapor, temperature, ozone, and particulates [Philbrick *et al.* 1997, Esposito and Philbrick, 1998; Philbrick and Mulik, 2000.]. The data collected by the LAPS Raman lidar have been supplemented with balloon sonde measurements as well as aircraft measurements to develop a more complete picture of complex atmospheric interactions [Philbrick *et al.*, 2003].

[‡] A radiosonde or balloon sonde is a meteorological sensor package attached to a helium-filled balloon. It is released into the air and during its ascent transmits measurements of atmospheric properties back to a base station on the ground.

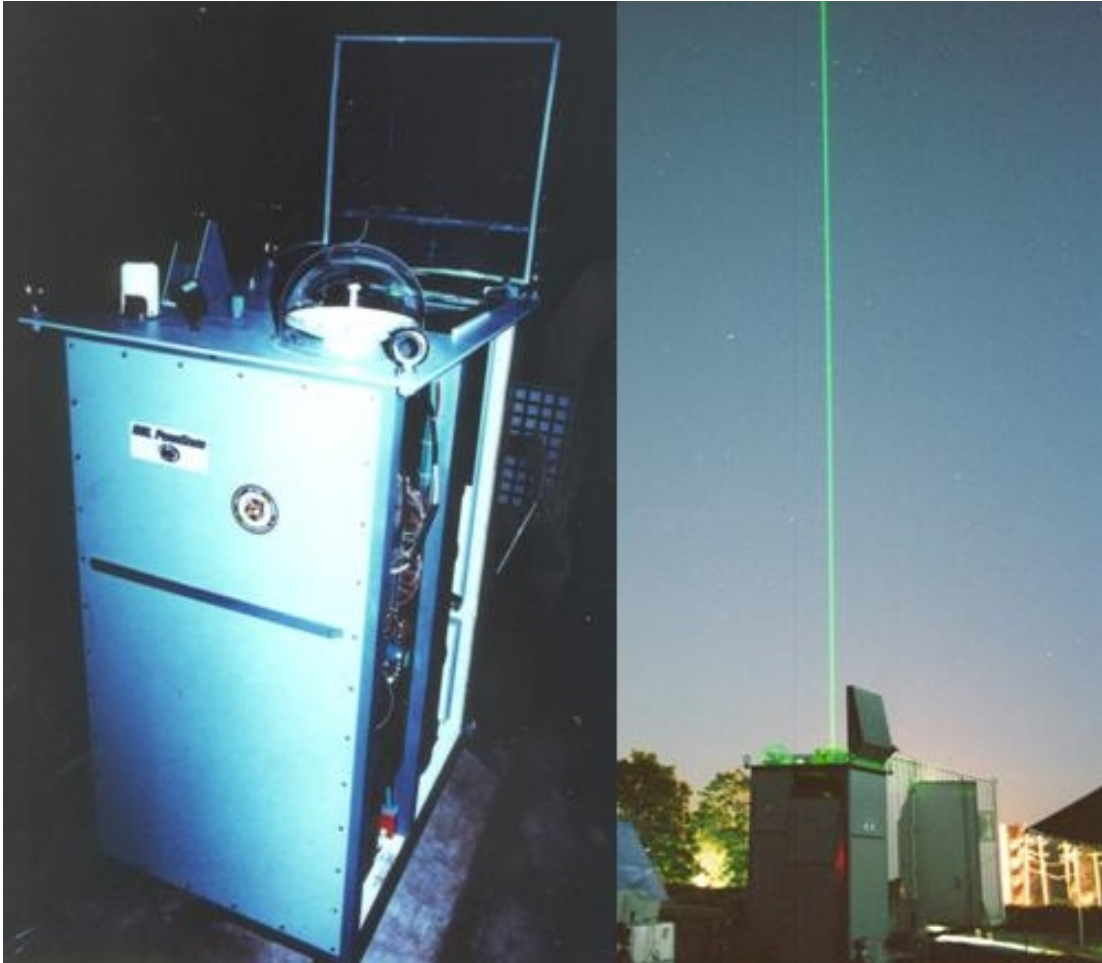


Figure 3.12. Lidar Atmospheric Profile Sensor (LAPS) at Penn State University

3.6 Summary

Rayleigh scattering where the scattered wavelength is essentially the same as the incident wavelength, in the natural atmosphere is a commonly observed phenomenon. A far less probable form of optical scattering is known as Raman scattering. Raman scattering from incident laser beams has proven to be a useful tool for the identification and quantification of many molecules. Following the developments of the laser in the early 1960s that provided a coherent and nearly monochromatic source, Raman scattering using laser beams has proved to be most valuable in locating and identifying unknown chemical species. The extremely small

scattering cross section of non-resonant Raman scattering make it difficult to detect, identify, and quantify small concentrations of chemical species. Lidar measurements of molecular concentrations are possible when using backscattered signals from the unique fingerprints of Raman spectra. By using the resonant enhancement process, a further extension of Raman spectral analysis is possible. Resonance-enhanced Raman scatter is expected to extend lidar remote sensing techniques by improving signal-to-noise ratio and permitting detection of lower concentrations of molecular species over larger distances.

Chapter 4: Theory of Resonance- Enhanced Raman Scattering

An overview of the theoretical background of resonantly enhanced Raman scattering is now provided as a foundation for this subject. The theory was first developed by Shorygin [1947] and expanded by the work of Albrecht [1961]. Over the years, many different methods for presenting and interpreting the theory of resonant enhanced Raman scatter have been proposed [Albrecht, 1961; Behringer, 1974; Spiro, 1977; Hong, 1977a and 1977b]. I have chosen to present a summary based upon the work of Clark and Dines [1986], with additional contributions of Long [2001]. The results and equations from this approach have become widely used and well-known within the community of researchers who work in the field.

4.1 Classical Light Scattering – Dipole Scattering

Raman scattering occurs when a dipole is induced in a molecule by the electric field of the applied electro-magnetic wave, and the result is dipole scattering from the molecule. The time-averaged power per unit solid angle is [Long, 2001],

$$I = k'_v \nu_s^4 p_0^2 \sin^2(\theta), \quad [4.1]$$

where,

$$k'_v = \frac{\pi^2 c_0}{2\epsilon_0},$$

p_0 is the amplitude of the induced dipole of frequency ν_s (scattered), and

θ is the angle with respect to the axis of the dipole.

The induced electric dipole can be viewed as a sum of an infinite series

$$p_o = p^{(1)} + p^{(2)} + p^{(3)} + \dots,$$

which generally converges quite quickly [Long, 2001] because

$$p^{(1)} \gg p^{(2)} \gg p^{(3)}$$

$$\bar{p}^{(1)} = \alpha \vec{E} \quad \text{where } \alpha \text{ is the molecular polarizability tensor of 2nd rank,}$$

$$\bar{p}^{(2)} = \frac{1}{2} \beta \vec{E} \vec{E} \quad \text{where } \beta \text{ is the hyperpolarizability tensor of 3rd rank,}$$

$$\bar{p}^{(3)} = \frac{1}{6} \gamma \vec{E} \vec{E} \vec{E} \quad \text{where } \gamma \text{ is the second hyperpolarizability tensor of 4th rank.}$$

By substituting p_0 into Equation [4.1], one retrieves [Long, 2001],

$$I = k_v 'v_s^4 [\alpha \vec{E}(v_{laser})]^2 \sin^2[\theta]. \quad [4.2]$$

From Equation 4.2, it is clear that the intensity of the scattered light is proportional to the fourth power of the scattered frequency and to the square of the E-field strength.

4.1.1 Rayleigh and Raman Scatter

By utilizing a Taylor series expansion and ignoring higher terms the polarizability tensor α can be described [Long, 2001] as,

$$(\alpha_{\rho\sigma})_k = (\alpha_{\rho\sigma})_0 + \left(\frac{\partial \alpha_{\rho\sigma}}{\partial Q_k} \right)_0 Q_k, \quad [4.3]$$

where,

$$Q_k = Q_{k0} \cos(v_k t + \delta_k).$$

Therefore, the polarizability tensor at frequency ν_k is equal to the polarizability tensor at the equilibrium point plus a perturbation from the equilibrium point that depends on ν_k . The electric field from the incident radiation field is,

$$\vec{E} = \vec{E}_0 \cos(\nu_l t),$$

where ν_l is the frequency of excitation (laser).

Examining $\vec{p}^{(1)} = (\alpha_{\rho\sigma})_k \vec{E}$, we can then calculate the time dependence of the induced electric dipole from the E-field and the polarizability tensor [Long, 2001], i.e.,

$$\vec{p}^{(1)} = (\alpha_{\rho\sigma})_0 \vec{E}_0 \cos(\nu_l t) + \left(\frac{\partial \alpha_{\rho\sigma}}{\partial Q_k} \right)_0 Q_{k0} \cos(\nu_k t + \delta_k) \vec{E}_0 \cos(\nu_l t).$$

By applying the trigonometric identity,

$$\cos(a)\cos(b) = \frac{1}{2} [\cos(a-b) + \cos(a+b)],$$

it is possible to separate the frequency components of the induced dipole moment into an elastically scattered component, as well as the Raman Stokes and anti-Stokes components.

When the molecule of interest is excited by the incident electric field, a dipole moment is created that oscillates at the excitation frequency and thereby re-radiates energy at the same frequency resulting in elastic or Rayleigh scatter. In the same volume, a small fraction of the molecules becomes excited and modulates the incident frequency by ($\pm \nu_k$) creating Raman Stokes and Raman anti-Stokes features which can be described as,

$$\begin{aligned}
 \bar{p}^{(1)} &= \underbrace{(\alpha_{\rho\sigma})_0 \vec{E}_0 \cos(\nu_l t)}_{\text{Rayleigh}} + \underbrace{\left(\frac{\partial \alpha_{\rho\sigma}}{\partial Q_k} \right)_0 Q_{k0} \cos(\nu_k t + \delta_k) \vec{E}_0 \cos(\nu_l t)}_{\cos(a)\cos(b) = \frac{1}{2} [\cos(a-b) + \cos(a+b)]} \\
 &\qquad\qquad\qquad \underbrace{\hspace{10em}}_{\text{Raman}} \\
 &\qquad\qquad\qquad \left(\frac{\partial \alpha_{\rho\sigma}}{\partial Q_k} \right)_0 Q_{k0} \vec{E}_0 \frac{1}{2} [\cos(\nu_l t - \nu_k t) + \cos(\nu_l t + \nu_k t)] \\
 &\qquad\qquad\qquad \swarrow \qquad\qquad \searrow \\
 &\qquad\qquad\qquad \text{Stokes} \qquad\qquad \text{Anti-Stokes}
 \end{aligned}$$

hence,

$$p_{\text{Rayleigh}}^{(1)}(\nu_l) = (\alpha_{\rho\sigma})_0 \vec{E}_0 \cos(\nu_l t)$$

$$\bar{p}_{\text{Raman}}^{(1)}(\nu_k + \nu_l) = \left(\frac{\partial \alpha_{\rho\sigma}}{\partial Q_k} \right)_0 Q_{k0} \vec{E}_0 \frac{1}{2} [\cos(\nu_l t - \nu_k t) + \cos(\nu_l t + \nu_k t)].$$

Because all molecules are polarizable [Long, 2001], a portion of α_0 will be non-zero and, therefore, Rayleigh scattering will always exist. In order for Raman scattering to occur (i.e. Raman active), the polarizability must change so that,

$$\left(\frac{\partial \alpha_{\rho\sigma}}{\partial Q_k} \right)_0 \neq 0.$$

That is, the derivative of the polarizability with respect to the normal mode must be non-zero in the case of Raman scattering. It follows that if there is no change in the polarizability due to an induced dipole moment, then the polarization of the scattering wave, $\bar{p}_{\text{Raman}}^{(1)}(\nu_k + \nu_l)$ will be zero. In this case, there will be no resultant scattering at either the Stokes or anti-Stokes Raman wavelengths.

4.2 Infrared Active and Raman Active Selection Rules

In order for a molecule to be infrared active so that infrared absorption at a certain frequency is allowed, the molecule must first have a permanent electric dipole moment. This dipole moment can then be modulated at the incident frequency, thus it is infrared active and absorbs energy from photons with energies near the energy of resonance corresponding to its quantized energy state. In order for a molecule to be Raman active so that a certain mode can be excited, a dipole moment must be induced by the electric field of the incident radiation. This induced dipole moment is a result of the motions of the electrons relative to the nucleus caused by the electric field of the scattering photon. Finally, the rule of mutual exclusion states that, if a molecule has a center of symmetry, then there are no modes that are both infrared and Raman active [Long, 2001].

4.3 Dirac Notation - Bra-Ket Operators

In order for the quantum mechanical equations to describe the absorption and scattering processes, we choose to use the notation for quantum states that was first introduced by Paul Dirac [Dirac, 1939] called bra-ket, from the “bra” and “ket” in “bracket”. The ‘left’ quantum state is defined as the bra $\langle a|$, and the ‘right’ quantum state is the ket $|b\rangle$. When combined $\langle a|b\rangle$, the bra-ket operator represents the inner product of a and b . In the case of quantum states, the complex conjugate is implied in the bra operator, but not in the ket. That is we have,

$$\Psi^* = \langle \Psi |.$$

The combination of the bra-ket operator is most commonly used as a multiple integral,

$$\int \Psi^* \Psi dQ_1 = \langle \Psi | \Psi \rangle,$$

and, more specifically,

$$\langle a | A | b \rangle = \int \Psi_a^*(x) A \Psi_b(x) dx.$$

4.4 Quantum Mechanical Treatment of Dipole Scattering

The quantum mechanical approach utilizes perturbation theory to calculate the transition electric dipole. The transition electric dipole is then used to replace the induced electric dipole, and describes the transition polarizability for transitions from an initial state $|i\rangle$ to final a state $\langle f|$ for a given excitation frequency, generally excited by laser frequency. The transition dipole can be described as a sum of individual components where each corresponds to different dependencies on the applied electric field,

$$p_{fi} = (p^1)_{fi} + (p^2)_{fi} + (p^3)_{fi} + \dots,$$

where the subscript fi represents the transition from the initial to the final state. By applying perturbation theory, we can use the bra-ket notation to represent the total transition dipole as,

$$p_{fi} = \langle \Psi_f' | \hat{p} | \Psi_i' \rangle,$$

where,

Ψ_f' is the perturbed time-dependent wave function for the final state,

Ψ_i' is the perturbed time-dependent wave function for the initial state, and

\hat{p} is the electric dipole moment operator.

Through the use of perturbation theory, it is possible to derive expressions for the transition dipole by expressing each term as a linear combination of unperturbed and perturbed states [Long, 2001]. In the case of the electric dipole operator, we can write,

$$(p^1)_{fi} = \langle \Psi_f^0 | \hat{p} | \Psi_i^1 \rangle + \langle \Psi_f^1 | \hat{p} | \Psi_i^0 \rangle.$$

The value is linearly dependent on the applied electric field because each portion is dependent only on a single perturbed state, either Ψ_i^1 or Ψ_f^1 .

4.5 Theory of Resonant-Enhanced Raman Scattering

The experiments performed in my research were carried out using an arrangement with a 90° scattering angle between the incident beam and the collection paths. For a Raman scattering transition between the initial state $|i\rangle$ and final state $\langle f|$, the intensity of the scattered light at 90° with respect to the excitation beam is given by,

$$I_{fi} \left(\frac{\pi}{2} \right) = \frac{\pi^2}{\epsilon_0^2} (\tilde{\nu}_0 \pm \tilde{\nu}_{fi})^4 I_0 \sum_{\rho, \sigma} \left[[\alpha_{\rho\sigma}]_{fi} [\alpha_{\rho\sigma}]_{fi}^* \right]$$

where ,

$\tilde{\nu}_0$ is the wavenumber of the excitation laser,

$\tilde{\nu}_{fi}$ is the wavenumber of the Raman transition $\langle f | \leftarrow | i \rangle$,

$\tilde{\nu}_0 + \tilde{\nu}_{fi}$ is the wavenumber of the Raman anti-Stokes scattered radiation,

$\tilde{\nu}_0 - \tilde{\nu}_{fi}$ is the wavenumber of the Raman Stokes scattered radiation,

I_0 is the irradiance W/m^2 of the incident radiation,

ε_0 is the permittivity of free space, $8.854 \times 10^{-12} \text{ F/m}$,

and $[\alpha_{\rho\sigma}]_{fi}$ is the $\rho\sigma^{\text{th}}$ element of the transition polarizability tensor as given by the Kramers—Heisenberg Dispersion Formula [Kramers & Heisenberg, 1925], and is written as,

$$[\alpha_{\rho\sigma}]_{fi} = \frac{1}{hc} \sum_{r \neq i, f} \left[\frac{[\mu_{\rho}]_{fr} [\mu_{\sigma}]_{ri}}{\tilde{\nu}_{ri} - \tilde{\nu}_o - i\Gamma_r} + \frac{[\mu_{\sigma}]_{fr} [\mu_{\rho}]_{ri}}{\tilde{\nu}_{rf} + \tilde{\nu}_o + i\Gamma_r} \right] \quad [4.4]$$

where,

$[\mu_{\rho}]_{fr}$ is the ρ^{th} component of the transition dipole moment associated with the transition $\langle f | \leftarrow | r \rangle$,

$[\mu_{\sigma}]_{fr}$ is the σ^{th} component of the transition dipole moment associated with the transition $\langle f | \leftarrow | r \rangle$, and

$i\Gamma_r$ is the damping factor that is inversely proportional to the lifetime of state $|r\rangle$.

In the case of resonance-enhanced Raman scatter, the excitation laser frequency, $\tilde{\nu}_0$, is tuned to a frequency near the electronic absorption frequency, $\tilde{\nu}_{ri}$, and as $\tilde{\nu}_0$ approaches $\tilde{\nu}_{ri}$, $\tilde{\nu}_{ri} - \tilde{\nu}_o$ approaches 0. Tuning reduces the denominator of the first term of the polarizability tensor, and results in large increase in the efficiency of the transition. This increase in the polarizability tensor represents the process by which the normally weak Raman scattered signal is enhanced in the resonance process.

Examination of the polarizability tensor, $[\alpha_{\rho\sigma}]_{fi}$, helps our understanding of this enhancement. Under resonance conditions, the 2nd term in the transition polarizability (Equation 4.4) can be neglected, yielding,

$$[\alpha_{\rho\sigma}]_{fi} \cong \frac{1}{hc} \sum_{r \neq i, f} \frac{[\mu_{\rho}]_{fr} [\mu_{\sigma}]_{ri}}{\tilde{\nu}_{ri} - \tilde{\nu}_o - i\Gamma_r}. \quad [4.5]$$

A convenient and commonly used simplification is the Born–Oppenheimer approximation, which is a method for separating the response of the nuclei from that of the electrons. Because the nuclei have significantly more inertia than the electrons, the relative response of the nuclei to the applied field can be neglected, and therefore only the response of the electron distribution needs to be considered. This approximation allows the excited states to be separated into products of vibrational and electronic states, that is,

$$\begin{aligned} |i\rangle &= |e_i \nu_i\rangle = |e_i\rangle | \nu_i \rangle, \\ |r\rangle &= |e_r \nu_r\rangle = |e_r\rangle | \nu_r \rangle, \\ |f\rangle &= |e_f \nu_f\rangle = |e_f\rangle | \nu_f \rangle, \end{aligned}$$

where e and ν represent the electronic and vibrational states for the initial (i), virtual (r), and final (f) states. Typically the initial and final electronic states are the ground state that further simplifies to,

$$\begin{aligned} |i\rangle &= |g \nu_i\rangle = |g\rangle | \nu_i \rangle \\ |r\rangle &= |e_r \nu_r\rangle = |e_r\rangle | \nu_r \rangle \\ |f\rangle &= |g \nu_f\rangle = |g\rangle | \nu_f \rangle. \end{aligned}$$

For this case, Equation [4.5] can be rewritten as,

$$[\alpha_{\rho\sigma}]_{fi} \cong \frac{1}{hc} \sum_{r \neq i, f} \frac{\langle \nu_f | [\mu_{\rho}]_{ge} | \nu_r \rangle \langle \nu_r | [\mu_{\sigma}]_{eg} | \nu_i \rangle}{\tilde{\nu}_{ri} - \tilde{\nu}_o - i\Gamma_r}, \quad [4.6]$$

where $[\mu_\rho]_{ge}$ is the ρ^{th} component of the transition dipole moment for the electronic transition $|g\rangle \leftarrow |e\rangle$ [Dines, 2008].

Finally by applying the Herzberg-Teller [Herzberg and Teller, 1933] expansion to the transition polarizability tensor, one can separate the Raman scattering into what is known as the *A*, *B*, *C*, and *D* terms of the transition polarizability [Long, 2001].

$$[\alpha_{\rho\sigma}]_{fi} = [\alpha_{\rho\sigma}]_{fi}^A + [\alpha_{\rho\sigma}]_{fi}^B + [\alpha_{\rho\sigma}]_{fi}^C + [\alpha_{\rho\sigma}]_{fi}^D$$

The four terms are included for completeness, although the *C* and *D* terms are likely to be very small in magnitude [Long, 2001] and are usually ignored in both Raman scattering and resonance enhanced Raman scattering.

A – Term: In applying the Franck-Condon approximation the polarizability is determined by the electronic transition dipole moment, $[\mu_\rho]$, and the vibrational overlap integral [Long, 2001], and is given by,

$$[\alpha_{\rho\sigma}]_{fi}^A = \frac{1}{hc} [\mu_\rho]_{ge}^0 [\mu_\sigma]_{eg}^0 \sum_{r \neq i, f} \frac{\langle \nu_f^{(g)} | \nu_r^{(e)} \rangle \langle \nu_r^{(e)} | \nu_i^{(g)} \rangle}{\tilde{\nu}_{ri} - \tilde{\nu}_o - i\Gamma_r}. \quad [4.7]$$

B – Term: This term represents the vibronic coupling of the resonant excited state, $|\nu_e^r\rangle$, to one other excited state, $|\nu_e^s\rangle$ [Long, 2001],

$$[\alpha_{\rho\sigma}]_{fi}^B = \frac{1}{h^2 c^2} [\mu_\rho]_{ge}^0 [\mu_\sigma]_{eg}^0 \frac{h_{se}^k}{\Delta \tilde{\nu}_{es}} \sum_{r \neq i, f} \frac{\langle \nu_f^{(g)} | Q_k | \nu_r^{(e)} \rangle \langle \nu_r^{(e)} | \nu_i^{(g)} \rangle}{\tilde{\nu}_{ri} - \tilde{\nu}_o - i\Gamma_r} + \frac{1}{h^2 c^2} [\mu_\rho]_{ge}^0 [\mu_\sigma]_{eg}^0 \frac{h_{es}^k}{\Delta \tilde{\nu}_{se}} \sum_{r \neq i, f} \frac{\langle \nu_f^g | \nu_r^{(e)} \rangle \langle \nu_r^{(e)} | Q_k | \nu_i^{(g)} \rangle}{\tilde{\nu}_{ri} - \tilde{\nu}_o - i\Gamma_r}. \quad [4.8]$$

C – Term: This term represents the vibronic coupling of the ground electronic state

, $|v_e^g\rangle$, to an excited electronic state , $|v_e^t\rangle$ [Long, 2001],

$$\begin{aligned} [\alpha_{\rho\sigma}]_{fi}^C &= \frac{1}{\hbar^2 c^2} [\mu_\rho]_{se}^0 [\mu_\sigma]_{eg}^0 \frac{\hbar_{sg}^k}{\Delta \tilde{\nu}_{gs}} \sum_{r \neq i, f} \frac{\langle v_f^{(g)} | Q_k | v_r^{(e)} \rangle \langle v_r^{(e)} | v_i^{(g)} \rangle}{\tilde{\nu}_{ri} - \tilde{\nu}_o - i\Gamma_r} \\ &+ \frac{1}{\hbar^2 c^2} [\mu_\rho]_{ge}^0 [\mu_\sigma]_{eg}^0 \frac{\hbar_{gs}^k}{\Delta \tilde{\nu}_{sg}} \sum_{r \neq i, f} \frac{\langle v_f^{(g)} | Q_k | v_r^{(e)} \rangle \langle v_r^{(e)} | v_i^{(g)} \rangle}{\tilde{\nu}_{ri} - \tilde{\nu}_o - i\Gamma_r}. \end{aligned} \quad [4.9]$$

D – Term: Vibronic coupling of the excited electronic state, $|v_e^r\rangle$, to two other

excited electronic states , $|v_e^s\rangle$ and $|v_e^{s'}\rangle$ [Long, 2001] is represented,

$$[\alpha_{\rho\sigma}]_{fi}^D = \frac{1}{\hbar^3 c^3} [\mu_\rho]_{gs}^0 [\mu_\sigma]_{eg}^0 \frac{\hbar_{se}^k}{\Delta \tilde{\nu}_{es}} \frac{\hbar_{es}^k}{\Delta \tilde{\nu}_{se}} \sum_{r \neq i, f} \frac{\langle v_f^{(g)} | Q_k | v_r^{(e)} \rangle \langle v_r^{(e)} | Q_k | v_i^{(e)} \rangle}{\tilde{\nu}_{ri} - \tilde{\nu}_o - i\Gamma_r}. \quad [4.10]$$

4.6 Qualitative Description of the A and B Terms for Resonance-Raman

Scattering

The A-term, or the Franck–Condon resonance-Raman effect, is determined by convolving the pure electronic transition dipole moment with the vibrational overlap integrals. The A-term resonance-Raman scattering occurs when two conditions are met [Long, 2001]:

1. The transition dipole moments $[\mu_\rho]_{ge}^0$ and $[\mu_\sigma]_{eg}^0$ must be non-zero [Clark and Dines, 1986], and
2. The products of the vibrational overlap integrals (Franck-Condon factors),

$\langle v_f^{(g)} | v_r^{(e)} \rangle \langle v_r^{(e)} | v_i^{(g)} \rangle$, must be nonzero for at least some value of the

vibrational quantum state, ν [Clark and Dines, 1986].

The first condition is met if the resonant electronic transition is electric-dipole-allowed. This is generally the case when a strong absorption band results from a π - π^* transition, or from charge transfer [Clark and Dines, 1986]. The second condition is met if there is a difference in the vibrational energy between the ground state levels, $|v_i^{(g)}\rangle$, and the electronic excited states, $|v_i^{(e)}\rangle$, resulting in a change of the shape of the potential field, or if there is a displacement ΔQ_k in the minimum of the excited potential field of the electronic states with respect to the normal coordinate Q_k . [Clark and Dines, 1986]. Figure 4.1 displays a diagram of the conditions that represent four possible cases associated with the occurrence of A-term resonance-Raman scattering.

In Figure 4.1(a), there is neither a change in the potential shape, nor a change in the potential minimum, therefore there is no A-term scattering. Figure 4.1(b) shows a change in the potential shape resulting in non-zero vibrational overlap integrals for both totally symmetric and asymmetric modes. The cases shown in Figures 4.1(c) and (d) represent the excitation associated with non-zero overlap integrals for totally symmetric modes with a displacement in the potential field. In practice a significant change in the vibrational energy state occurs only when there is a displacement of the potential energy minimum, therefore case (d) is considered most important [Clark and Dines, 1986]. If the displacement of the potential minimum is large enough, then the A-term resonant Raman scattering can result in overtones with intensities that are comparable to the fundamental.

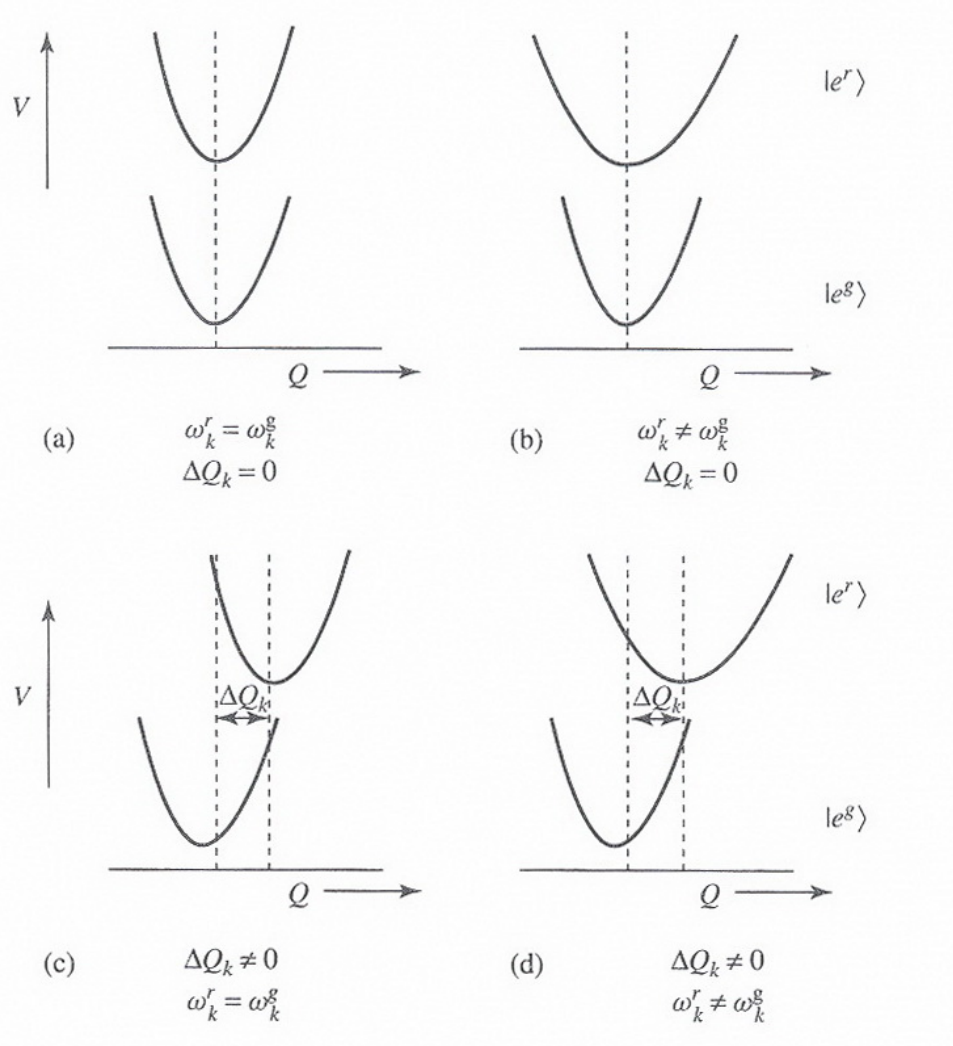


Figure 4.1. Four conditions for A-term scattering [Long, 2001].

The *B*-term resonant scattering is the result of vibronic coupling of the resonant excited state $|v_e^r\rangle$, to one other excited state $|v_e^s\rangle$ [Long, 2001]. Similar to the *A*-term, the *B*-term depends on non-zero overlap and transition integrals, as well as on the intensity of the vibronic coupling h_{se}^k and upon the difference between the coupled states $\Delta\tilde{\nu}_{es}$. The *B*-term is usually smaller than the *A*-term, however if the resonant transition yields zero, or near zero displacements of the potential minimum then only the diagonal overlap integrals are non-zero and as such the *A*-term is

vanishing. [Clark and Dines, 1986]. For times when the A-term is zero, the B-term may be the only significant contribution to the resonance Raman scattering, and in this case the diagonal overlap integrals are important. These integrals are only non-zero for $\nu_i^{(g)} = \pm 1$; therefore only fundamental Raman shifts are observed, so that there are no overtones. An extension of this idea, known as the ‘low temperature limit’, occurs when upper vibrational levels are not populated. Thus, $\nu_i^{(g)} = 0_i^{(g)}$ and $\nu_f^{(g)} = 1_f^{(g)}$, and only these two products contribute. In this case, we can remove the summation over the terms in B-term from the vibrational overlap integrals [Long, 2001] yielding,

$$\begin{aligned} [\alpha_{\rho\sigma}]_{fi}^B = & \frac{1}{h^2 c^2} [\mu_\rho]_{ge}^0 [\mu_\sigma]_{eg}^0 \frac{h_{se}^k}{\Delta \tilde{\nu}_{es}} \frac{\langle 1_f^{(g)} | Q_k | 0_r^{(e)} \rangle \langle 0_r^{(e)} | 0_i^{(g)} \rangle}{\tilde{\nu}_{ri} - \tilde{\nu}_o - i\Gamma_r} \\ & + \frac{1}{h^2 c^2} [\mu_\rho]_{ge}^0 [\mu_\sigma]_{eg}^0 \frac{h_{es}^k}{\Delta \tilde{\nu}_{se}} \frac{\langle 1_f^{(g)} | 1_r^{(e)} \rangle \langle 1_r^{(e)} | Q_k | 0_i^{(g)} \rangle}{\tilde{\nu}_{ri} - \tilde{\nu}_o - i\Gamma_r}. \end{aligned} \quad [4.11]$$

4.7 Summary

The intensity of non-resonance Raman scattered lines depends on the intensity of the incident radiation, the fourth power of the frequency, and the magnitude of the transition polarizability tensor $[\alpha_{\rho\sigma}]_{fi}$. The magnitude of the transition polarizability tensor is controlled by the overlap integrals, and their contribution is even more important in the case of resonance-Raman scattering. In the resonance Raman case the proximity of the excitation frequency to the electronic absorption peak ($\tilde{\nu}_{ri} - \tilde{\nu}_o$) provides the resonance coupling enhancement. As the excitation frequency approaches the absorption frequency, a minimum in the denominator occurs that

results in the large enhancements of the resonant Raman scattered intensity. The *A*-term resonance Raman scattering results in the observation of strong fundamental line intensities, and can also result in equally strong overtones in the Raman spectra. The *B*-term resonance Raman scattering is limited to fundamental modes and is typically a weaker phenomenon. Table 4.1 shows a comparison that summarizes the Raman and resonant-enhanced Raman scattering [Smith and Dent, 2005].

Table 4.1. Summary of Raman and Resonant Raman [Smith and Dent, 2005]

Raman Scattering	Resonance Raman Scattering
<i>B</i> -Term effective	<i>A</i> - and <i>B</i> -term effective
No overtones	Overtones common
More modes observed in the spectrum	Some modes selectively enhanced
No electronic information	Electronic information present
Weak scattering	Stronger scattering

Chapter 5: Raman and Resonance-Enhanced Raman Spectroscopy: The Experimental Setup

Townes and Schawlow first discovered stimulated emission with the invention of the MASER in 1953. Seven years later, Theodore Maiman demonstrated the first LASER by shining a high-power flash lamp on a ruby rod that had silver-reflective coated surfaces. After the invention of the laser, it was often said that the “laser is a solution looking for a problem.” This is certainly no longer the case, as lasers are often utilized in everyday life, from grocery store scanners to police speed measurement, to a plethora of applications within the medical fields. Lasers are also commonly used in the scientific and optical research fields because of their extremely narrow line width, as well as their temporal and spatial coherence. Lasers also have become the near perfect source for remote detection and for identification of chemical species.

In recent years, there have been increased research-and-development efforts focused on the ultraviolet region. There are two major reasons for this; first, the ultraviolet region has advantages of higher scattering cross-sections and reduced background and second, the costs of ultraviolet sources (lasers) and detectors have decreased while the quantum efficiency of the ultraviolet detectors has increased.

Utilizing the ultraviolet end of the spectrum for Raman study is appealing for a number of reasons. Each of the following advantages allows increased signal-to-noise performance, making detection and quantification of chemical and biological species easier. First, the Raman cross sections are proportional to ν^4 or λ^{-4} , so

decreasing the wavelength results in larger Raman scatter signals. Second, an important application of Raman scatter is for profiling species concentrations and atmospheric properties using lidar. Lidar is usually performed outdoors; as such, researchers are constantly working to overcome the signals from the solar background. The stratospheric ozone and molecular oxygen absorption provides a special spectral region known as the *solar blind* region for applications within the troposphere. Atmospheric ozone absorb so strongly in the UV-C ($\lambda < 280$ nm) that the solar radiation at the surface is non-existent, hence the name *solar blind*. Atmospheric ozone also absorbs most of the UV-B ($280 \text{ nm} < \lambda < 315$ nm) region, which also benefits atmospheric lidar measurements with increased signal-to-noise ratios. Finally, the deep UV region is appealing for use in Raman scattering because the fluorescence background no longer interferes for $\lambda < 280$ nm. This third advantage yields the opportunity to make use of ultraviolet excitation for resonance-Raman scattering. This research examines the opportunities for eventual development of resonance-Raman lidar techniques by studying the electronic absorption and scattering in both benzene and toluene.

5.1 Resonance Enhancement

Resonance-enhanced Raman scatter has been found in an array of chemicals [Asher, 1993; Behringer, 1974; Calleja and Cardona, 1978; Chen *et al.*, 1997]; few studies, if any, have used ultra fine-tuning (<1 nm) through the electronic absorption peaks of molecules. By using an OPO (Optical Parametric Oscillator) cavity to continuously tune through the electronic absorption bands of both benzene and

toluene, it has been possible to study the effects of a resonant enhancement with a tuning bandwidth as small as a fraction of a nanometer.

5.2 Experimental Setup Overview

As with many research endeavors it is important to be flexible when setting up an experiment. Throughout this research, it was necessary at times to rethink, redesign, and, in some circumstances, redo certain experiments, in order to improve the overall quality of the experimental results. Each step in the experimental process was not only crucial to the overall success, but it also provided an important learning opportunity. Each step in the experiment required addressing new problems that arose along the way, such as reducing the Rayleigh scatter signal, correcting a misaligned laser, repairing electronic hardware failures, investigating unknown Raman line interferences, among many other issues. Although each setback was incredibly upsetting, and at times seemed insurmountable, the problems yielded wonderful[†] opportunities to learn and adapt, to successfully complete the experiment.

The experiments to collect the Raman data were performed at the North Carolina State University Optics Lab in collaboration with the research group of Professor Hans Hallen. The Raman scattering experiment utilized a pulsed laser for excitation, which could be tuned to specific electronic absorption bands. The sample was held in a Teflon container with the incident radiation striking the input window at $\sim 45^\circ$ and scattering into a matched optical collection system. The lens coupling

[†] In hindsight, the problems provided opportunities to learn, although at the time these ‘wonderful’ opportunities were just awful.

system focused the light through the entrance slit into a triple monochromator for analysis.

5.2.1 Laser Excitation

An optical parametric oscillator (OPO) is a tunable laser cavity that is capable of generating a continuous wavelength scan of laser output. An OPO contains the basic assembly of a laser with cavity mirrors, a pump source, and an optical medium in which lasing occurs. The pump source in the case of our OPO is the 3rd harmonic of the Nd:YAG (neodymium doped into yttrium aluminum garnet) laser at 354.7 nm. Table 5.1 shows the harmonic wavelengths generated by the Nd:YAG laser. This pump laser beam is split within the OPO cavity into two other beams: a signal and an idler. A nonlinear interaction amplifies both the signal and the idler waves while the pump beam is reduced, as its energy is coupled into these two waves. This is considered as a three frequency interaction,

$$\omega_1 = \omega_2 + \omega_3,$$

where ω_1 is the pump, ω_2 is the signal, and ω_3 is the idler.

Table 5.1. Harmonic generation wavelengths of the Nd:YAG laser

Fundamental Wavelength (nm)	2nd (nm)	3rd (nm)	4th (nm)	5th(nm)
1064.0	532.0	354.7	266.1	212.8

The signal in our case is in the visible region (400 to 700 nm) while the idler is in the infrared (700 to 2200 nm). The lasing medium is a β -BBO (beta-barium borate) crystal, which is well suited for nonlinear generation because of its high nonlinear optical coefficients, as well as its high damage threshold ($>1 \text{ GW/cm}^2$). During our operation using the nonlinear crystals, the energy densities exceed 100

MW/cm². Figure 5.1 shows an overall layout of the excitation laser (individual images of the excitation laser are shown in Appendix D). Figure 5.2 shows a close-up view of the OPO cavity, and Figure 5.3 diagrams the operation of the OPO. At the center of Figure 5.3, the β -BBO crystal used as the tunable medium is schematically represented.

Tuning of the optical parametric oscillator is accomplished by changing the angle of the β -BBO crystal. Each wavelength is associated with a different phase matching condition, which is accomplished by changing the pathlength using a different phase matching angle. It is possible to tune the laser through the entire visible range by simply changing the angle of the β -BBO crystal over a range of about $\pm 5^\circ$. The approximate phase matching conditions for our OPO cavity are shown in Table 5.2, together with the wavelength of excitation in the ultraviolet.

Table 5.2. Phase Matching Angle of Optical Parametric Oscillator

Phase Matching Angle (Deg)	Pump (nm)	Signal (nm)	Idler (nm)	UV (nm)
25.1	354.7	423	2200	211.5
27.4	354.7	450	1682	225
30.1	354.7	500	1224	250
31.7	354.7	550	1001	275
32.5	354.7	600	869	300
32.9	354.7	650	782	325
33.1	354.7	700	720	350

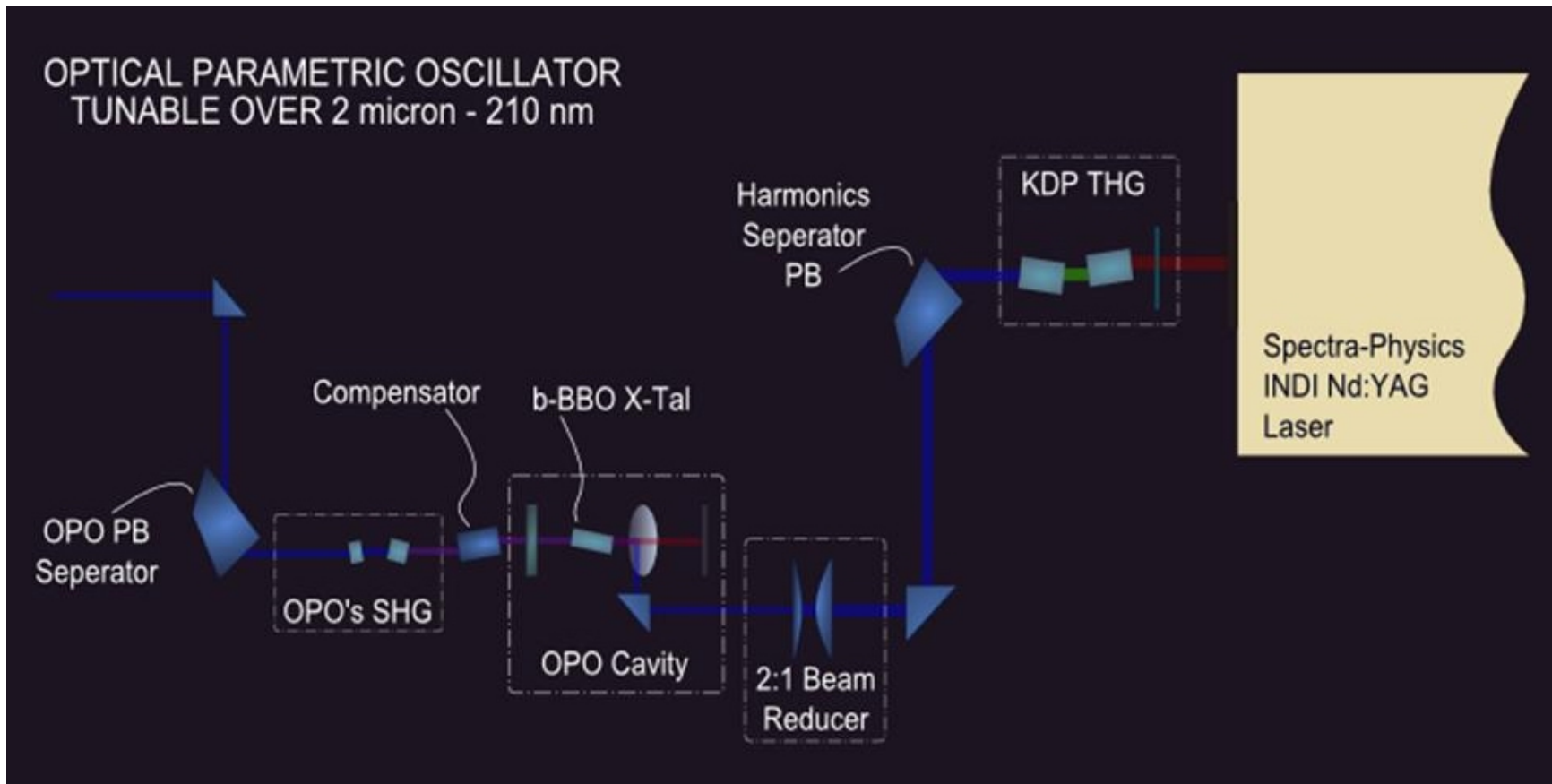


Figure 5.1. Excitation laser arrangement for Raman scattering setup [Chadwick, 2008]

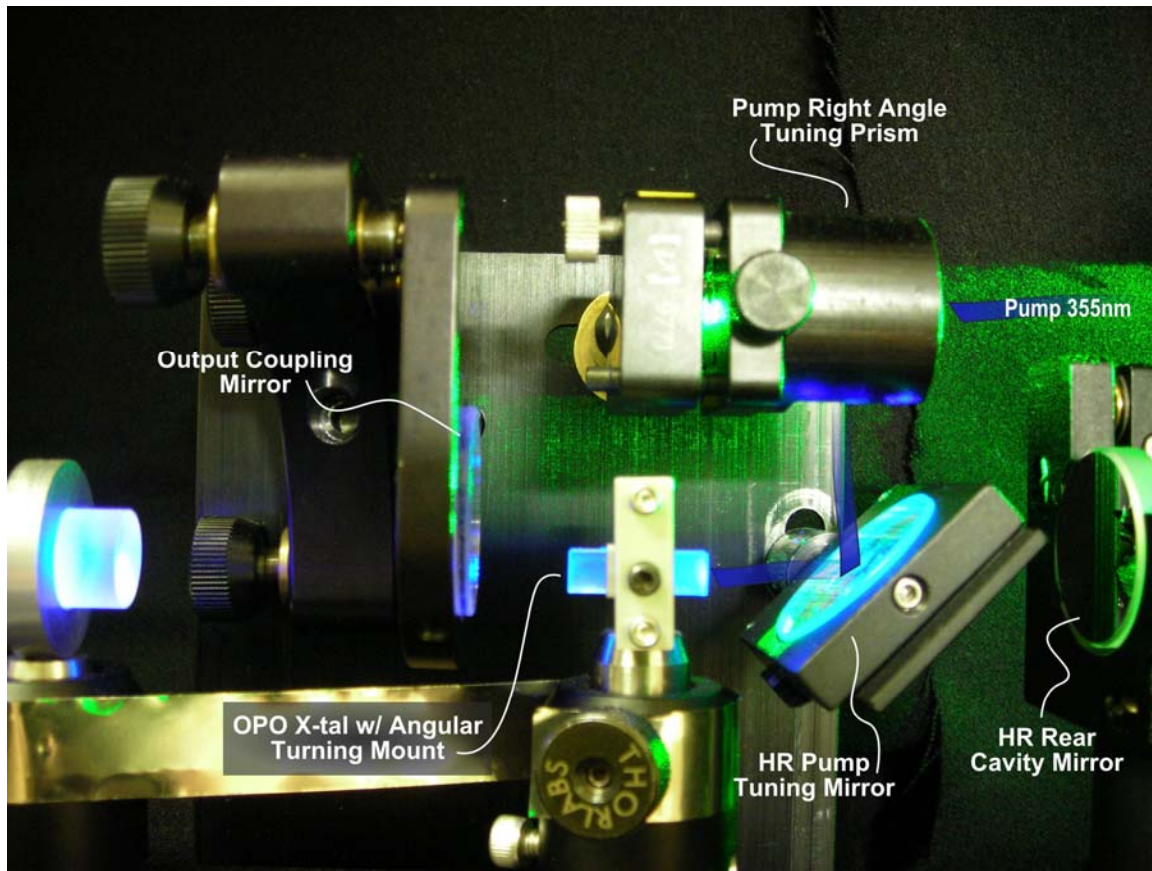


Figure 5.2. OPO Cavity at North Carolina State University laboratory

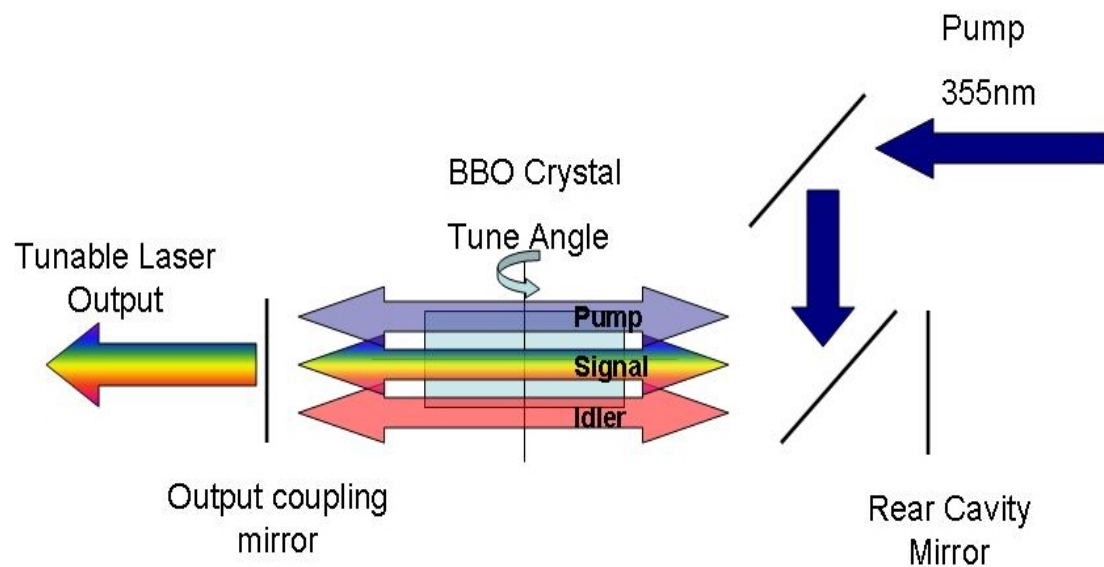


Figure 5.3. OPO Schematic

By tuning the angle of the β -BBO crystal, it is possible to generate the entire rainbow of laser wavelengths shown in Figure 5.4. However, the phase matching angle becomes increasingly more sensitive at the longer wavelengths because the energy steps become smaller (for constant wavelength steps). Although β -BBO is transparent below 420 nm, it is not efficient in generating laser output because the idler frequency is in the infrared at wavelengths longer than 2200 nm, where it is greatly attenuated (absorbed) within the β -BBO crystal (see the transmission curve for β -BBO in Figure 5.5). By tuning the OPO cavity we can continuously generate a visible laser output from approximately 420 nm to 710 nm. Using a second tunable β -BBO as a harmonic generator allows the visible output of the OPO cavity to be frequency doubled to yield an ultraviolet tuning range of approximately 210 nm to 355 nm.

The laser output had an average power of 1 to 2 mW (depending on wavelength) throughout the ultraviolet end of the spectrum, with a 10-Hz repetition rate and a 7-ns pulse duration.[‡] The power output of the laser was measured prior to each data run at each wavelength of excitation and varied by less than $\pm 5\%$ during the Raman data collection process. The OPO crystal used in the experiment is a type-1 β -BBO, which allows tuning throughout the visible region with very small changes in angle. Since the type-1 crystal has less stringent phase matching than a type-2 β -BBO crystal, it has a larger laser linewidth. Typical ultraviolet linewidths for the system are on the order of 30 to 50 cm^{-1} . This relatively large laser linewidth is troublesome when the Raman scattered lines are close to the elastically scattered line,

[‡] The laser repetition rate and pulse duration are controlled by the pump laser (third harmonic ND:YAG at 354.7nm)

or when the Raman scattered lines occur close to each other. With the large laser linewidth it may not be possible to distinguish two adjacent Raman lines, so the laser linewidth establishes the resolution limit for this system. The full-width half-maximum OPO laser linewidth at 240 nm was experimentally measured to be 0.25 nm ($\sim 44.45 \text{ cm}^{-1}$), see Figure 5.6.

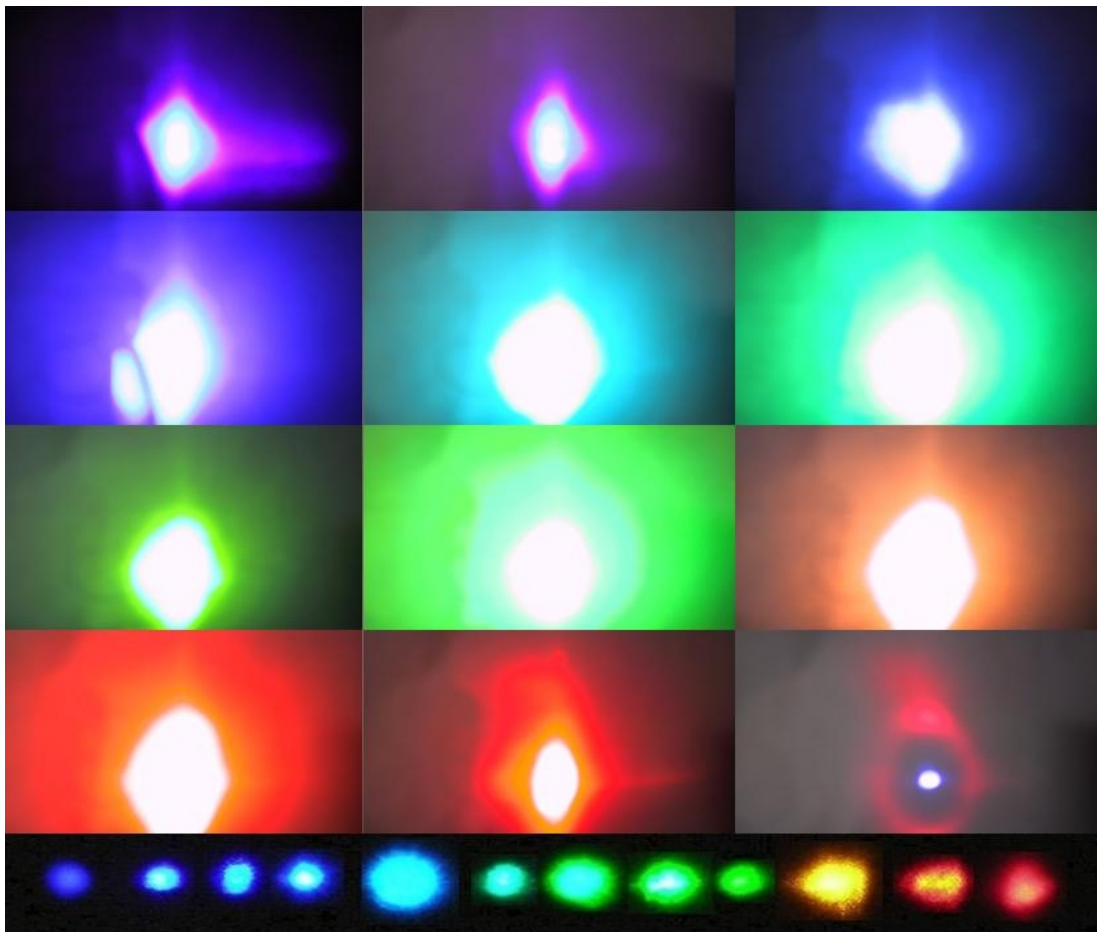


Figure 5.4. OPO laser output from North Carolina State University, shown for the wavelength range 420 to 710 nm (white center portions due to saturation of digital camera)

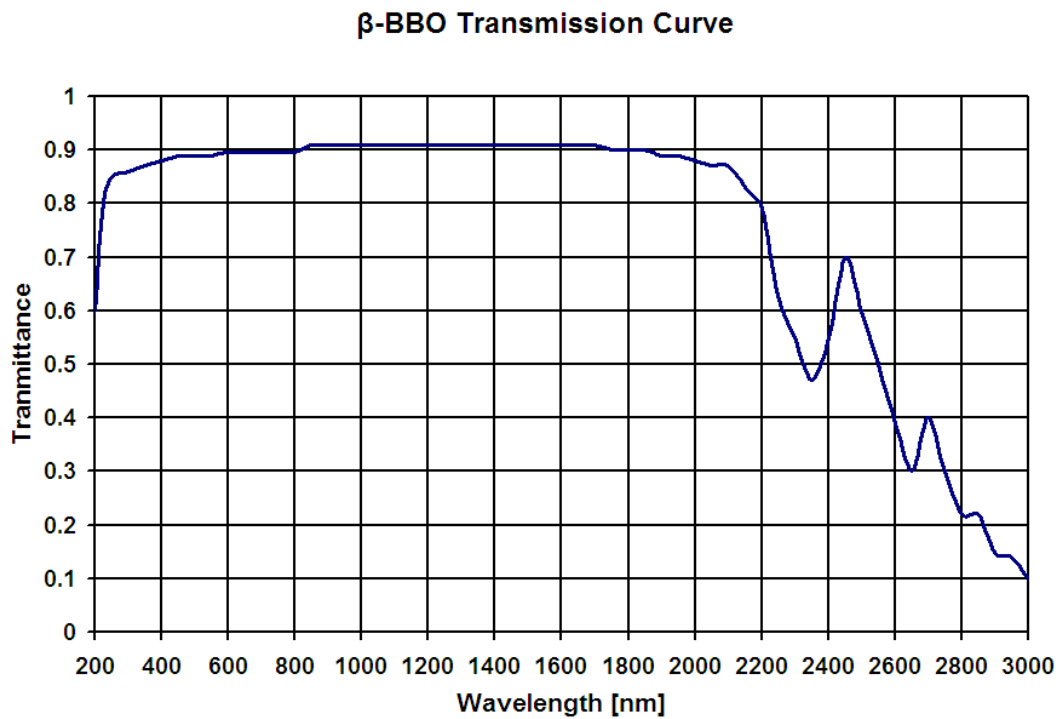


Figure 5.5. Typical β -BBO transmission curve

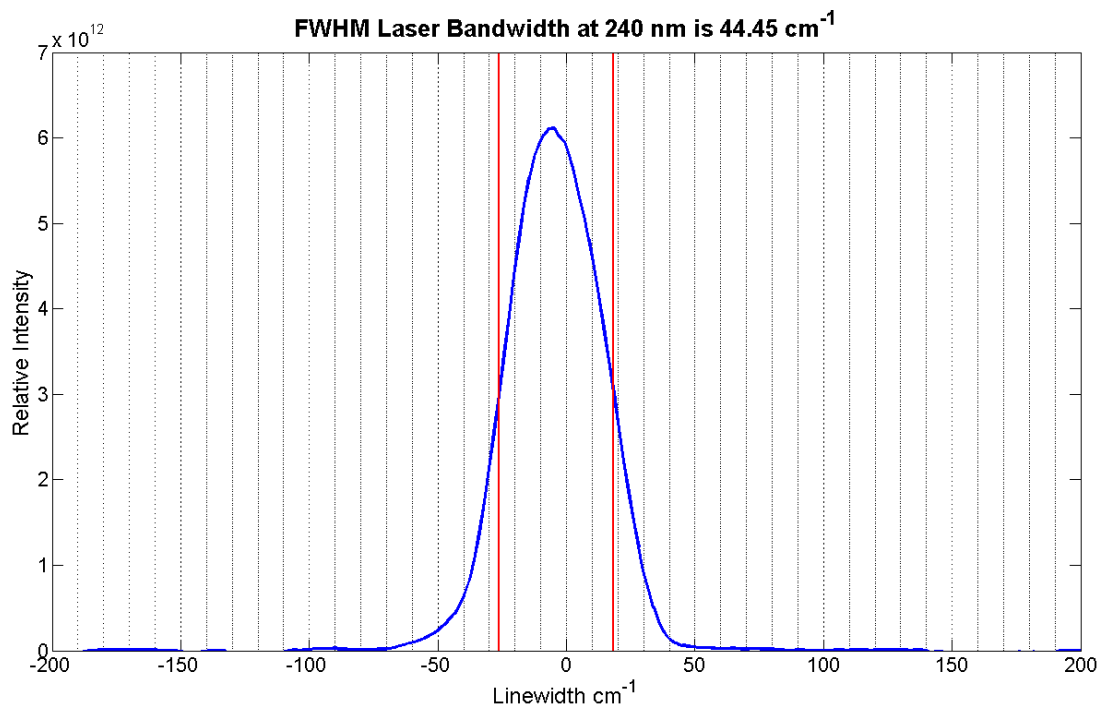


Figure 5.6. OPO laser linewidth at 240 nm, blue line is laser profile, the red lines represent the full-width at halfmaximum

5.2.2 Optical Scattering Arrangement

A 90° optical scattering setup was used to collect the Raman spectra. The incident laser illuminates the sample at approximately 45° with respect to the cell face normal, and the light entering the sample holder is scattered at 45° to complete a 90° angle. Collection of the scattered radiation is via a matched lens system to collimate and focus the scattered light into the spectrometer's entrance slit. Figure 5.7 shows a picture of the 90° arrangement of the Raman scattering setup, and Figure 5.8 is a schematic of the arrangement. Because the beam is coupled through a slit into the spectrometer, the most critical direction for optimum beam alignment is parallel with the input slit. In order to optimize coupling into the spectrometer, a UV (fused silica) right angle prism was mounted on a multi-axis mount allowing micro-adjusts of the beam position (see Figure 5.8). The optimum collection efficiency was found through the maximization of the Rayleigh scattered light. By adjusting the position of the incoming laser, it was possible to maximize the intensity on the CCD detector. Along with adjusting the laser position, the spectrometer's entrance slit-width was decreased, by adjusting both the input slit and the laser position, the optimal coupling is achieved.

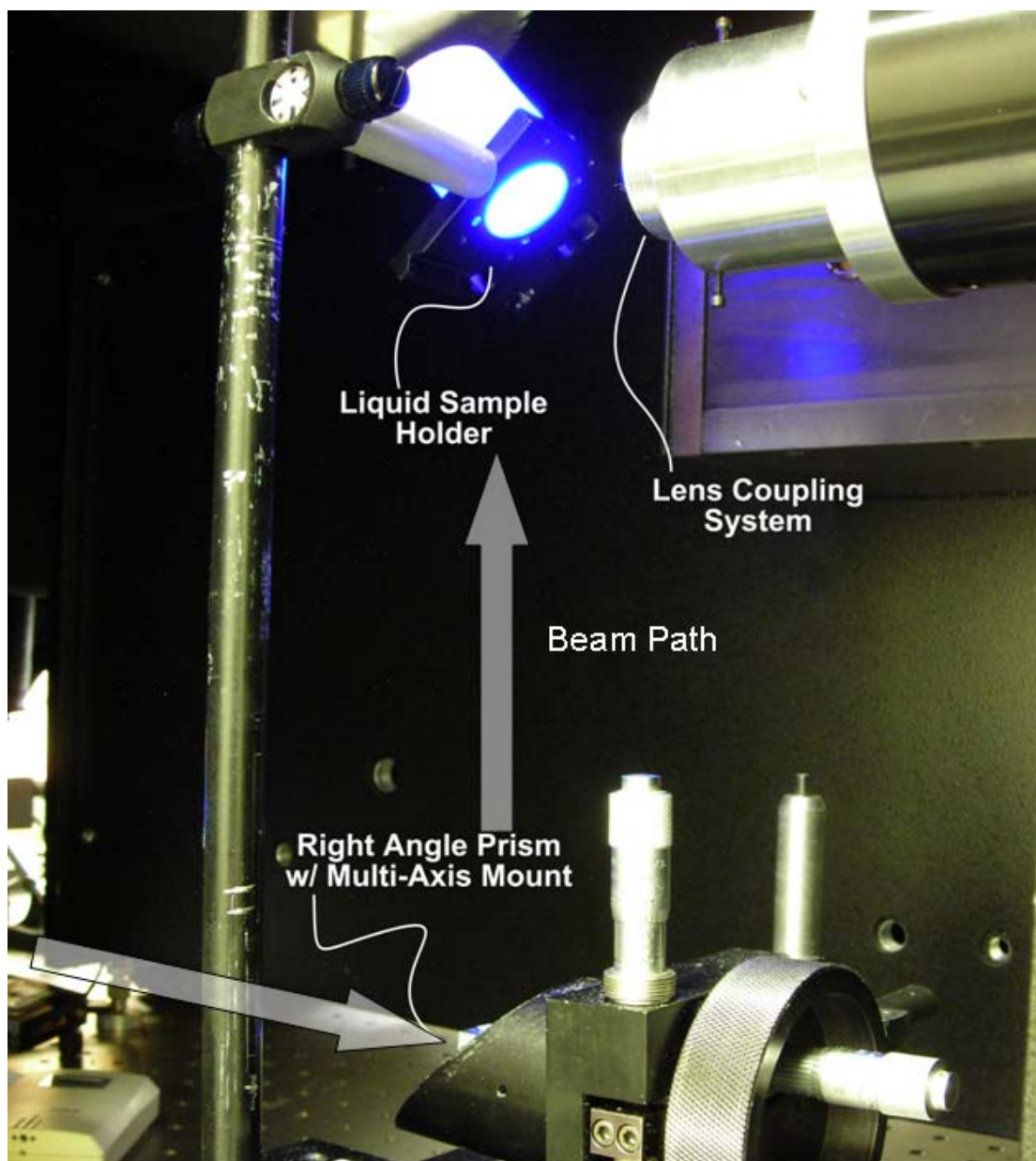


Figure 5.7. Arrangement of the 90° Raman scattering setup with 430 nm excitation

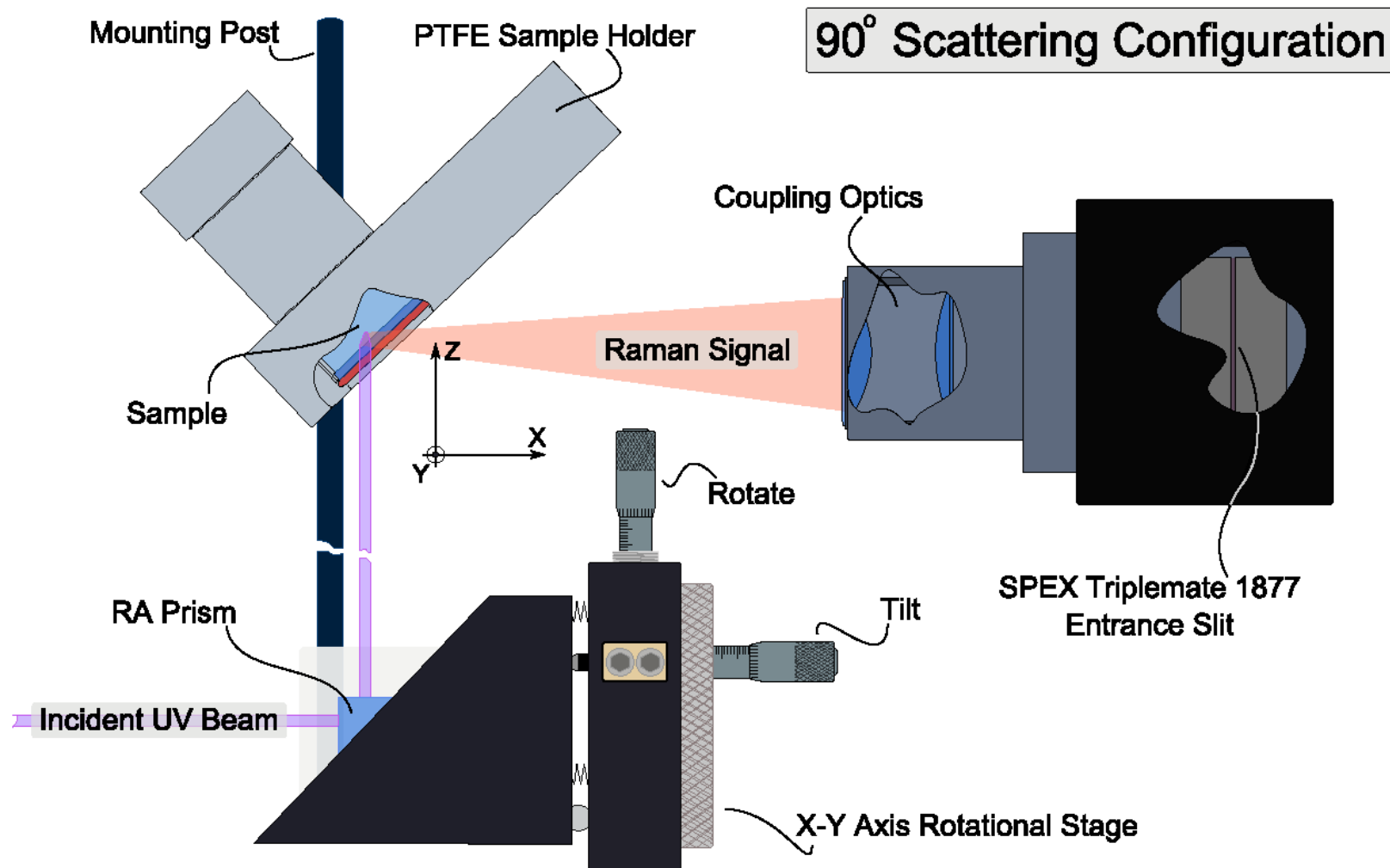


Figure 5.8 Optical scattering schematic [Chadwick, 2008]

5.2.3 Spectrometer Basics

To measure the Raman spectra, it is necessary to separate the spectral orders of scattered light and to analyze the wavelength distribution. The separation of the scattered light is accomplished using a reflection-type diffraction grating spectrometer that separates the diffracting orders as indicated in Figure 5.9.

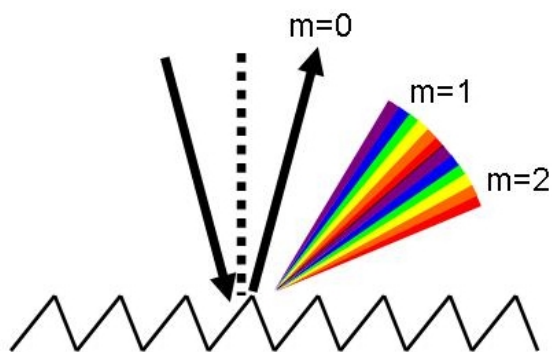


Figure 5.9. Reflection-type diffraction grating

The diffraction angle is dependent on both the wavelength of the light, the grating groove spacing, and the angle of incidence. The diffraction pattern that results for a single wavelength is a periodic array of minima and maxima that satisfy the interference criterion,

$$\sin(\theta_m) = \sin(\theta_i) + m \frac{\lambda}{d},$$

where,

θ_m is the angle of diffraction for the m^{th} order,

θ_i is the angle of incidence,

d is the distance between diffraction slits[§],

m is the diffraction order.

[§] Diffraction gratings are typically labeled with #grooves/mm, e.g., 2400 gr/mm

The diffraction order must be an integer value, and there are regions where second-order diffraction patterns will partially fall on top of first-order diffraction patterns. By using a visible blazed grating in its second-order diffraction mode, ultraviolet wavelengths of 200 to 300 nm will diffract in the same angular range as 400 to 600 nm in the first order. When using a diffraction grating in the second-order mode, there may be interference from the first-order diffraction, if the visible wavelengths are present. If one is detecting the scattered light using a CCD camera that is sensitive to both visible and ultraviolet, then may not be possible to distinguish between the different overlapping lines. After angular separation, the light is then spatially separated over the length of the spectrometer and detected in the CCD imaging area.

During our experiments, two different spectrometers were used. Initially a 1/3-m single-stage spectrometer was used. Because of its limited resolution, however, it was difficult to measure the low-energy Raman shifts near the strong Rayleigh scatter line. Following the initial experiments, the smaller 1/3-m spectrometer was replaced with a three-stage, Jobin Yvon Spex Triplemate 1877, 0.6-m spectrometer.

5.2.4 Jobin Yvon Spex Triplemate 1877

The triple Jobin Yvon Spex Triplemate 1877 spectrometer is a three-stage spectrometer. The first two stages are utilized to filter and remove stray light particularly the strong Rayleigh (elastic) scattering signal from the optical path, see

Figure 5.10. The third stage is the spectrometer stage used to separate the wavelengths for measurement of the Raman spectra and is shown Figure 5.11.

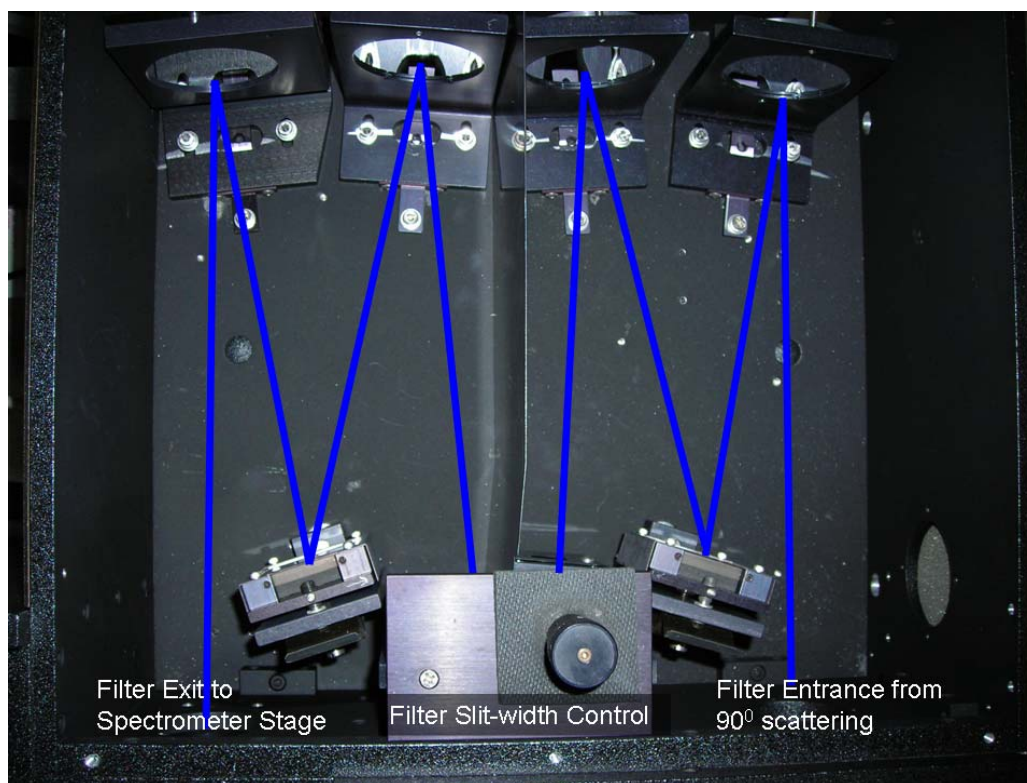


Figure 5.10 Filter stage of Spex Triplemate 1877

The Spex Triplemate spectrometer is able to achieve out-of-band blocking on the order of 10^{14} , and this property makes it ideal for Raman spectroscopy, particularly when the removal of the strong Rayleigh scatter is necessary. When using an imaging CCD camera, it is not possible to fully eliminate the background signal by decreasing the filter slit width. As the slit width is diminished in size, the stray light rejection becomes more effective; however, the field of view of the camera is constricted, and the edges of the CCD camera active area may no longer be illuminated.

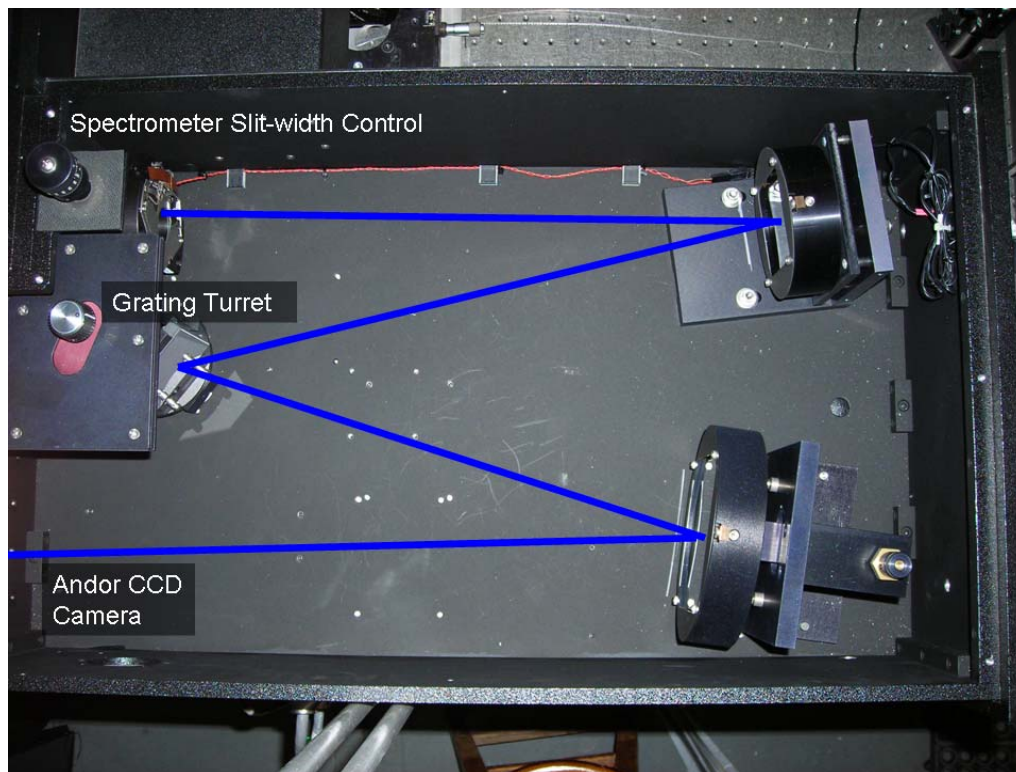


Figure 5.11 Spectrometer Stage of Spex Triplemate 1877

The filter stage works exceptionally well when the detection system is a single output slit onto a photomultiplier tube. When it is necessary to maintain an illumination width on the CCD camera however, there is a practical limit to the slit size. Typical Raman scattering experiments use a single excitation wavelength, which makes it possible to remove the Rayleigh line scattering by using a holographic notch filter, which has a very narrow stop band centered at the excitation wavelength. When using a tunable laser, it is not possible to use a holographic notch because of the constant change in the excitation wavelength, as well as due to the prohibitive cost of maintaining a large array of notch filters.

Ultraviolet enhanced coatings were used on the reflecting surfaces of all optics, to maximize throughput in the operating region. An earlier application of the

same model Spex Triplemate has been estimated to have an overall throughput efficiency of 7% [Asher, 1993]. The trade-off to improve signal-to-noise ratio with the rejection of the Rayleigh line, and reduction of other stray light, is well worth the relatively low overall throughput. The throughput versus wavelength for our Spex Triplemate 1877 spectrometer has been modeled by C. T. Chadwick [2008] and is shown Figure 5.12. The modeled peak in the throughput calculation results in an efficiency of almost 15% at 250 nm.

The Spex Triplemate 1877 spectrometer stage (third stage) has a turret with three different gratings: 1200 gr/mm, 2400 gr/mm, and 3600 gr/mm. Each of the three gratings has both advantages and disadvantages. The most notable difference is in the range over which the spectrometer can be operated, as presented in Table 5.3.

Table 5.3. Spectrometer Operating Range

Grating	1200 gr/mm	2400 gr/mm	3600 gr/mm
Spectrometer Operating Range	0 – 1000 nm	0 – 500 nm	0 – 333 nm

The spectrometer operating range is determined by the number of grating grooves per millimeter. In order to achieve the highest resolution, it is necessary to use the largest number of grooves per millimeter; however, the operating range becomes constricted and so we chose to use the 2400 gr/mm grating. This grating made it possible to take high resolution spectra in both the visible and ultraviolet wavelength regions; thus, it was possible to obtain measurements in both the resonant and non-resonant regions for determining the magnitude of resonance-enhanced Raman scatter. Two different gratings could have been used; however, it would become necessary to recalibrate the system every time the grating was changed.

The grating choice also determined the range of wavelengths that the CCD camera would see in a single image. When using the 2400 gr/mm grating, the CCD camera had a measured wavelength range of 5.7 nm. Because the camera has a square chip with 512×512 pixels, the theoretical resolving limit is:

$$\frac{5.7 \text{ nm}}{512 \text{ pixels}} = \frac{0.01 \text{ nm}}{\text{pixel}}.$$

As was mentioned earlier, however, the actual resolution is limited by the relatively large bandwidth of the OPO. Also, the spectrometer's manual states that the resetability of the spectrometer is no worse than $\pm 0.2 \text{ nm}$ ($\pm 30 \text{ cm}^{-1}$ at 260 nm); experimentally we found the resetability to be $\pm 0.04 \text{ nm}$ ($\pm 6 \text{ cm}^{-1}$ at 260 nm).

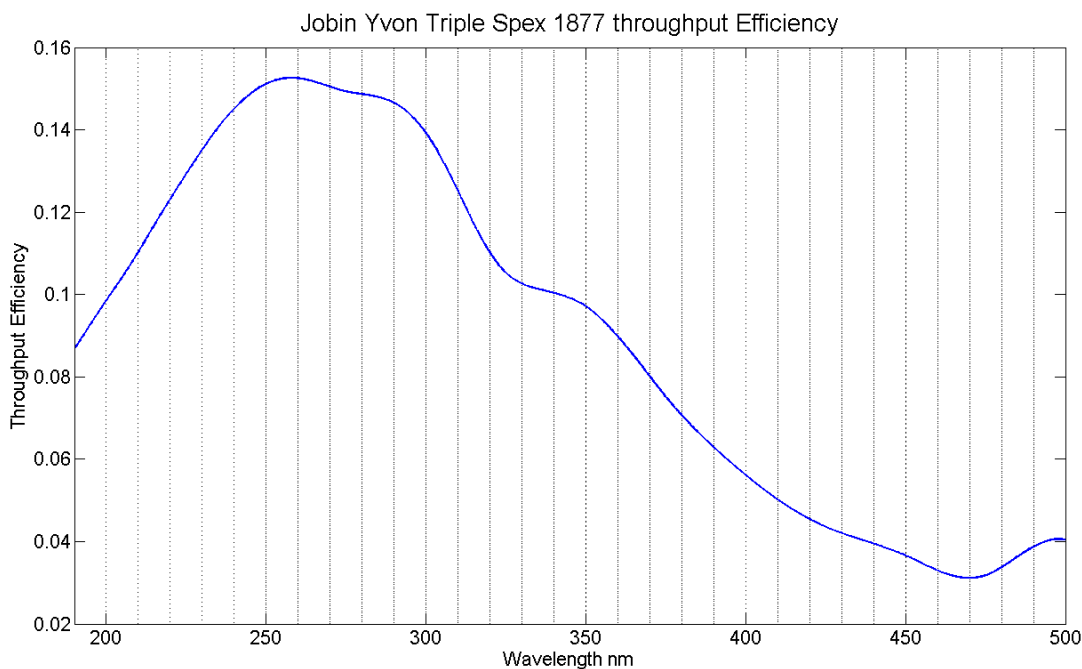


Figure 5.12 Spex Triplemate 1877 overall throughput efficiency [Chadwick, 2008]

5.2.5 CCD Camera

The data were taken collected an EM-CCD (Electron Multiplying-Charge Coupled Device) camera from Andor. The EM-CCD was chosen for two primary

reasons; the camera has extremely low dark counts and has a very high quantum efficiency ($\approx 35\%$) through the ultraviolet region. Figure 5.13 shows the Andor IXON back-illuminated EM-CCD camera's quantum efficiency curve.

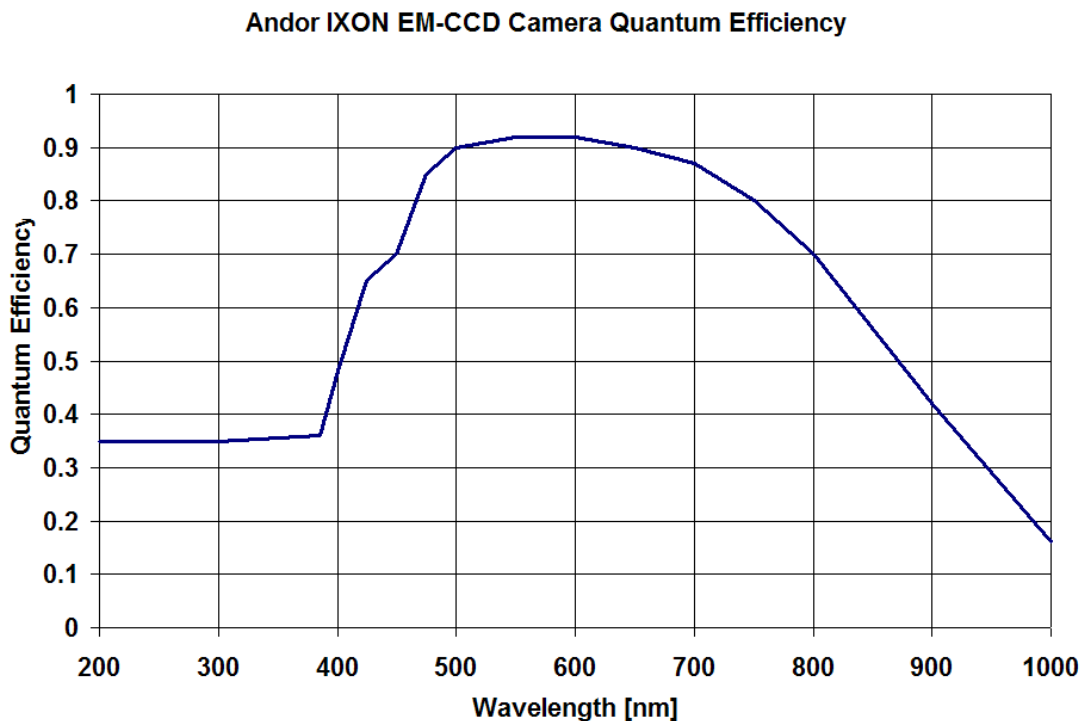


Figure 5.13 Andor Ixon EM-CCD quantum efficiency

5.2.6 Spectrometer Calibration (Mercury Lamp)

The spectrometer was calibrated using a low-pressure mercury vapor lamp. This lamp was chosen because of its strong ultraviolet emission lines at precisely known wavelengths. The mercury vapor emission lines provide a simple way to calibrate the spectrometer for accurate wavelength positions. The strongest line at 253.65 nm was used to calibrate the spectrometer stage and to center the camera's field of view. Weaker lines in the 290 nm region were used to calibrate the filter stage. Figure 5.14 shows four lines from the mercury lamp that are ~ 0.2 nm apart.

Appendix C provides a list of the ultraviolet mercury vapor emission lines from the National Institute of Standards and Tables.

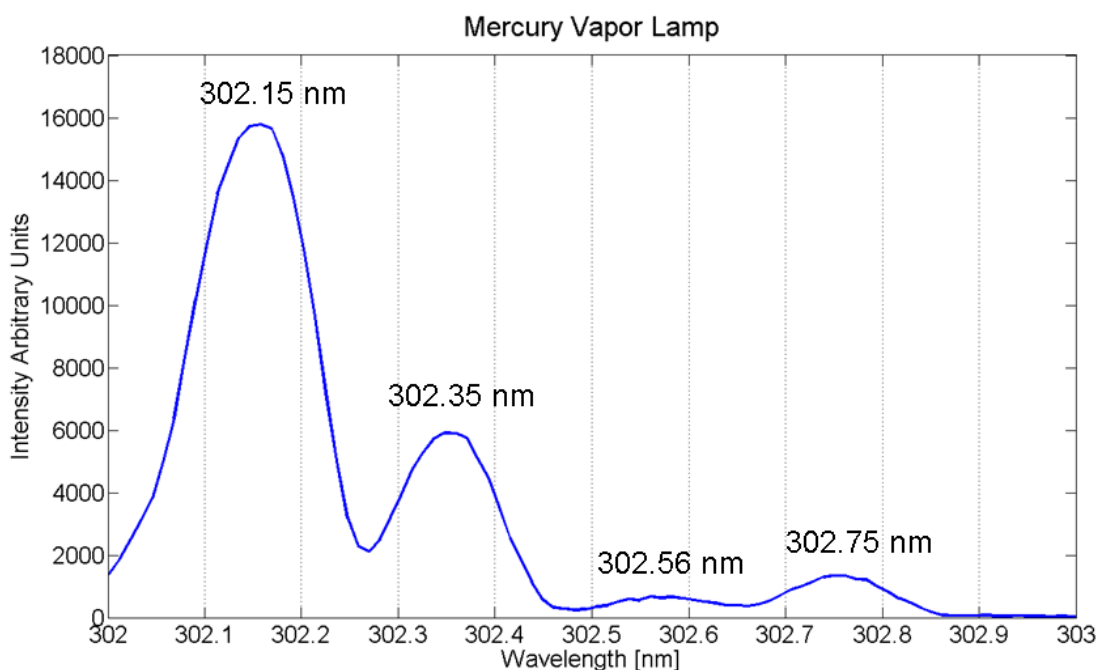


Figure 5.14 Mercury vapor lamp spectra 2400gr/mm Spex Triplemate Spectrometer

Once the calibration was performed using the mercury vapor lamp, a separate confirmation of the calibration was performed using a known laser wavelength and a diamond sample. Diamond is commonly used for such purposes because of its strong single Raman scattering component at 1331 cm^{-1} . Figure 5.15 shows the rough cut diamond; the bluish color observed is due to its fluorescence. Figure 5.16 shows the Raman scattering spectra measured when the diamond was excited by 260 nm radiation. The observation of the Raman line of diamond at 1331 cm^{-1} confirms the proper calibration of the spectrometer. It also should be noted that throughout the experiment, many other chemicals (*n*-heptane, Teflon, naphthalene, beta-carotene, and water) were measured and compared with known and well documented Raman

spectra. The spectra of each were analyzed, and all were also found in wavelength agreement; thus, giving more confidence in the calibration of our spectrometer during the experiments.

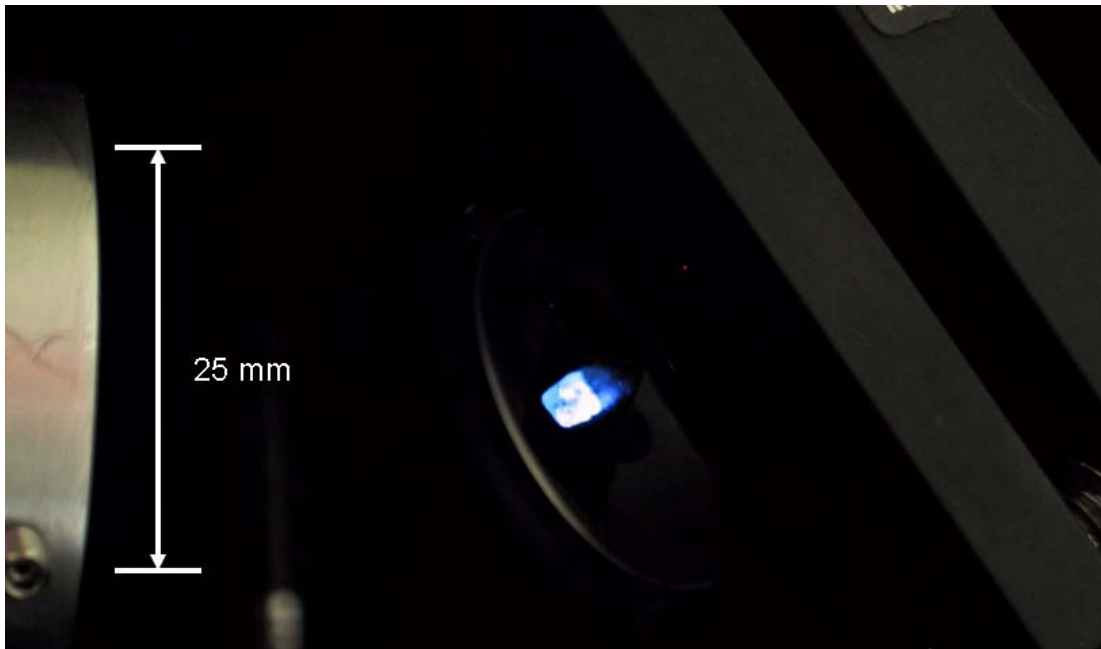


Figure 5.15. Rough diamond for calibration, color observed is due to fluorescence

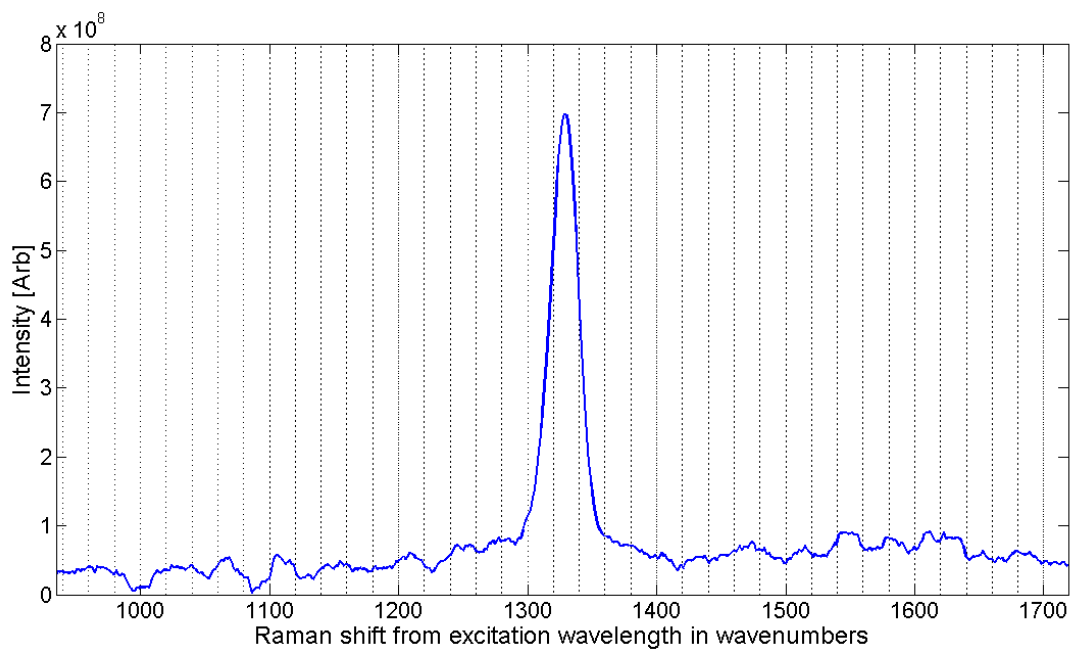


Figure 5.16 Raman scatter from diamond with 260 nm excitation

5.2.7 Sample Holder

Two different sample holders were used for the Raman scattering experiment; they are shown in Figure 5.17. The first sample holder was a Teflon container with a sapphire window, and the back was plugged with a Teflon stopper (see left side of Figure 5.17). A second sample holder shown on the right side of Figure 5.17, was made using Teflon housing and two sapphire windows. Appendix E shows more detailed pictures of the sample holders. Close examination of Figure 5.17 shows a metallic center on the left side; this is a piece of aluminum foil used to prevent Raman scattering from Teflon holder. Initial experiments found a strong set of unknown Raman lines in the recorded spectra, these were found to be from the Raman scatter of the Teflon case. The Raman spectrum measured is shown in Figure. 5.18 with a comparison to the Raman spectra of Teflon collected by Sedlacek *et al.* [2001]. The aluminum foil eliminated the Raman scatter from the Teflon surface of the sample holder.

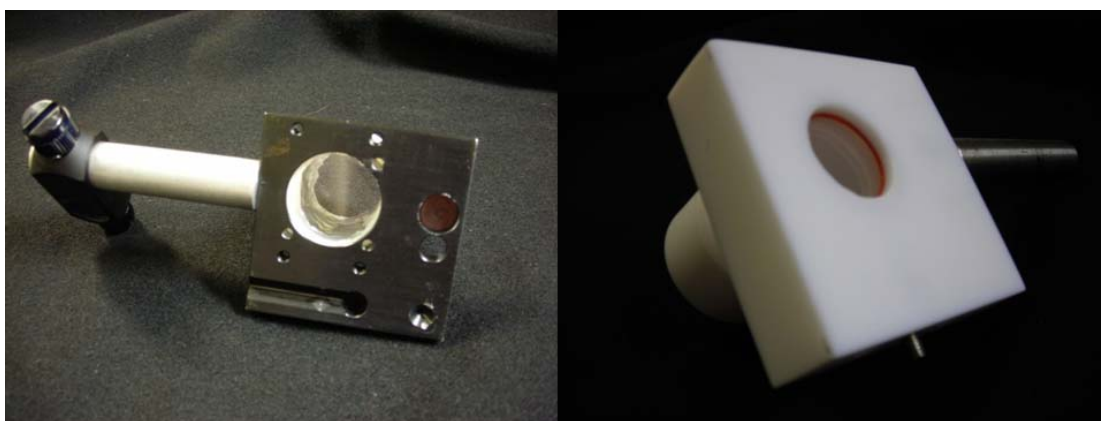


Figure 5.17. Sample holders with open back and Teflon stopper removed (left), and dual window (right)

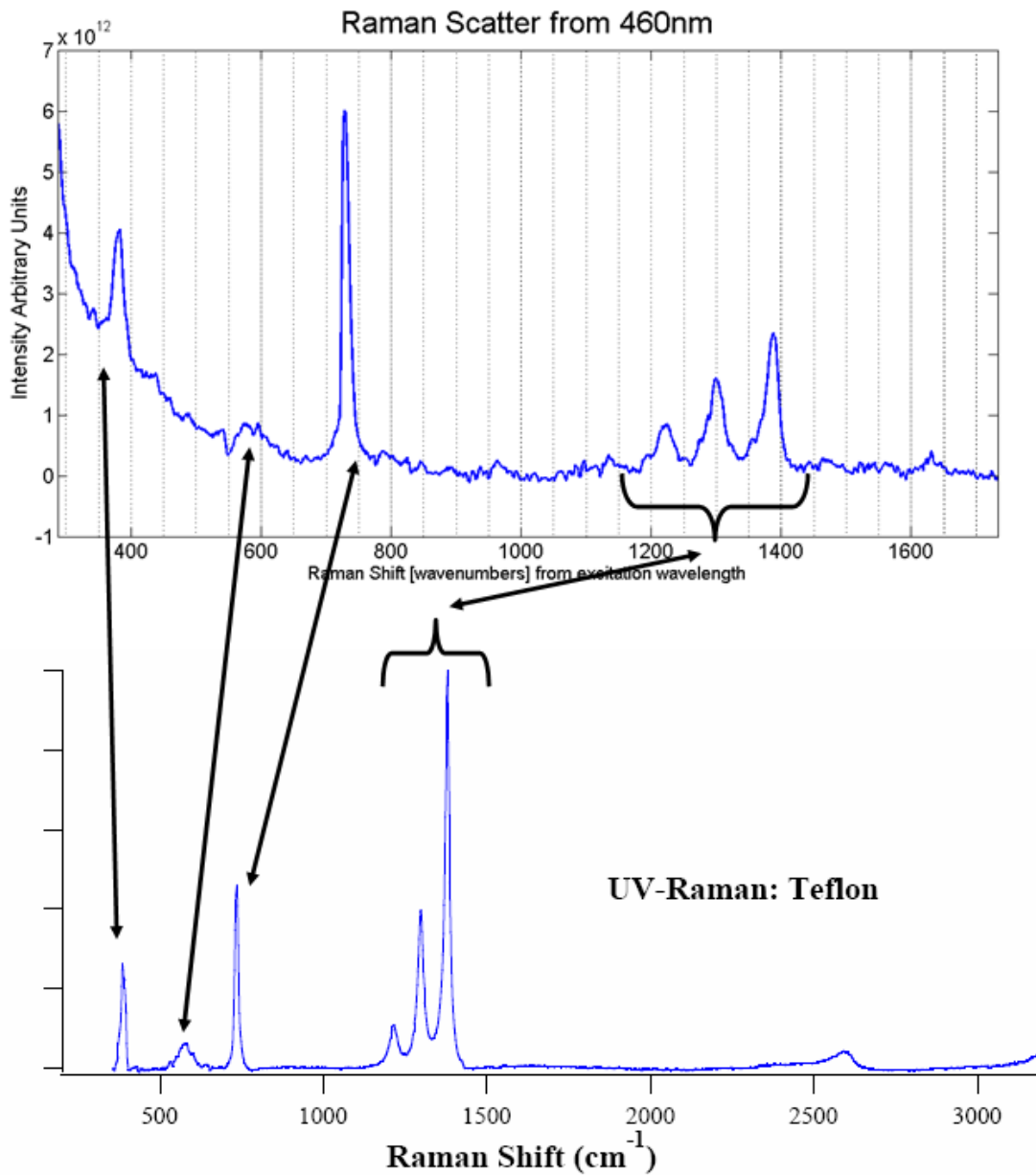


Figure 5.18. Raman Spectra of Teflon as collected in this experimental setup (top), and a comparison to the Raman spectra of Teflon collected by Sedlacek *et al.* [2001] (bottom)

The dual window sample holder was constructed to be used as a 90° scattering sample holder and an absorption cell (see Figure 5.19). Simple measurements of the

absorption coefficients were made possible by taking laser power measurements.**

The laser power was first measured without any sample inside the holder and then the measurement was made a second time with a known amount of the absorbing species.

Using the known concentration and pathlength made it possible to calculate the absorption coefficient at the laser wavelength. Sapphire was chosen as the window material because of its high transmission throughout the ultraviolet and visible regions. The Sapphire windows maintain higher than 90% transmission from 200 nm to 1000 nm.

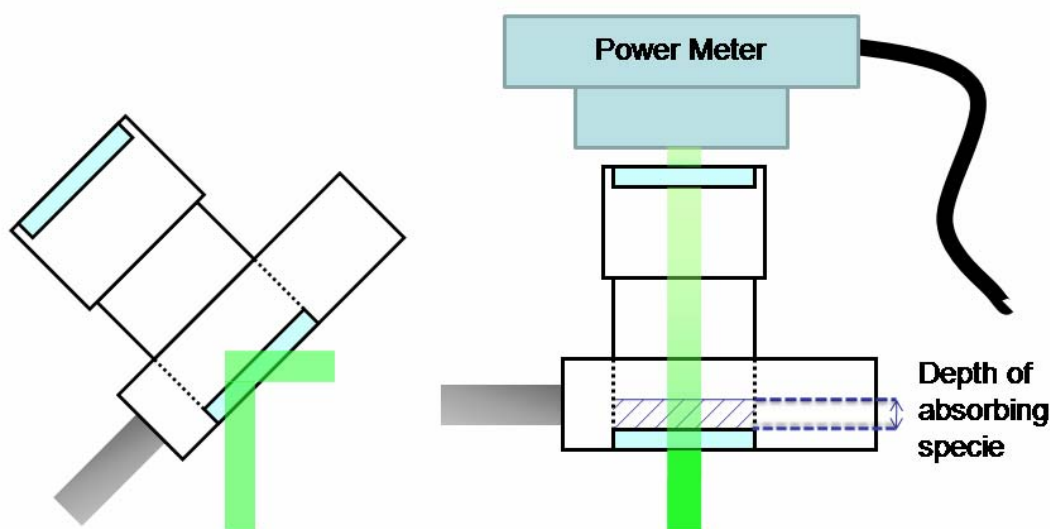


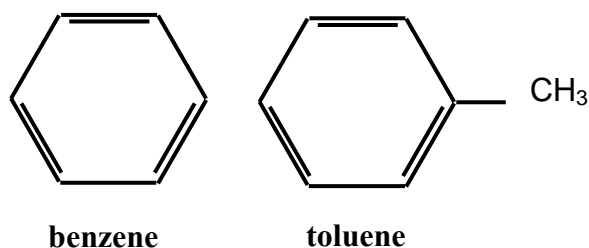
Figure 5.19. Teflon sample holder in 90° scattering configuration (left) and absorption measurement configuration (right)

5.2.8 Sample Handling and Preparation

The samples used for the Raman scattering experiment were HPLC-grade chemicals obtained from Sigma Aldrich and no further purification was performed.

** 30-s average power measurements were made in order to reduce the error created by the pulse-to-pulse power fluctuations that are typical in a pulsed laser system.

Because benzene and toluene are both aromatic hydrocarbons, they were handled with the use of gloves, eye-protection, and dual cartridge organic vapor filter masks, as well as added ventilation in order to prevent any inhalation. A small portion of the chemical was moved to a secondary storage container in order to prevent back contamination, and pipettes were then used to measure and dispense the fluid into the sample holders. Depending on the required concentration of the chemical, different amounts were diluted in *n*-heptane. For example, in order to create a 1 molar (1 mol of solute in 1 liter of solvent) solution of benzene in *n*-heptane, one must dissolve 88.77 ml in 1 liter of *n*-heptane. Only tens of milliliters were needed during the experiment, and a significantly smaller amount of solution was made. Therefore a 1 molar solution was made by mixing 0.8877 ml of benzene in 10 ml of *n*-heptane. The choice of *n*-heptane was made for two main reasons: (1) *n*-heptane is transparent in the ultraviolet and visible, and (2) toluene, benzene, and naphthalene are all soluble in *n*-heptane. A comparison of benzene's and toluene's molecular structure is shown in Figure 5.20. Both toluene and naphthalene are based on modifications of the benzene ring. Toluene has an added methyl group replacing a single hydrogen, and naphthalene consists of two benzene rings connected along a common carbon double bond. A variety of common solvents used for ultraviolet spectroscopy are listed in Table 5.4, along with their associated cut-off wavelength, which identifies the point of approximately 5% absorption. When the excitation or scattered light is smaller than the cut-off wavelength a different solvent should be utilized.



5.20 Molecular structures of benzene and toluene

Table 5.4. UV Cut-off Wavelengths for Common Solvents

Solvent	UV Cut-off Wavelength [nm]
water	195
n-heptane	200
acetonitrile	210
cyclohexane	210
diethyl ether	210
ethanol	210
hexane	210
methanol	210
dioxane	220
tetrahydrofuran	220
dichloromethane	235
chloroform	245
carbon tetrachloride	265
benzene	280
toluene	285
acetone	300

5.3 Summary

The resonance-Raman experiment required many hours of diligence to yield interesting results. The tunable ultraviolet laser must be perfectly aligned in order to yield appreciable laser energy. With confidence that the laser source is working properly, one then aligns the 90° scattering geometry in order to maximize throughput into the spectrometer, which has already been properly calibrated using a low pressure mercury vapor discharge emission lamp. After the system is aligned and calibrated, the sample is put into the scattering cell and measured using a viable

resonance excitation wavelength. This process begins with examining the high-resolution absorption spectra available for the molecule to select a wavelength region for the study. An appropriate narrow band absorption peak can be difficult to locate without high-resolution absorption spectra to use as a reference. By tuning the laser to an appropriate absorption peak the resonance-enhanced Raman scattering is investigated.

Chapter 6: Raman Data Processing: Noise Removal and Data Normalization

All of the data recorded by the Andor camera using the 90° scattering arrangement is pre-processed to remove bad pixels, noise and other unwanted phenomena using routines written in MATLAB. There are two primary goals of the initial MATLAB processing: the first is to remove noise and the second is to normalize the data for a resonance-enhancement gain calculation. The initial steps to remove the noise and the basic steps of normalization include assigning wavelengths, correcting laser power variation, adjusting detector integration time, accounting for spectrometer throughput, and including the quantum efficiency of the EM-CCD. Each of these topics are discussed in this chapter. The final step in the normalization process is the correction for absorption of both the excitation wavelength and the Raman scattered wavelength, and that calculation is discussed in detail in Chapter 7.

6.1 Preliminary Data Processing – Noise Removal

Noise removal is separated into two parts: the first part is the removal of any background, and the second part is the removal of bad or saturated pixels. The inherent detector background is removed using a dark image. The EM-CCD has a square active area with 512×512 pixels. Each pixel corresponds to a charge well and each well fills up with charge as the camera is exposed, based on its susceptibility. The accumulation of different dark count levels for each pixel is used to correct this effect from knowing the dark image exposure time. This dark image

intensity per unit time is then subtracted pixel by pixel from the data images resulting in a near-zero background. A second problem occurs in the case of longer exposures (1 minute or longer) when the presence of unwanted ‘meteors’ are observed (see Figure 6.1). The ‘meteors’ are saturated or nearly saturated pixels that tend to bleed through an entire row.

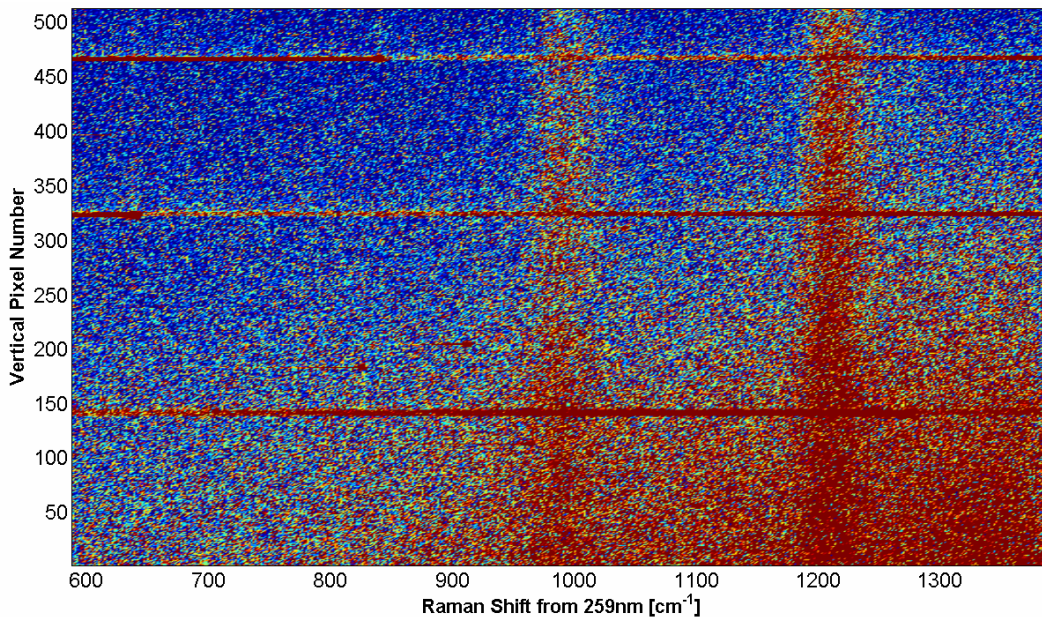


Figure 6.1. Raw camera image of liquid benzene Raman scatter with ‘meteors’ —the horizontal saturated stripes

‘Meteor’ removal is performed with a simple search algorithm that hunts for a row of nearly saturated pixels and removes them as well as the entire row that contained them. Only a few of the pixels are saturated in the images; however, when it occurs the entire row is affected by a blooming effect due to charge transport.

Figure 6.2 shows the result of removing the saturated pixels and their corresponding rows from the image shown in Figure 6.1.

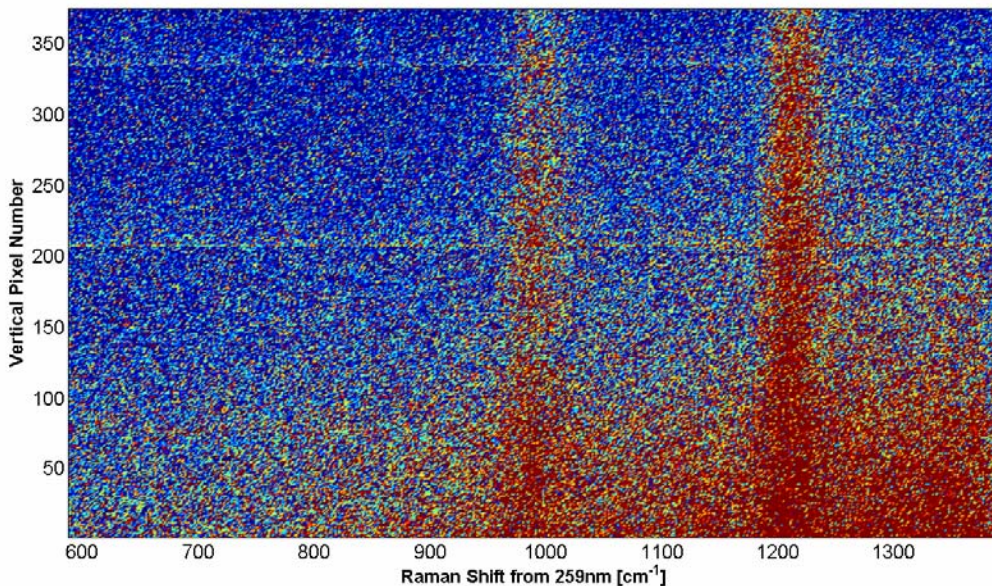


Figure 6.2. Processed camera image of liquid benzene Raman scatter with ‘meteors’ mostly removed

6.2 Signal Averaging

In order to improve the signal-to-noise ratio, signal averaging is performed on the collected Raman data. Each column represents the same wavelength and a vertical column average is applied to improve the Raman signal. Each vertical line is summed and then divided by the number of rows. It is important to take an average and to not merely sum the columns, because each image may contain a different number of ‘meteors’ resulting in a different number of usable rows. The result of the vertical average is shown in Figure 6.3. The data should also be normalized for relative sensitivity of the background levels at the focal plane. If meteors are found near the bottom of the image in the case of Figure 6.2, a removal of the intensity will may have an effect on the average of the spectrum; however, it has not been applied because of the uncertainties that would be introduced to the data.

6.3 Complete Raman Spectrum Presentation

Because the spectral field of view of the camera was limited to 5.7 nm, each CCD image captured only a small portion of the full Raman spectra that spans approximately 4000 cm^{-1} . At 260 nm, the spectral field of view of 5.7 nm corresponds to approximately 823 cm^{-1} , meaning that a set of five images must be taken (assuming perfect overlap) to span the entire 4000 cm^{-1} . Each individual image then contains a different portion of the Raman spectra; these data are pre-processed as individual images and then stitched together to form a complete picture of the Raman spectrum. Figures 6.1–6.3 above show the data collection of a single CCD exposure.

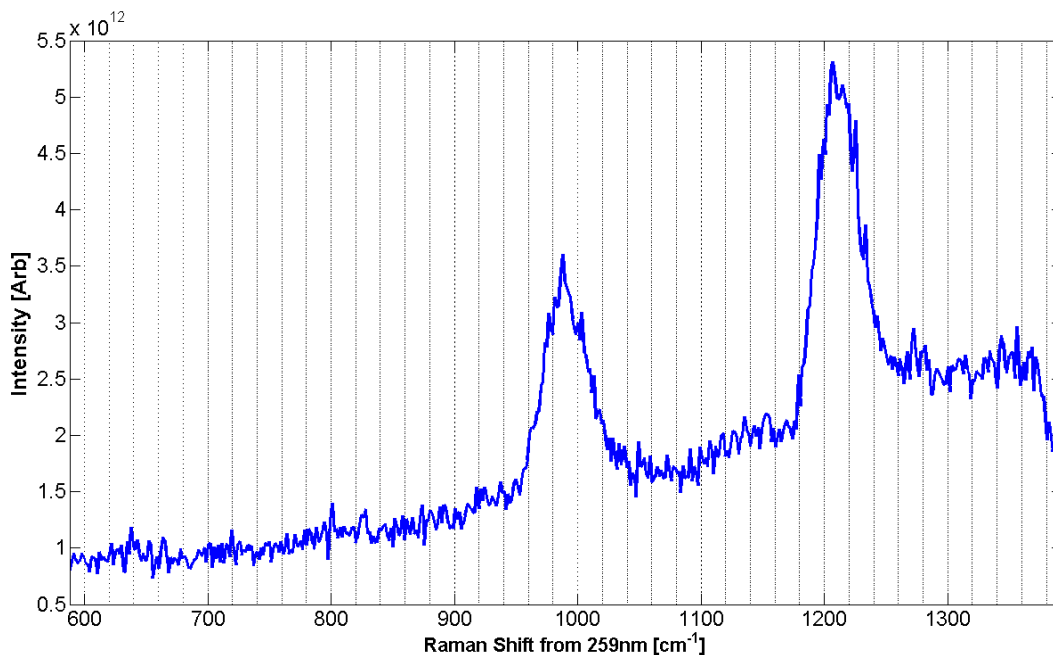


Figure 6.3. Vertical average of CCD image with ‘meteors’ removed

A Raman spectrum of benzene with resonance excitation is seen in Figure 6.4, it contains a set of nine separate images stitched together. Having this many images

insured sufficient overlap from one image to the next, thereby eliminating the chance for a missed spectral feature between images. The significantly higher intensity on the left side of the image ($< 700 \text{ cm}^{-1}$) is a result of the Rayleigh scatter contribution. Because the intensity of the Rayleigh scatter is so high, it interferes with the lower wavenumber Raman scattered lines, and it may even mask a part of the Raman spectra making some features impossible to detect. A second item of note is the drastic decrease in background around 1100 cm^{-1} , and is the result of two consecutive images having different background levels. This step change occurs where two images are stitched together at a point further away from the elastically scattered line, where the instrument has improved ability to reject stray light. As the filter (first) stage is moved to a different wavelength, there is a cutoff point –depending on filter slit-width– at which the filter stage can almost completely reject the Rayleigh scattered return. This point occurred somewhere between the two images around 1100 cm^{-1} causing the significant decrease in the background level.

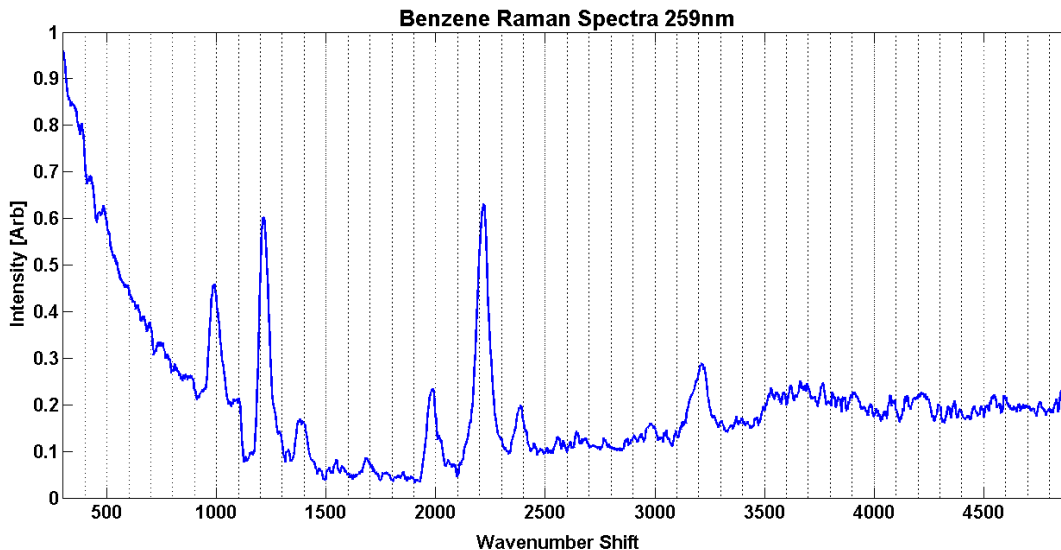


Figure 6.4. The full Raman spectrum of benzene using 259-nm (resonance) excitation

6.4 Normalization of Raman Data

In order to compare Raman data from different data runs, a few normalization factors are necessary. Power normalization is necessary because the Raman scattered signal is directly proportional to the incident power. The incident laser power was measured with each data set as the experiments were conducted to correct for its variations. Measurements of the power were recorded before and after each image were obtained. Raman scattering intensity is proportional to λ^{-4} , and each data set is corrected based upon the intensity and relative scattering cross-section associated with its excitation wavelength. Because of the wavelength dependence, if a molecule is excited at 500 nm and again at 250 nm, there should be an inherent signal gain of a factor of 16 at 250 nm. The additional resonant gain we seek is a separate effect, and the wavelength-dependent gain factor is removed prior to calculating the resonant gain. In the case of benzene and toluene, the resonance enhancement occurs in a very

small range, less than 1 nm; nevertheless the wavelength dependent correction is included for completeness.

The Spex Triplemate 1877 spectrometer has a variable throughput with typical overall efficiency values of 12–15% in the ultraviolet and approximately 4–6% in the visible (see Figure 5.12). To calculate the correction factor between the ultraviolet and the visible Raman scattered intensities, a simple ratio of throughput-efficiencies is used. The ratios are taken at wavelengths between 265 nm and 450 nm that correspond with the Raman scattered wavelengths for the benzene ν_2 mode when excited with 259 and 430 nm excitation, respectively.

Spex throughput Efficiency at 265 nm Raman Scattered light = 15%

Spex throughput Efficiency at 450 nm Raman Scattered light = 4%

$$\text{Raman Scattered Correction factor} = \frac{4\%}{15\%} = 0.27$$

In order for the UV Raman scattered data to be normalized to the visible data, it should be multiplied by a factor of 0.27.

The quantum efficiency variations in the EM-CCD camera must be considered throughout the ultraviolet region (200 nm – 380 nm), where the CCD maintains a relatively constant 35% quantum efficiency (see Figure 5.13). However; at 390nm, the quantum efficiency rises rapidly to a peak of 93% around 575 nm. It is necessary to correct the Raman scattered signal when comparing signals at the ultraviolet to the visible due to the variation in quantum efficiency. Therefore, the ultraviolet data must be corrected by a factor equal to the ratio of the quantum efficiencies when using 430 nm as the non-resonant visible comparison,

Quantum Efficiency for 200 – 380 nm = 35%

Quantum Efficiency at 450 nm excitation = 70%

$$\text{Raman Scattered Correction factor} = \frac{70\%}{35\%} = 2.0$$

Hence, it should be multiplied by a factor of 2.0 in order for the UV Raman scattered data to be normalized to the visible data.

The final normalization factor includes differences in exposure (i.e., integration) time of the EM-CCD camera. The exposure times for the Raman data ranged from 1 to 15 minutes, with most data (>90%) collected in either 1- or 2-minute exposure times. The correction for exposure time is a simple linear multiplication or division. The only exception from a linear correction is when the camera has become saturated by overexposure.

Analysis of the individual files, including the normalization correction and the noise removal are all performed using code developed in MATLAB, which is found in Appendix G.

6.5 Summary

In order to have an accurate measure of the Raman scattered intensities, it is necessary to remove any interfering noise. The resonance Raman scattering data may include a source of noise from saturated 'meteor' pixels as shown in Figure 6.1.

After this major source of noise is removed, it is possible to normalize the data. Four simple steps are performed in normalization:

- 1) a correction for laser power,
- 2) a correction for the λ^{-4} dependence of the Raman scattering,
- 3) a correction for the quantum efficiency of the EM-CCD camera,

4) a correction for the exposure (integration) time of the detector.

The final, and significantly more complicated, correction is that due to optical absorption in the sample, and that topic is discussed in Chapter 7, along with the resonance gain calculation.

Chapter 7: Raman Data Processing: Resonance Absorption Correction and Gain Calculation

The Raman spectra of a molecule at resonance may appear to be no stronger than the measurement using non-resonant excitation. It is necessary to correct for the absorption of the exciting wavelength and for self-absorption of the Raman scattered wavelength. The fact that resonance is found coincident with large absorption features, which also may correspond with Raman spectral lines, that experience self-absorption, is described in Chapter 8. The excitation wavelength may be absorbed so strongly that the laser beam does not fully penetrate the sample. As the laser beam propagates through the scattering medium, its intensity decreases as described by Beer's Law. The large amount of absorption at the resonance wavelength limits the scattering volume and the number of participating scatterers. If the scattered intensity is equivalent for both resonant and non-resonant excitation, and the volume of scattering is much smaller when on a resonance, then in the non-resonant case more molecules are proportionately scattering the measured intensity. The total scattered signal is the sum of the scattering intensity of each molecule, and the differences in this scattering intensity are important when determining the gain to use for the Raman scattering enhancement. When at resonance there may be significantly fewer molecules contributing to the overall Raman scattered intensity.

The retrieval of the resonance-enhanced Raman scattering gains for benzene and toluene are described in this chapter. Specifically, two key calculations must be made: first, a correction for the absorption is applied for the measurement on

resonance, and second, an accurate measure of the Raman scattered signal is found using a Gaussian fit to the average.

7.1 Absorption Correction for Resonance Raman Spectra

In order to correct the signals near the resonance condition it is necessary to accurately calculate the absorption along the path into and out of the scattering volume. The spectral resolution of the absorption must resolve the narrow bands to properly characterize a resonant enhancement. Absorption is calculated utilizing Beers Law,

$$I = I_0 e^{-\alpha z},$$

$$\text{Transmission} = \frac{I}{I_0} = e^{-\alpha z}$$

where α is the absorption coefficient in units of cm^{-1} . Thus, the intensity of the excitation laser falls exponentially as it propagates into the absorbing media. The absorption can also be described using the molar extinction coefficient, ϵ , with units of $(\text{Molarity} \times \text{cm})^{-1}$. By multiplying the molar absorptivity by the concentration of the solution, one finds the absorption coefficient. The benzene molecule exhibits four major ultraviolet absorption groups; one near 340 nm with a peak molar extinction $\epsilon \sim 0.004 \text{ M}^{-1} \text{ cm}^{-1}$, a second in the 260 nm range with an $\epsilon \sim 220 \text{ M}^{-1} \text{ cm}^{-1}$ (the focus of study in this dissertation), a third near 205 nm with an $\epsilon \sim 7000 \text{ M}^{-1} \text{ cm}^{-1}$, and finally a fourth in the vacuum ultraviolet near 160 nm with an $\epsilon \sim 60000 \text{ M}^{-1} \text{ cm}^{-1}$.

7.1.1 Absorption Correction for Benzene

The absorption correction for benzene has been calculated following two approaches that yield a resonance gain in the range of 10^3 to 10^4 relative to the normal Raman scattering signal intensity. The large range in values is caused by the differences in the absorption cross section of benzene between the vapor and liquid phases. The experiments were performed with liquid benzene, and the absorption calculations are first performed utilizing previously published values for the absorption of liquid benzene. However, it is clear that the resonance excitation peaks of liquid benzene are not found at the wavelengths corresponding to the maximum in absorption, but they correspond precisely with the locations of the vapor phase absorption peaks. This finding opens the question regarding the phase state in the sample during laser illumination, and the processes associated with forming of bubbles in the liquid during the dissolution of the liquid binding properties. A constant value is used for the number density calculations that correspond to the molecular density of the liquid-phase benzene. This approach is based on the fact that the experiments use liquid benzene, and although the molecules may be less ordered, there is not enough time for them to separate to form a lower density.

The liquid absorption spectra of benzene have been recorded and published [Friedel, 1951; Inagaki, 1971]. Benzene's large absorption cross section typically necessitates that it be diluted in a solvent such as cyclohexane. The dilution process allows a larger dynamic range in the measurement; however, solvents are known to cause shifts in the absorption spectra of the solute, as well as in a peak broadening [Berlman, 1971].

Because we find the difference between the locations of the liquid phase absorption maxima and the location of the resonance excitation peak, we compare the gains using the absorption cross section for both the liquid phase and the gas phase of benzene. Using the liquid- and vapor-phase absorption to calculate the resonance gain should bracket the upper and lower limits for the actual resonant gain.

7.1.1.1 Gas Phase Absorption Correction for Benzene

The vapor phase absorption spectrum for benzene was obtained from Hannelore Keller-Rudek, Geert K. Moortgat, *MPI-Mainz-UV-VIS Spectral Atlas of Gaseous Molecules* as published by Etzkorn *et al.* (1999). The absorption data from Etzkorn are plotted in Figure 7.1, and a small sample of the format of the data is shown in a numerical table in Appendix H. The absorption data are displayed in units of $\text{cm}^2/\text{molecule}$. For the absorption to be useful when in using Beer's Law, the values must be converted to an extinction coefficient, α (cm^{-1}), utilizing the density and the molecular weight of benzene. This process is shown below,

$$\begin{aligned}
 \text{Benzene } C_6H_6 \text{ Molecular weight} &\cong 78 \left(\frac{\text{g}}{\text{mol}} \right) \\
 \text{Liquid Benzene Density} &= 0.8786 \left(\frac{\text{g}}{\text{cm}^3} \right) \\
 78 \left(\frac{\text{g}}{\text{mol}} \right) \times \frac{1}{0.8786} \left(\frac{\text{cm}^3}{\text{g}} \right) \times \frac{1}{6.02 \times 10^{23}} \left(\frac{\text{mol}}{\text{molecules}} \right) &= 1.47 \times 10^{-22} \left(\frac{\text{cm}^3}{\text{molecule}} \right) \\
 \text{number Density} &= 6.78 \times 10^{21} \left(\frac{\text{molecules}}{\text{cm}^3} \right) \\
 \alpha \left(\frac{1}{\text{cm}} \right) &= \text{number Density} \left(\frac{\text{molecules}}{\text{cm}^3} \right) \times \text{absorption} \left(\frac{\text{cm}^2}{\text{molecule}} \right) \quad [7.1]
 \end{aligned}$$

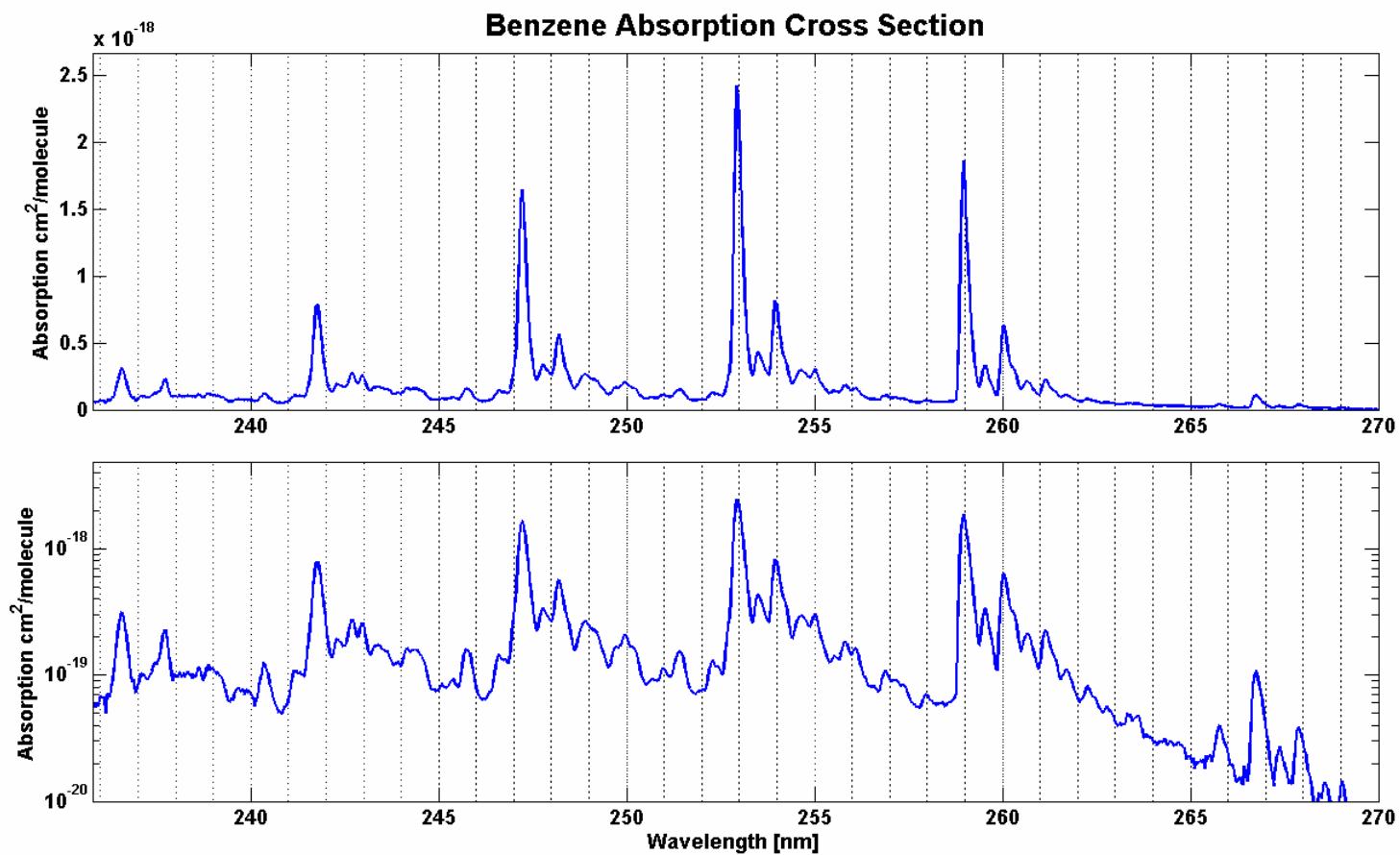


Figure 7.1. Benzene vapor phase absorption cross section, (top) linear scale and (bottom) log scale, Etzkorn[1999]

The absorption correction can be divided into two steps:

1. A correction for the absorption of the excitation wavelength, as it propagates into the scattering cell, is depicted in Figure 7.2.

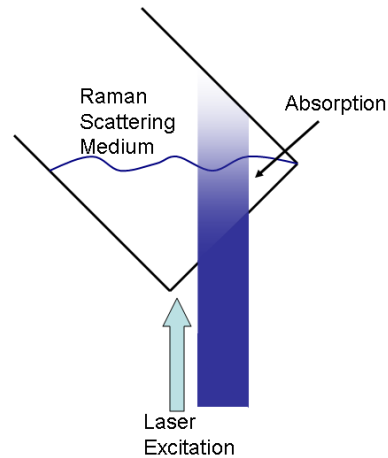


Figure 7.2. Absorption on the laser of excitation

2. A correction for the absorption of the Raman-shifted wavelength (i.e., self absorption) as it propagates and exits the scattering cell, is depicted in Figure 7.3.

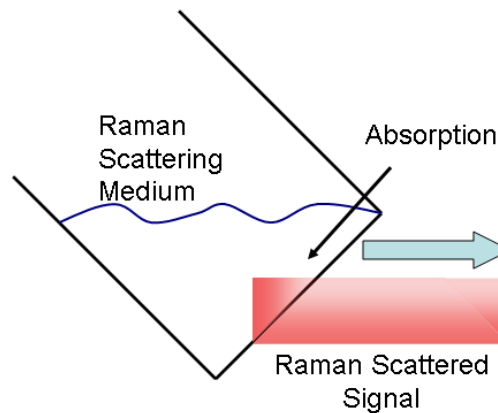


Figure 7.3. Absorption on the Raman scattered signal

The absorption corrections are performed utilizing a routine written in MATLAB, that requires inputs of the excitation wavelength and the wavenumber shift of the

associated Raman scattered signal. The wavelength of excitation was then used to find the absorption cross section from the published data. The retrieved absorption value was used in Equation [7.1] to find the corresponding absorption coefficient for the wavelength of excitation ($\alpha_{\text{excitation}}$). This calculation was performed a second time to find the self-absorption coefficient at the Raman scattered wavelength (α_{Raman}). The loss due to $\alpha_{\text{excitation}}$ is evaluated on the entry until the light is Raman scattered, and shifted to a new wavelength. Conversely, the α_{Raman} is only evaluated on the exit path at the Raman scatter wavelength. So, for any point in the scattering media there will be loss due to absorption both prior to scattering and after scattering. The total volume of the scattering region is then approximated. The volume of scattering is determined by the effective depth of penetration of the laser beam, and this volume is found by performing a weighted linear integral. One must calculate what the effective depth is by combining the losses for both the entry path to the scatterer and the exit path from the scatterer. A sketch shown in Figure 7.4 describes the method used for the calculation.

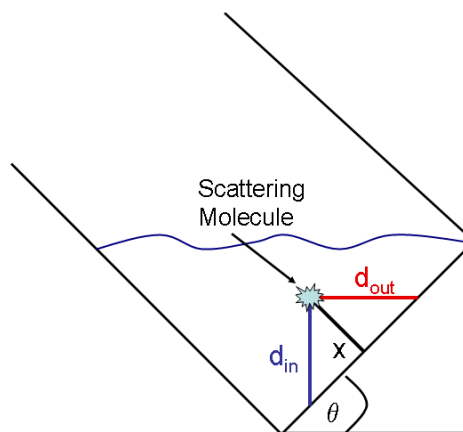


Figure 7.4. Absorption loss for a molecule at a distance of X from the laser entry point. d_{in} is the pathlength on entrance, d_{out} is the pathlength on exit, and θ is the angle of the sample holder

The loss on the entry path can be described as:

$$\frac{I}{I_0} = e^{-d_{in} \alpha_{excitation}},$$

where $d_{in} = \frac{X}{\cos(\theta)}$.

and the loss on the exit path can be described as:

$$\frac{I}{I_0} = e^{-d_{out} \alpha_{Raman}},$$

where $d_{out} = \frac{X}{\sin(\theta)}$.

The total loss over the distance X (the furthest point in) is integrated to find an effective penetration depth from which all scattering would take place.

$$\text{penetration depth} = \int_0^X e^{-\alpha_{excitation} \frac{x'}{\cos(\theta)}} e^{-\alpha_{Raman} \frac{x'}{\sin(\theta)}} dx'$$

$$\text{penetration depth} = - \left. \frac{e^{-x'(\alpha_{excitation} \sec(\theta) + \alpha_{Raman} \csc(\theta))} \cos(\theta) \sin(\theta)}{\alpha_{excitation} \sin(\theta) + \alpha_{Raman} \cos(\theta)} \right|_0^X$$

$$\text{for } x' = 0 \Rightarrow \frac{-\cos(\theta) \sin(\theta)}{\alpha_{excitation} \sin(\theta) + \alpha_{Raman} \cos(\theta)}$$

$$\text{for } x' = X \Rightarrow - \frac{e^{-X(\alpha_{excitation} \sec(\theta) + \alpha_{Raman} \csc(\theta))} \cos(\theta) \sin(\theta)}{\alpha_{excitation} \sin(\theta) + \alpha_{Raman} \cos(\theta)}$$

An example of the values for our absorption correction calculation in benzene follows:

$$\lambda_{\text{excitation}} = 259 \text{ nm}, \theta = 45^\circ, X = 1 \text{ cm}$$

$$\text{Wavenumber shift for Benzene Raman line} = 995 \text{ cm}^{-1}$$

$$\text{Raman Scattered wavelength for 259 nm excitation} = 265.85 \text{ nm}$$

$$\text{Number density of liquid Benzene} = 6.78 \times 10^{21} \frac{\text{molecules}}{\text{cm}^3}$$

$$\text{Absorption at 259 nm} \cong 1.72 \times 10^{-18} \frac{\text{cm}^2}{\text{molecule}}$$

$$\text{Absorption at 265.85 nm} \cong 3.49 \times 10^{-20} \frac{\text{cm}^2}{\text{molecule}}$$

From the absorption, we can then calculate the absorption coefficients for the wavelength of excitation and the Raman scattered wavelength.[†]

$$\alpha_{\text{excitation}} = 1.72 \times 10^{-18} \frac{\text{cm}^2}{\text{molecule}} \times 6.78 \times 10^{21} \frac{\text{molecules}}{\text{cm}^3}$$

$$\alpha_{\text{excitation}} = 11661 \frac{1}{\text{cm}}$$

$$\alpha_{\text{Raman}} = 3.49 \times 10^{-20} \frac{\text{cm}^2}{\text{molecule}} \times 6.78 \times 10^{21} \frac{\text{molecules}}{\text{cm}^3}$$

$$\alpha_{\text{Raman}} = 236 \frac{1}{\text{cm}}$$

At this point all, of the necessary quantities have been retrieved and the integral can be evaluated.

$$\text{Penetration Depth} = \left[-\frac{e^{-1(11611 \times \sec(45) + 236 \times \csc(45))} \cos(45) \sin(45)}{11661 \times \sin(45) + 236 \times \cos(45)} \right]$$

$$- \left[\frac{-\cos(45) \sin(45)}{11661 \sin(45) + 236 \cos(45)} \right]$$

$$= 5.94 \times 10^{-5} \text{ cm}$$

[†] The absorption of the laser wavelength is quite large when on resonance. This factor can be seen by comparing the $\alpha_{\text{excitation}}$ to the α_{Raman} . The α_{Raman} is comparatively small and contributes much less to the overall absorption.

The Raman scattered signal from resonance excitation in benzene is coming from the first thin $\sim 0.594 \mu\text{m}$ layer of the liquid. Thus, the laser energy does not penetrate very far into the sample because the absorption is so large, and this results in scattering occurring from a small fraction of the scattering volume compared with the visible (non-resonant) case. The absorption of benzene is negligible in the case of visible excitation; thus, one can assume that the entire path of the laser beam is participating in the Raman scattering. In our case, the scattering along total distance X is equivalent to the beam volume corresponding to a cylinder approximately 1 cm in diameter. This depth entire depth is involved in the scattering, and in the case of resonance at $\lambda_{\text{excitation}} = 259 \text{ nm}$, only the molecules in the first $\sim 0.594 \mu\text{m}$ participate in the scattering process. The gain in intensity of Raman scatter for the cases of resonant and off-resonant excitation can be found by taking the ratio of the penetration depths,[‡]

$$\text{Gain} = \frac{\text{penetration depth visible}}{\text{penetration depth resonance}} = \frac{1 \text{ cm}}{5.94 \times 10^{-5} \text{ cm}} = 16800$$

The resonance Raman scattered intensity results from a volume 16,800 times smaller than when the Raman spectra are generated with a visible wavelength. For equal intensity recorded spectra, the molecules on resonance have an intensity that is 1.7×10^4 larger than the non-resonant excitation.

The vapor phase absorption correction is applied to nine different excitation wavelengths near the absorption peak at 259 nm, where the resultant increase in the Raman spectra is evident. Figure 7.5 shows the relative intensity of the resonant

[‡] As was stated above, the cross sectional area of the beam is constant so that the total volume and, thus, the total number of scatterers are dependent solely on the penetration depth.

Raman spectra without the correction for absorption. Figure 7.6 shows the same Raman spectra with the absorption correction applied.

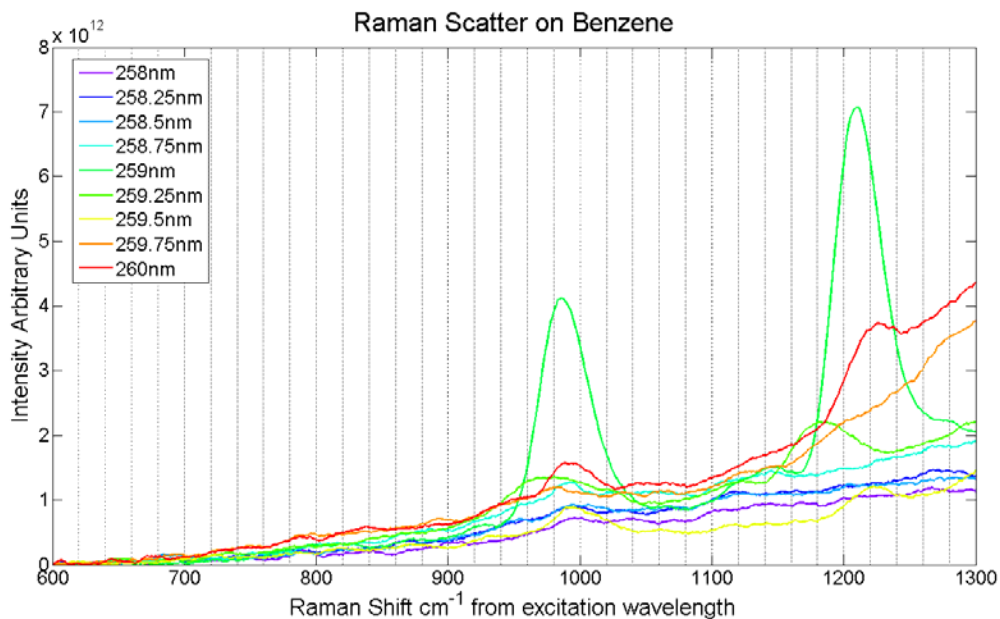


Figure 7.5. Benzene resonance-Raman spectra

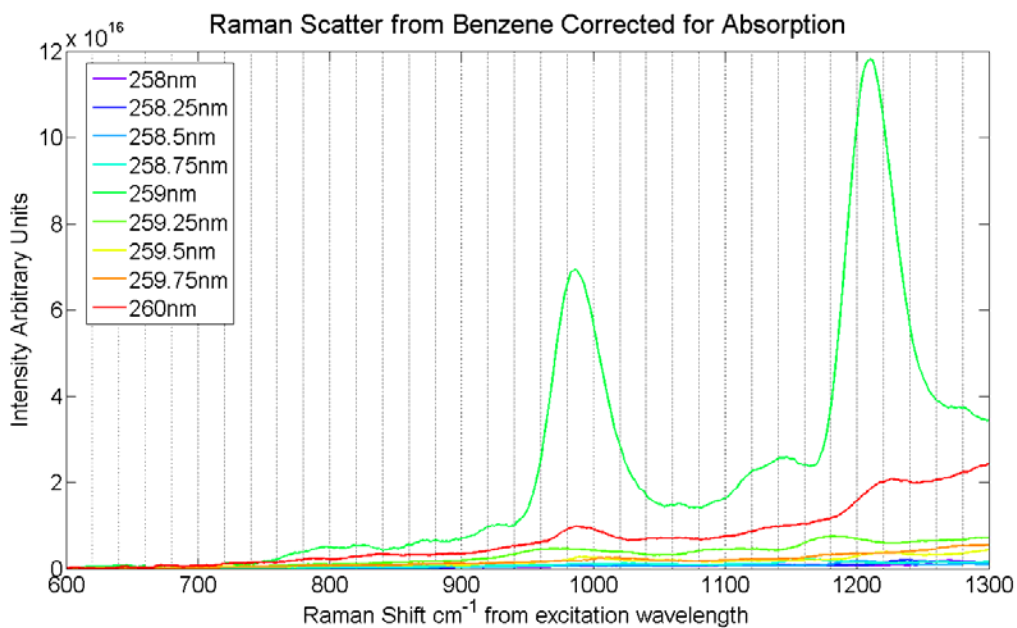


Figure 7.6. Resonance-Raman scatter as seen in Figure 7.5, with absorption correction

7.1.1.2 Liquid-Phase Absorption Correction for Benzene

The liquid-phase absorption spectrum for benzene is shown in Figure 7.7. The molar absorptivity ε values are significantly smaller for liquid-phase benzene than for gas-phase benzene. Because the absorption is smaller, one expects the scattering volume to be larger, because the light will penetrate deeper into the sample and excite more molecules. This increase in volume results in a smaller value for the overall gain factor.

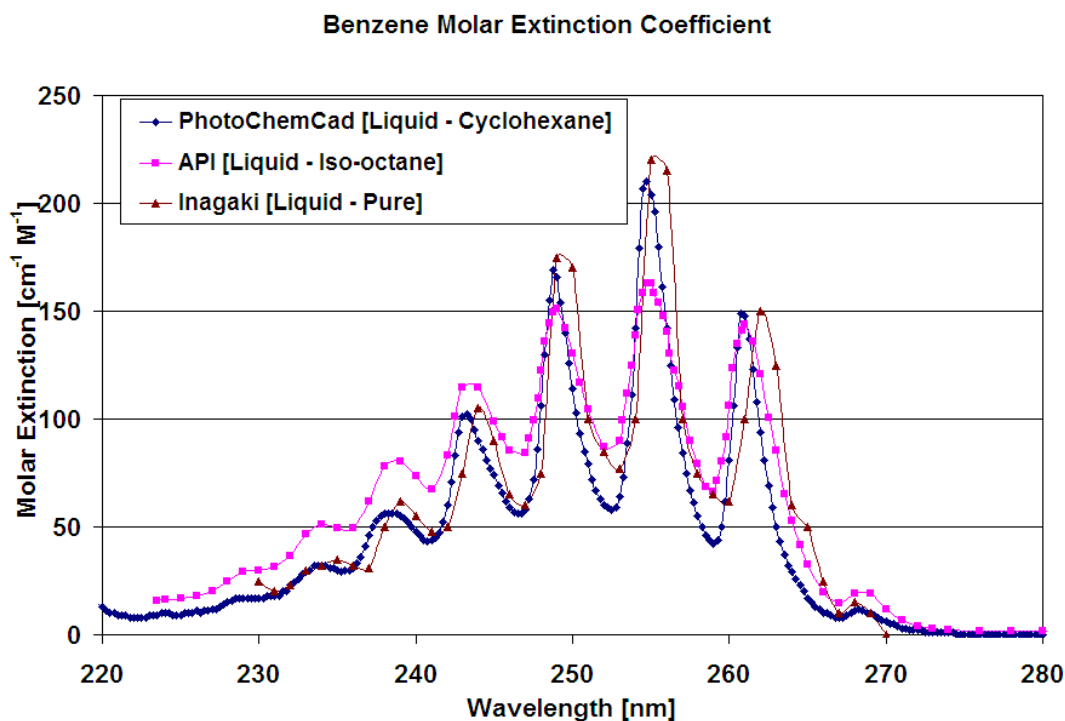


Figure 7.7. Liquid-phase benzene absorption [Du *et al.*, 1998, Inagaki 1972; API 1970]

By utilizing the molar absorptivity ε from Figure 7.5 for the excitation wavelength and the Raman scattered wavelength, a calculation of the values of $\alpha_{\text{excitation}}$ and α_{Raman} can be performed:

$$\alpha_{\text{excitation}} = \epsilon \times \text{Molarity Pure Benzene}$$

$$M_{\text{pure}} = 878.6 \frac{\text{g}}{\text{l}} \times \frac{1}{78} \frac{\text{mol}}{\text{g}} = 11.26 \frac{\text{mol}}{\text{l}}$$

$$\epsilon \text{ at } 259 \text{ nm} = 65 \frac{1}{\text{M} \cdot \text{cm}}$$

$$\alpha_{\text{excitation}} = 65 \frac{1}{\text{M} \cdot \text{cm}} \times 11.26$$

$$\alpha_{\text{excitation}} = 731.9 \frac{1}{\text{cm}}$$

$$\epsilon \text{ at } 265 \text{ nm} = 25 \frac{1}{\text{M} \cdot \text{cm}}$$

$$\alpha_{\text{Raman}} = 25 \frac{1}{\text{M} \cdot \text{cm}} \times 11.26$$

$$\alpha_{\text{Raman}} = 281.5 \frac{1}{\text{cm}}$$

The effective penetration depth can be calculated similarly to that shown in section 7.1.1.1, the yielding,

$$\begin{aligned} \text{Penetration Depth} &= \left[-\frac{e^{-1(731.9 \times \sec(45) + 281.5 \times \csc(45))} \cos(45) \sin(45)}{731.9 \times \sin(45) + 281.5 \times \cos(45)} \right] \\ &\quad - \left[\frac{-\cos(45) \sin(45)}{731.9 \sin(45) + 281.5 \cos(45)} \right] \\ &= 6.97 \times 10^{-4} \text{ cm} \end{aligned}$$

$$\text{Gain} = \frac{\text{penetration depth visible}}{\text{penetration depth resonance}} = \frac{1}{6.97 \times 10^{-4}} \frac{\text{cm}}{\text{cm}} = 1400$$

The Raman scattered intensity when on resonance results from a volume 1400 times smaller than in the visible for the case when liquid benzene absorption is considered.

The molecules on resonance have an effective scattering cross section that is 1400 times larger than the non-resonant excitation.

7.1.2 Absorption Correction for Toluene

The entire procedure in Section 7.2.1 can be repeated to calculate the absorption correction and the resonance gain in toluene. The calculation is identical with a few simple changes:

- (1) the wavelength of excitation that was used for resonance Raman studies in toluene is 266.83 nm,
- (2) the absorption spectra of liquid and vapor states are used, and,
- (3) the input molarity was calculated for pure toluene.

The corrections were also performed twice: once for gas phase absorption, and a second time for liquid-phase absorption. Again, we find the difference in the location of the resonant excitation at the vapor-phase peak rather than the liquid-phase absorption peak.

7.1.2.1 Gas Phase Absorption Correction for Toluene

The vapor phase absorption spectra for toluene are shown in Figure 7.8 [Etzkorn *et al.*, (1999)]. A numerical table containing a small sample of the absorption spectrum of toluene is provided in Appendix I.

In the case of toluene we use the following values for our absorption correction calculation,

$$\lambda_{\text{excitation}} = 266.83 \text{ nm}, \theta = 45^{\circ}, X = 1 \text{ cm}$$

wavenumber shift for toluene Raman line = 800 cm^{-1}
 from 800 cm^{-1} , Raman scattered wavelength = 272.65 nm

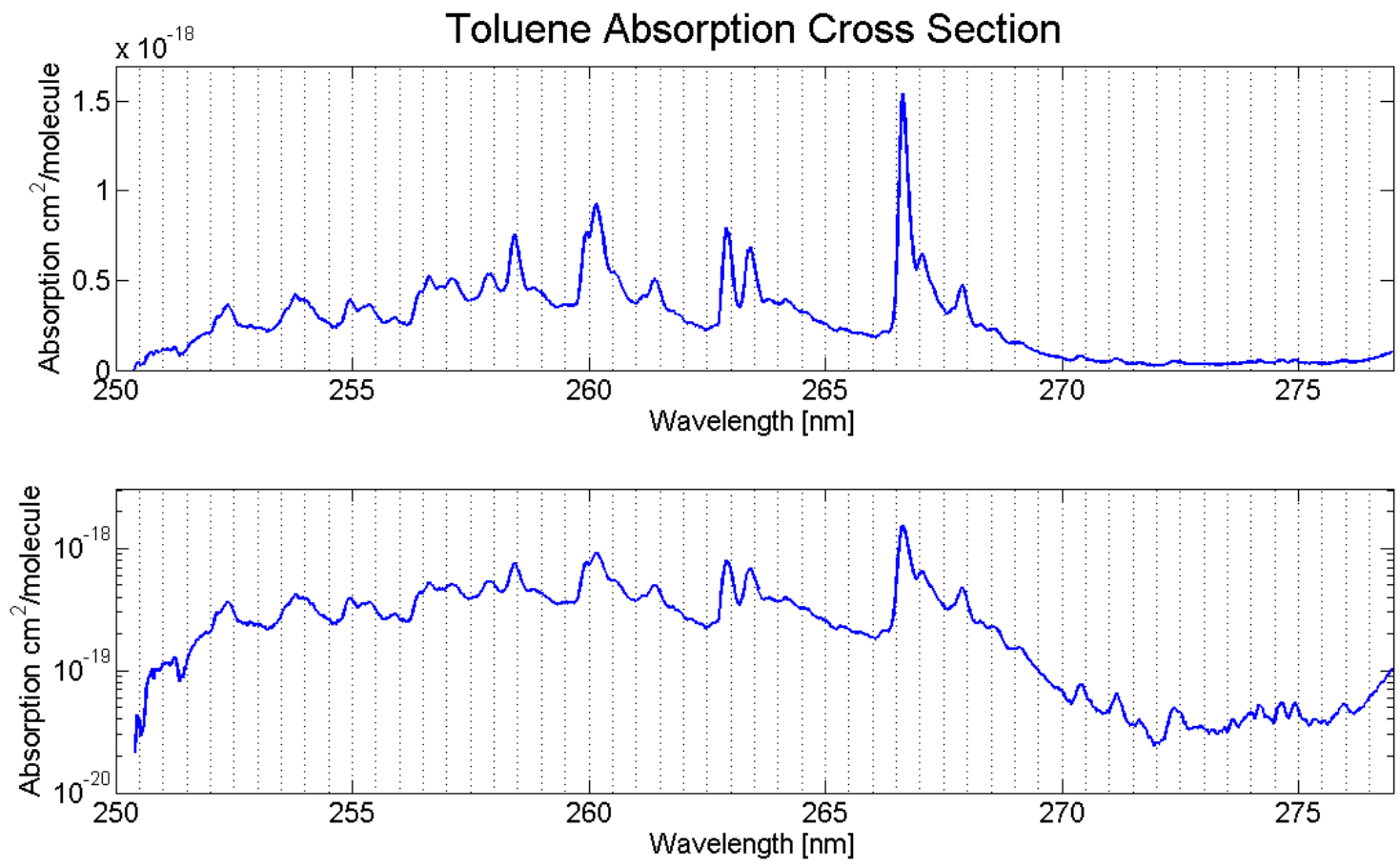


Figure 7.8. Toluene vapor-phase absorption cross section [Etzkorn, 1999]

$$\text{number density of liquid toluene} = 5.67 \times 10^{21} \frac{\text{molecules}}{\text{cm}^3}$$

$$\text{Absorption at } 266.83 \text{ nm} \cong 7.22 \times 10^{-19} \frac{\text{cm}^2}{\text{molecule}}$$

$$\text{Absorption at } 272.65 \text{ nm} \cong 3.31 \times 10^{-20} \frac{\text{cm}^2}{\text{molecule}}$$

From the absorption, we can then calculate the absorption coefficients for the excitation wavelength and the Raman scattered wavelength.

$$\alpha_{\text{excitation}} = 7.72 \times 10^{-19} \frac{\text{cm}^2}{\text{molecule}} \times 5.67 \times 10^{21} \frac{\text{molecules}}{\text{cm}^3}$$

$$\alpha_{\text{excitation}} = 4377 \frac{1}{\text{cm}}$$

$$\alpha_{\text{Raman}} = 3.31 \times 10^{-20} \frac{\text{cm}^2}{\text{molecule}} \times 5.67 \times 10^{21} \frac{\text{molecules}}{\text{cm}^3}$$

$$\alpha_{\text{Raman}} = 187 \frac{1}{\text{cm}}$$

$$\text{Penetration Depth} = \left[-\frac{e^{-1(4377 \times \sec(45) + 236 \times \csc(45))} \cos(45) \sin(45)}{4377 \times \sin(45) + 187 \times \cos(45)} \right] - \left[\frac{-\cos(45) \sin(45)}{5377 \sin(45) + 187 \cos(45)} \right]$$

$$= 1.65 \times 10^{-4} \text{ cm}$$

As in the case of benzene, the gain is calculated as the ratio of the penetration depths at visible to the ultraviolet wavelengths,

$$\text{Gain} = \frac{\text{penetration Depth visible}}{\text{penetration Depth Resonance}} = \frac{1}{1.65 \times 10^{-4}} \frac{\text{cm}}{\text{cm}} = 6060$$

The Raman scattered intensity on resonance results from a volume 6060 times smaller than in the visible case. For equal intensity recorded spectra the molecules on resonance have an effective scattering cross section that is 6060 times larger than the non-resonant excitation. The absorption correction, gain calculation, and path

integration were all performed in MATLAB (the associated code is provided in Appendix J).

7.1.2.2 Liquid Phase Absorption Correction for Toluene

Using the process described in section 7.1.1.2 (vapor-phase benzene correction), the liquid absorption correction for toluene has been calculated. By using the molar absorptivity ϵ from Figure 7.9 at the excitation wavelength and the Raman scattered wavelength, a calculation of the values of $\alpha_{\text{excitation}}$ and α_{Raman} can be performed.

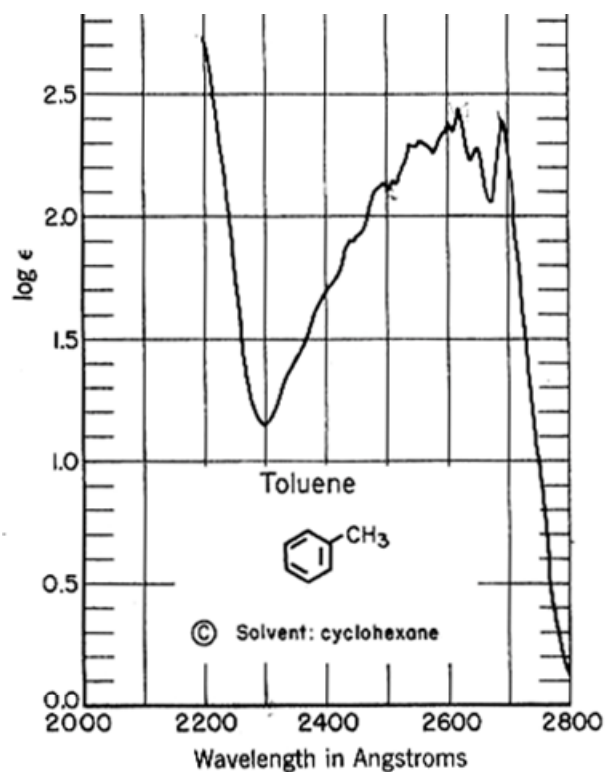


Figure 7.9. Liquid toluene absorption in cyclohexane [Friedel *et al.*, 1951]

$$\alpha_{\text{excitation}} = \epsilon \times \text{Molarity Pure Toluene}$$

$$M_{\text{pure}} = 866.9 \frac{\text{g}}{\text{l}} \times \frac{1}{92} \frac{\text{mol}}{\text{g}} = 9.42 \frac{\text{mol}}{\text{l}}$$

$$\varepsilon \text{ at } 266.83 \text{ nm} = 250 \frac{1}{\text{M} \cdot \text{cm}}$$

$$\alpha_{\text{excitation}} = 250 \frac{1}{\text{M} \cdot \text{cm}} \times 9.42$$

$$\alpha_{\text{excitation}} = 2355 \frac{1}{\text{cm}}$$

$$\varepsilon \text{ at } 272.65 \text{ nm} = 50 \frac{1}{\text{M} \cdot \text{cm}}$$

$$\alpha_{\text{Raman}} = 50 \frac{1}{\text{M} \cdot \text{cm}} \times 9.42$$

$$\alpha_{\text{Raman}} = 471 \frac{1}{\text{cm}}$$

Similarly to section 7.2.2.1, the effective penetration depth can be calculated.

$$\begin{aligned} \text{Penetration Depth} &= \left[-\frac{e^{-1(2355 \times \sec(45) + 471 \times \csc(45))} \cos(45) \sin(45)}{2355 \times \sin(45) + 471 \times \cos(45)} \right] \\ &\quad - \left[\frac{-\cos(45) \sin(45)}{2355 \sin(45) + 471 \cos(45)} \right] \\ &= 2.5 \times 10^{-4} \text{ cm} \end{aligned}$$

$$\text{Gain} = \frac{\text{penetration Depth visible}}{\text{penetration Depth Resonance}} = \frac{1}{2.5 \times 10^{-4}} \frac{\text{cm}}{\text{cm}} = 4000$$

The Raman scattered intensity when on resonance results from a volume 4000 times smaller than in the visible case. For equal intensity recorded spectra the molecules on resonance have an effective scattering cross section that is 4000 times larger than the non-resonant excitation.

It is rare that the Raman scattered lines to have identical intensities. In order to find the total gain, it is necessary to calculate the intensity of the Raman lines, and this measure of intensity is performed using a Gaussian fit to find the area under the curve.

7.2 Peak Fitting

In order to compare the strength of the Raman scattered signals, two methods were employed; first Raman lines are fitted to the peak using a known distribution, such as a Gaussian curve; second a direct retrieval of the Raman parameters is obtained from integration of the area under the peaks in the spectrum. Using these methods, it is possible to retrieve a peak intensity and calculate the intensity by performing a numerical integration of the area under the Raman lines. Comparing the area underneath each of the fitted peaks allows comparison of the Raman lines on an equal footing.

The Gaussian peak fitting was performed using Fityk, which is an open source peak-fitting software that has been used in a variety of applications from spectroscopy to crystallography. Fityk is a powerful program that can remove background levels using a multi-point spline, and also maintains a large array of distribution types that can be used for peak fitting curves, such as Gaussian, Lorentzian, Voigt, and many others. The original data for 258.88 nm excitation of benzene are shown in a screenshot from Fityk in Figure 7.10. A fit to the Raman scattered lines of the retrieved data was performed using a normal (Gaussian) distribution,

$$y = \frac{P}{\sigma\sqrt{2\pi}} e^{-\frac{1}{2\sigma^2}(x-\mu)^2}.$$

where P is the Peak height, σ is the standard deviation, and μ is the center of the distribution.

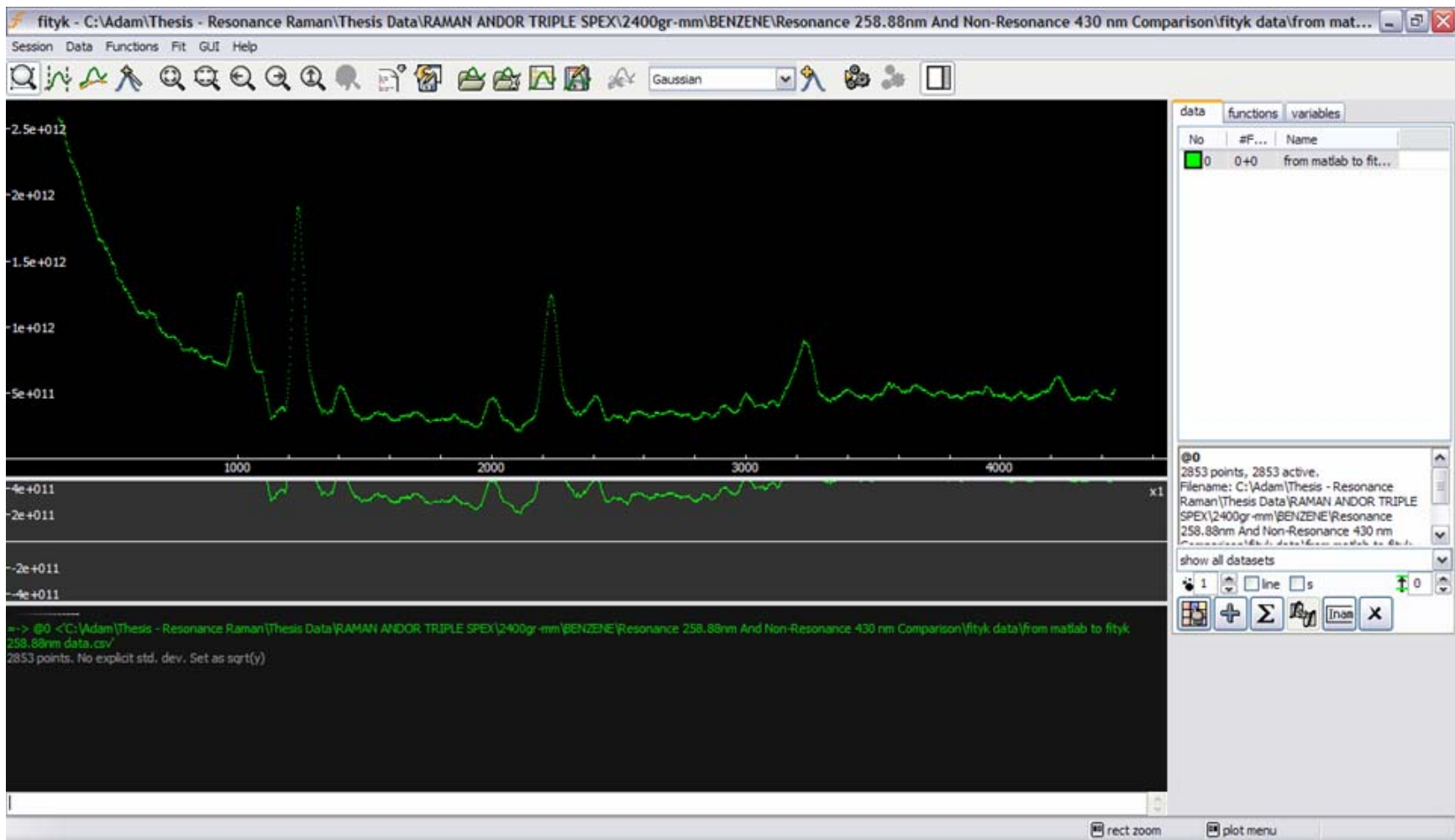


Figure 7.10 Fityk screenshot with resonance Raman spectrum of benzene using 258.88 nm excitation

The program also employs three different weighted least-squares methods for retrieval of the properly fitted peaks. The method selected for analysis of the Raman peaks is the built-in Levenberg–Marquardt technique, which works by minimizing the sum of the squares of the deviations,

$$S(q) = \sum_{i=1}^n [y_i - f(t_i|p)]^2 .$$

There are three basic steps involved in peak fitting the Raman data using the Fityk package. First, it is necessary to strip any background signals that exists in the data. This background may be due to noise counts, or it could be a result of the Rayleigh tail extending into and interfering with the Raman data. The Rayleigh tail is clearly seen in Figure 7.10, where the intensity drops in an exponential manner with increased wavenumber over the low wavenumber ($< 1000 \text{ cm}^{-1}$) region. After the background has been properly stripped using a multipoint spline (Figure 7.11), it is then necessary to determine how many Raman peaks exist in the data. For each Raman peak, a rough guess fit is entered using the GUI . There are two ways to enter the rough guess: either by using the auto-add-peak function or by performing a simple mouse click that will determine the center and peak value of the Gaussian curve, then by holding and dragging the mouse the width parameter entered (Figure 7.12).

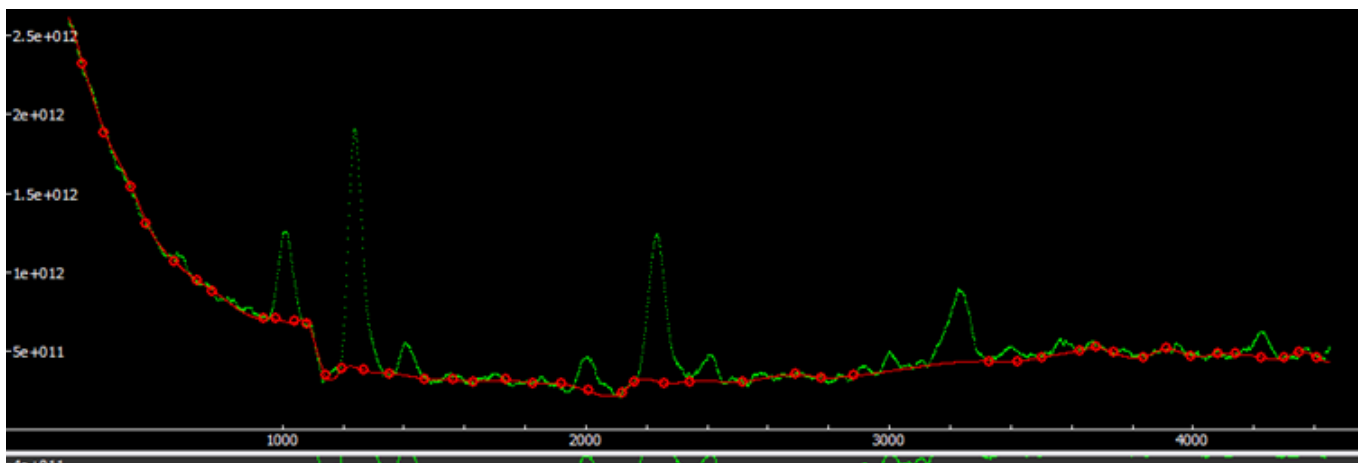


Figure 7.11. Fityk multi-point spline background removal for 258.88 nm excitation

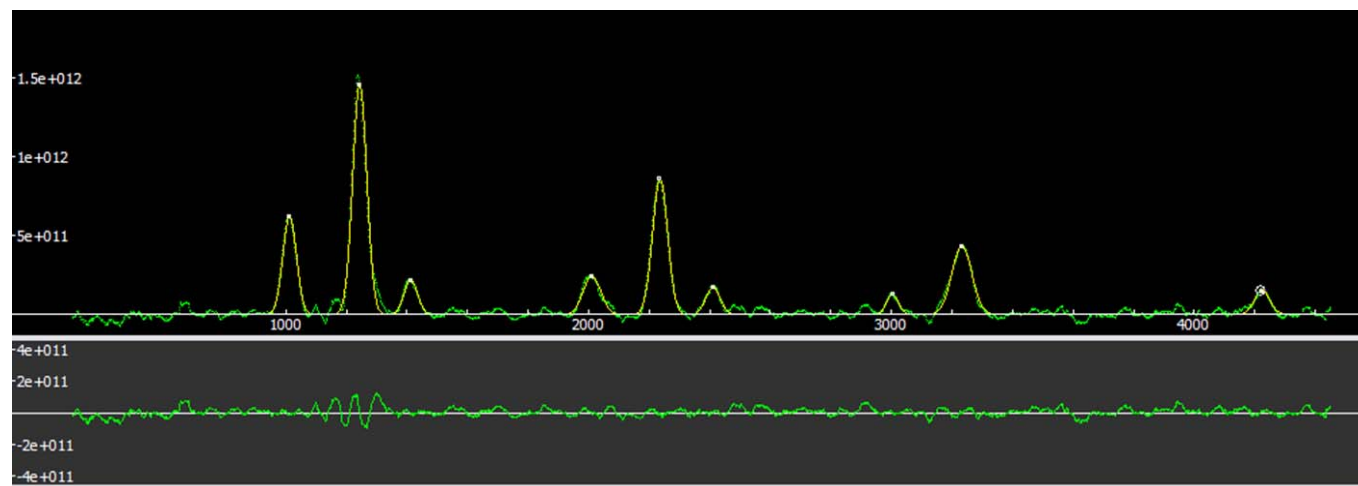


Figure 7.12. Fityk background removal and peak fits for 258.88 nm excitation

This task is repeated for each of the peaks. Figure 7.12 shows another screenshot with the background removed and the fitted peaks for the 258.88 nm resonance-Raman spectrum in benzene. Finally, the program seeks a best fit when the sum of the least squares is minimized. One should note that if the original guesses are too poor, the program will not converge. The retrieved fits using Fityk were exported to a text file and then imported to MATLAB for ease of manipulation and calculations. Figure 7.13 shows the Gaussian fits for the Raman data of the 258.88 nm (resonance) excitation wavelength in benzene.

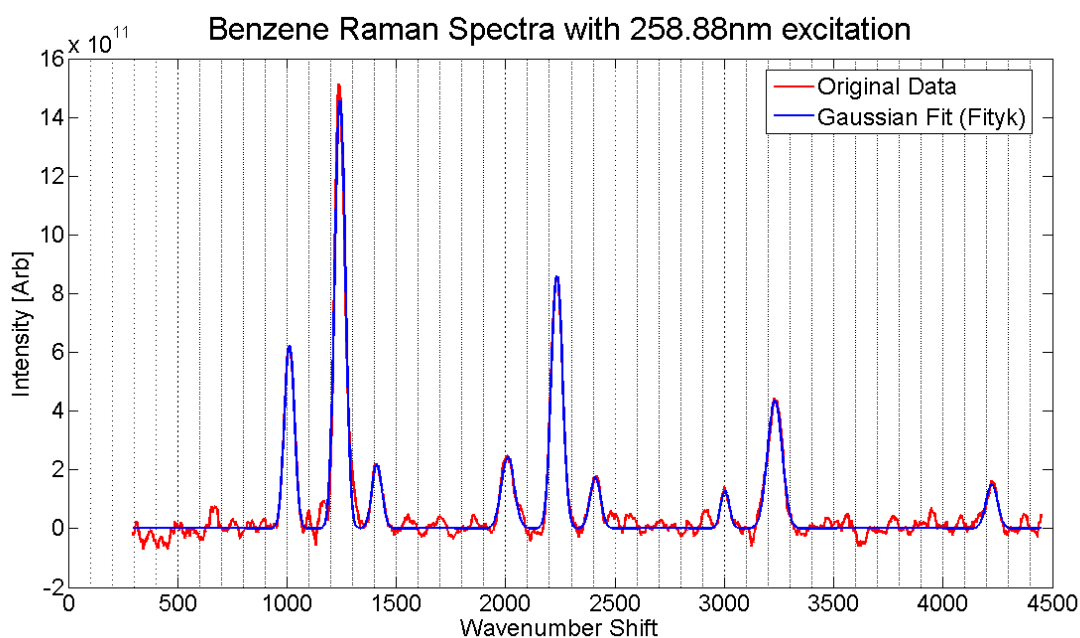


Figure 7.13. Gaussian fit to 258.88 nm (resonance) Raman data using Fityk

The fitted Gaussian peaks were then used to calculate the areas and the peak heights for each of the Raman lines; this calculation is the final correction that is necessary in order to compare the Raman scattered intensities. Table 7.1 shows the peak center, relative peak height, full-width at half maximum, and area under the peaks retrieved by the Fityk calculation for the data shown in Figure 7.13.

Table 7.1. Raman peak parameters from Fityk for peaks shown in Figure 7.13.

Peak Center cm⁻¹	Peak Height arb	FWHM cm⁻¹	Area arb
1010.69 ± 20	6.02E+11 ± 3.01E+10	50.962	3.27E+13 ± 1.64E+12
1242.53 ± 20	1.49E+12 ± 7.45E+10	53.1084	8.40E+13 ± 4.20E+12
1413.59 ± 25	1.90E+11 ± 9.50E+9	44.4208	8.97E+12 ± 4.49E+11
2006.32 ± 24	2.51E+11 ± 1.26E+10	64.2524	1.72E+13 ± 8.60E+11
2235.06 ± 25	9.07E+11 ± 4.04E+10	65.979	6.37E+13 ± 3.19E+12
2400.61 ± 24	1.65E+11 ± 8.30E+9	65.5846	1.15E+13 ± 5.85E+11
3002.62 ± 27	1.05E+11 ± 5.25E+9	33.8142	3.79E+12 ± 1.90E+11
3226.52 ± 26	4.18E+11 ± 2.09E+10	79.978	3.55E+13 ± 1.78E+12
4230.53 ± 30	1.45E+11 ± 7.25E+9	52.2156	8.06E+12 ± 4.03E+11

A routine that was developed in MATLAB and used in conjunction with Fityk finds the Raman lines and their associated parameters. The peaks of the Raman lines were found and the associated wavenumbers were used for the Raman line locations. After finding the peak, the full-width at half-maximum was retrieved. The half-maximum point was found by walking down the sides of each peak to locate the first point with intensity less than half of the maximum. The walk method was performed for both the lower and upper limit, thus retrieving the full-width at half-maximum. Finally, a numerical integration of the area defined by the full-width at half-maximum was calculated.

The Raman lines excited by the 258.88 nm wavelength along with their respective full-width at half-maximum (red) from the Matlab routine are shown in Figure 7.14 and the associated parameters are listed in Table 7.2.

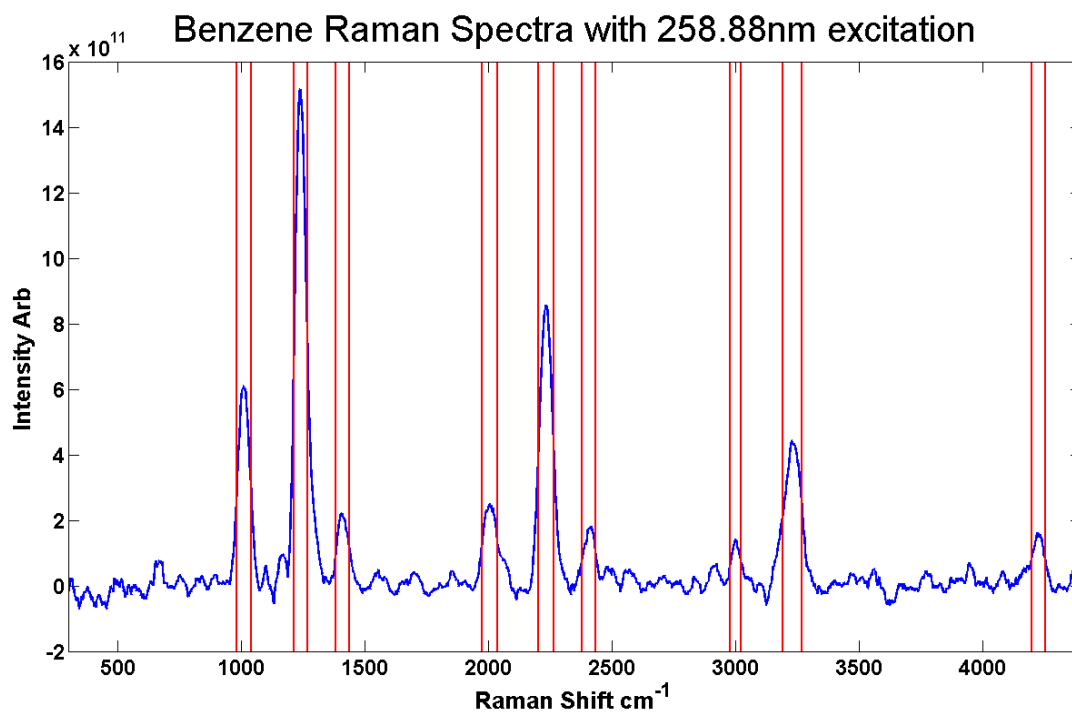


Figure 7.14. Raman scatter from 258.88 nm (blue) with full-width at half maximum (red) from original data for each Raman line

Table 7.2. Raman peak parameters from Matlab for peaks shown in Figure 7.14.

Peak Center cm^{-1}	Peak Height arb	FWHM cm^{-1}	Area arb
1012.8 ± 12	$6.11\text{E}+11 \pm 3.06\text{E}+10$	56.74	$2.77\text{E}+13 \pm 1.39\text{E}+12$
1237.9 ± 11	$1.51\text{E}+12 \pm 7.55\text{E}+10$	52.9	$6.40\text{E}+13 \pm 3.20\text{E}+12$
1407.3 ± 15	$2.20\text{E}+11 \pm 1.10\text{E}+11$	56	$9.74\text{E}+12 \pm 4.87\text{E}+11$
2005.5 ± 16	$2.48\text{E}+11 \pm 1.24\text{E}+10$	62.7	$1.29\text{E}+13 \pm 6.45\text{E}+11$
2234 ± 14	$8.55\text{E}+11 \pm 4.28\text{E}+10$	61.9	$4.20\text{E}+13 \pm 2.10\text{E}+12$
2417.3 ± 12	$1.81\text{E}+11 \pm 9.05\text{E}+9$	54	$7.76\text{E}+12 \pm 3.88\text{E}+11$
3001.3 ± 14	$1.40\text{E}+11 \pm 7.00\text{E}+9$	44.3	$4.71\text{E}+12 \pm 2.36\text{E}+11$
3227 ± 12	$4.43\text{E}+11 \pm 2.22\text{E}+10$	76.7	$2.71\text{E}+13 \pm 1.36\text{E}+12$
4222 ± 17	$1.62\text{E}+11 \pm 8.01\text{E}+9$	55.3	$7.03\text{E}+12 \pm 3.52\text{E}+11$

Both the Fityk routine and the MATLAB routine were repeated using the non-resonant (430 nm) data. The Raman lines from the 430 nm excitation using Fityk can be seen in Figure 7.15, and their associated parameters are listed in Table 7.3.

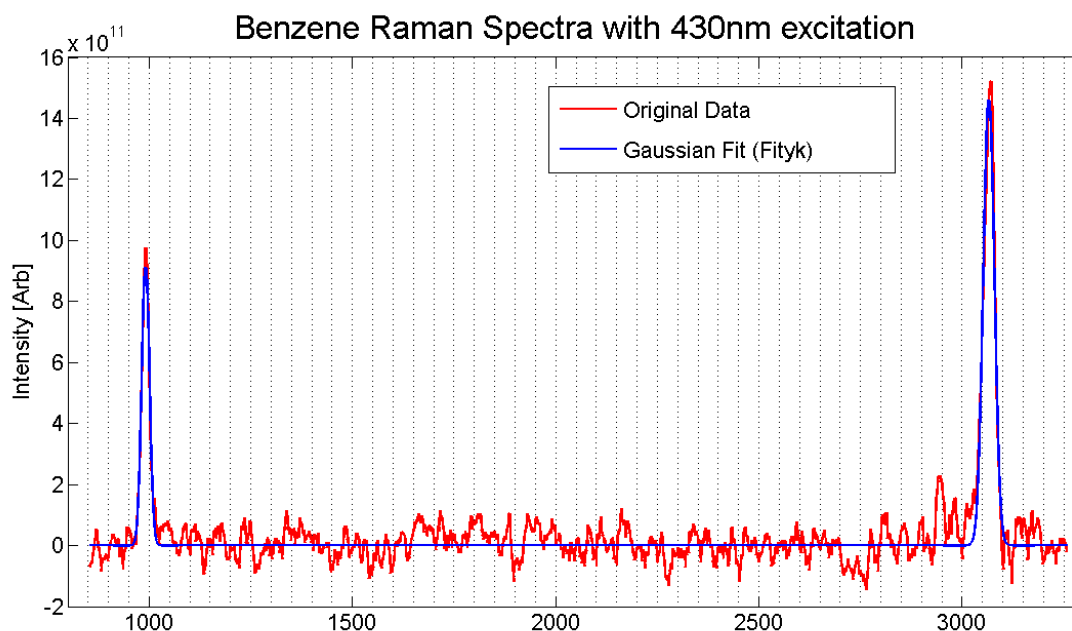


Figure 7.15. Gaussian fit to 430 nm (non-resonant) Raman data using Fityk

Table 7.3. Raman peak parameters from Fityk for peaks shown in Figure 7.15

Peak Center cm^{-1}	Peak Height arb	FWHM cm^{-1}	Area arb
991.275 ± 7	$9.13\text{E}+11 \pm 4.57\text{E}+10$	21.7616	$2.11\text{E}+13 \pm 1.06\text{E}+12$
3065.55 ± 7	$1.46\text{E}+12 \pm 7.30\text{E}+10$	31.1172	$4.83\text{E}+13 \pm 2.44\text{E}+12$

The Raman lines from the 430 nm excitation along with their respective full-width at half-maximum (red) from the MATLAB routine can be seen in Figure 7.16, and the associated parameters are listed in Table 7.4.

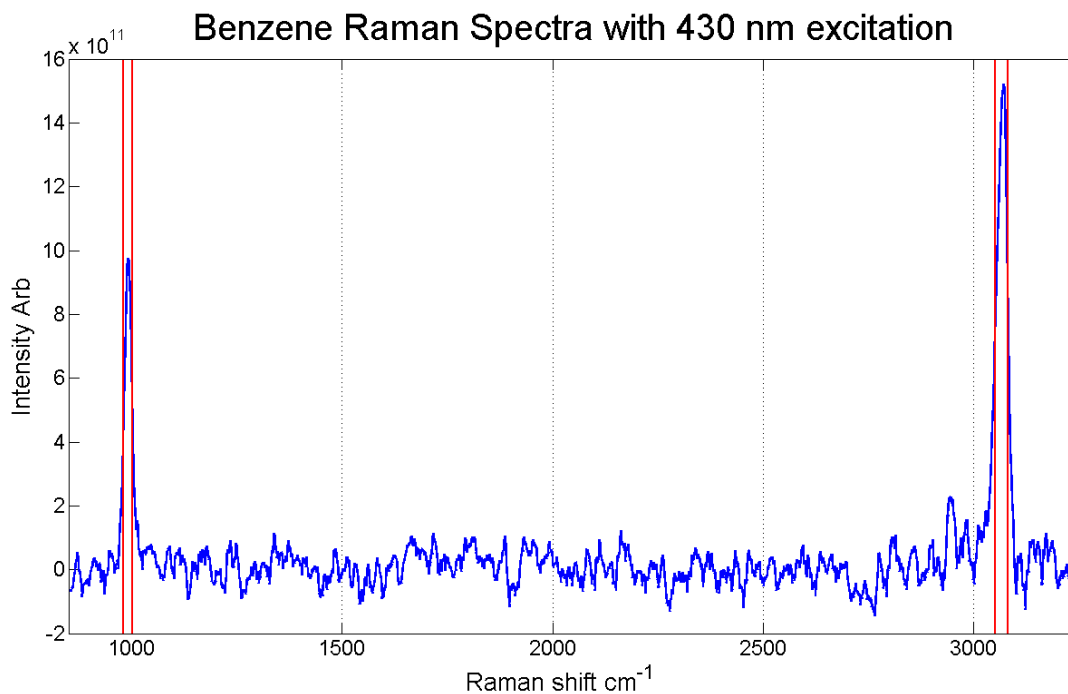


Figure 7.16. Raman scatter from 430 nm (blue) with full-width at half maximum (red) from original data

Table 7.4 Raman peak parameters from Matlab for peaks shown in Figure 7.16

Peak Center cm^{-1}	Peak Height arb	FWHM cm^{-1}	Area arb
991.97 ± 7	$9.76\text{E}+11 \pm 4.88\text{E}+10$	20.42	$1.56\text{E}+13 \pm 7.80\text{E}+11$
3070.9 ± 7	$1.52\text{E}+12 \pm 7.60\text{E}+10$	30.9	$3.70\text{E}+13 \pm 1.85\text{E}+12$

7.3 Benzene Resonance-Raman Final Gain Figure

The overall resonant enhancement can be calculated utilizing the absorption gain correction value from Section 7.2.1 and combining it with the ratio of the areas of the 992 cm^{-1} Raman line for resonant and non-resonant excitation. The ν_2 , 992 cm^{-1} Raman scattered line is the only line for which a gain can be calculated, as it is the only line that is present in both the non-resonant and resonant spectra. The

combination of the absorption correction from the volume of scattering and the relative measure of the intensity of the Raman scattering, area under the curve, yields

Absorption Correction = 16800

$$\text{Gaussian fitted area ratio} = \frac{258.88 \text{ nm}}{430 \text{ nm}} = \frac{1.56 \times 10^{13} \pm 7.80 \times 10^{11}}{2.11 \times 10^{13} \pm 1.06 \times 10^{12}} \cong 0.74 \pm 0.08$$

$$\text{Matlab retrieved area ratio} = \frac{258.88 \text{ nm}}{430 \text{ nm}} = \frac{2.77 \times 10^{13} \pm 1.39 \times 10^{12}}{3.27 \times 10^{13} \pm 1.64 \times 10^{12}} \cong 0.85 \pm 0.09$$

Overall Resonant Gain Gas Phase Calculation $\cong 16800 \times 0.85 \pm 0.09 \cong 14300 \pm 1500$

Overall Resonant Gain Liquid Phase Calculation $\cong 1400 \times 0.85 \pm 0.09 \cong 1200 \pm 120$

The resonant gain for the ν_2 (ring-stretch) mode of vibration is found to be approximately 3 to 4 orders of magnitude larger than normal Raman.

7.4 Summary

The absorption correction for the resonance-Raman scatter from benzene and toluene has been performed. Specifically, two calculations were made: first a correction for the absorption that determined the scattering volume, second, an accurate measure of the Raman-scattered signals was obtained for both a Gaussian fit and a direct numerical integration employed to retrieve the Raman scattered intensity from the area. The absorption correction on resonance is a result of the decrease in the effective scattering volume and it, therefore, decreases the total number of molecules that participate in the scattering process. The combination of these corrections yields a final value for the overall resonance enhancement of 14300 ± 1500 for gas phase benzene and 1200 ± 120 for the liquid phase calculation. A gain for the ν_2 vibrational mode of benzene was thus found to be 3 to 4 orders of

magnitude larger than normal Raman scattering. Finally, because the ν_2 mode is the only fundamentally enhanced mode at resonance, it is not possible to make a calculation of gain for any of the other modes.

Chapter 8: Resonance-Raman Spectra

Benzene has been extensively studied since it was first isolated in 1925 by Michael Faraday [Faraday, 1825]. Some years later in 1865, benzene's structure was described by Kekulé as an alternating double- and single-bond structure denoted as the benzene ring [Kekulé, 1865]. The symmetries of the benzene molecule have been debated and discussed for many years. Many studies have shown a resonance enhancement of the benzene Raman signal [Korenowski, 1978; Asher and Johnson, 1984; Asher, 1988, 1993; Ziegler & Hudson, 1980; Gerrity *et al.* 1985; Sension *et al.*, 1990, 1991], although these previous investigations lacked the fine tuning of the excitation wavelength that we use in this study.

Ziegler and Hudson [1980] made measurements of the resonance enhancement of liquid benzene by using 212.8 nm in order to probe the singlet (${}^1B_{1u}$) transition. The spectra obtained by Ziegler and Hudson is believed to be the first resonance enhanced Raman spectrum of benzene and shows that the only enhanced mode is the fundamental ν_2 992 cm^{-1} . Asher and Johnson [1984] performed measurements of the resonance enhancement of benzene by using an excitation source stepped through the absorption of liquid benzene, using approximately 2 nm steps. They measured and recorded the 992 cm^{-1} peak, relative to the acetonitrile peak at 918 cm^{-1} . Gerrity *et al.*, [1985] probed benzene vapor in the deep ultraviolet confirming the ν_2 (992 cm^{-1}) enhancement, as well as the e_{2g} combinational modes and overtones. Sension *et al.* [1991] recorded resonance enhanced Raman spectra of

benzene in the ${}^1B_{1u}$ region. The recorded spectra also show the enhancement of the e_{2g} modes of vibration and the only fundamentally enhanced mode is ν_2 .

Each of the resonance Raman spectra previously published and the results presented in this chapter show enhancement of the e_{2g} modes and the conspicuous lack of the ν_1 C-H stretching mode of benzene. The ν_1 mode when excited in the non-resonant Raman scattering regime is generally 1.5 times larger than the ν_2 mode at 992 cm^{-1} . The $2\nu_8$ result seen by Gerrity *et al.* is also confirmed in this study with a large enhancement when the wavelength of excitation matches the vapor phase absorption peak ($\sim 259\text{ nm}$).

The Raman data are collected both at resonance and off-resonance, in order to determine the resonance gain by comparisons with off-resonance Raman spectra. The excitation at resonance increases the relative signal strengths and excites additional modes in the spectrum (combinational and overtones). These modes have been compared with those found in the previous work of Ziegler and Hudson [1981], who performed resonance measurements on benzene with 212.8 nm (5^{th} harmonic Nd:Yag) excitation.

8.1 Benzene Vibrational Raman Modes

The benzene molecule (C_6H_6) may contain as many as 30 normal modes of vibration, based upon $3N-6$ (N is the number of atoms, i.e., 12) for nonlinear molecules. Table 8.1 contains a summary of the vibrational modes from Purdue University's website. The vibrational modes were calculated using the HyperChem Model (www.hyper.com), a commercially available product for the investigation of

chemical bonds and structures. The values in Table 8.1 show the calculated vibrational frequencies that may differ from the experimentally determined values by 10-30%. The modes that are vibrationally IR active have the approximate relative intensities shown in the table.

Table 8.1. Benzene normal vibrational modes (3N-6, totaling 30) from Purdue [2007]

<i>Benzene Vibrational Modes</i>				
10–30% different than observed				
Benzene Modes	cm ⁻¹	mode	IR Active?	Raman Active?
	3206	a _{1g}	no	yes
2 modes	3195	e _{1u}	yes (0.69)	no
2 modes	3187	e _{2g}	no	yes
	3184	b _{1u}	no	no
2 modes	1767	e _{2g}	no	yes
2 modes	1579	e _{1u}	yes (0.095)	no
	1366	b _{2u}	no	no
	1329	a _{2g}	no	no
	1276	a _{1g}	no	yes
2 modes	1222	e _{2g}	no	yes
	1179	b _{2u}	no	yes
2 modes	1146	e _{1u}	yes (0.0085)	no
	1028	b _{1u}	no	no
	1012	b _{2g}	no	no
2 modes	989	e _{2u}	no	no
2 modes	891	e _{1g}	no	yes
	744	a _{2u}	yes (1.0)	no
2 modes	648	e _{2g}	no	yes
	618	b _{2g}	no	no
2 modes	371	e _{2u}	no	no

The published literature generally uses one of two standard labeling schemes for the vibrational modes of benzene. The vibrational modes of benzene have been labeled ν_1 through ν_{20} by both G. Herzberg (Nat. Res. Council Canada) and by E. B. Wilson (Harvard); however, their respective assigned numbers are different. A comparison of the labels for vibrational modes by Herzberg and Wilson is provided in Table 8.2 to avoid confusion when surveying the literature, and a more detailed

version of this table is provided in Appendix K. Throughout this dissertation, the Herzberg naming convention is used and a summary of the labeling of the vibrational modes is listed in Table 8.3.

Table 8.2. Herzberg and Wilson mode assignment comparison.

Comparison of Wilson and Herzberg Notation		
mode	E. Bright Wilson Harvard	Gerhard Herzberg Nat. Res. Council Canada
a_{1g}	v_2	v_1
a_{1g}	v_1	v_2
a_{2g}	v_3	v_3
a_{2u}	v_{11}	v_4
b_{2g}	v_5	v_7
b_{2g}	v_4	v_8
b_{1u}	v_{13}	v_5
b_{1u}	v_{12}	v_6
b_{2u}	v_{14}	v_9
b_{2u}	v_{15}	v_{10}
e_{1g}	v_{10}	v_{11}
E_{1u}	v_{20}	v_{12}
e_{1u}	v_{19}	v_{13}
e_{2g}	v_7	v_{15}
e_{2g}	v_8	v_{16}
e_{2g}	v_9	v_{17}
e_{2g}	v_6	v_{18}
e_{2u}	v_{17}	v_{19}
e_{2u}	v_{16}	v_{20}
E_{2g}	v_1+v_6	v_2+v_{18}

The non-resonant Raman spectra of liquid benzene resulting from 488 nm (Argon-Ion Laser) excitation is shown for comparison in Figure 8.1. The strong feature between 0 and 200 cm^{-1} is due to the Rayleigh scattered return and is not a vibrational mode of benzene. Notice that it is not possible to see every vibrational mode, either due to low signal strength, or noise, or a lack of detection sensitivity as well as possible changes in the symmetry that can affect which modes are Raman active.

Table 8.3. Benzene vibrational modes using Herzberg notation.

Benzene vibrational modes Herzberg notation			
ν_1	3062 cm^{-1}	a_{1g}	CH stretch
ν_2	992 cm^{-1}	a_{1g}	ring stretch
ν_3	1326 cm^{-1}	a_{2g}	CH bend
ν_4	673 cm^{-1}	b_{1u}	CH bend
ν_5	3068 cm^{-1}	b_{1u}	CH stretch
ν_6	1010 cm^{-1}	b_{2g}	ring deform
ν_7	995 cm^{-1}	b_{2g}	CH bend
ν_8	703 cm^{-1}	b_{2u}	ring deform
ν_9	1310 cm^{-1}	b_{2u}	ring stretch
ν_{10}	1150 cm^{-1}	b_{2u}	CH bend
ν_{11}	849 cm^{-1}	e_{1g}	CH bend
ν_{12}	3063 cm^{-1}	e_{1u}	CH stretch
ν_{13}	1486 cm^{-1}	e_{1u}	ring stretch and deform
ν_{14}	1038 cm^{-1}	e_{1u}	CH bend
ν_{15}	3047 cm^{-1}	e_{2g}	CH stretch
ν_{16}	1596 cm^{-1}	e_{2g}	ring stretch
ν_{17}	1178 cm^{-1}	e_{2g}	CH bend
ν_{18}	606 cm^{-1}	e_{2g}	ring deform
ν_{19}	975 cm^{-1}	e_{2u}	CH bend
ν_{20}	410 cm^{-1}	e_{2u}	ring deform

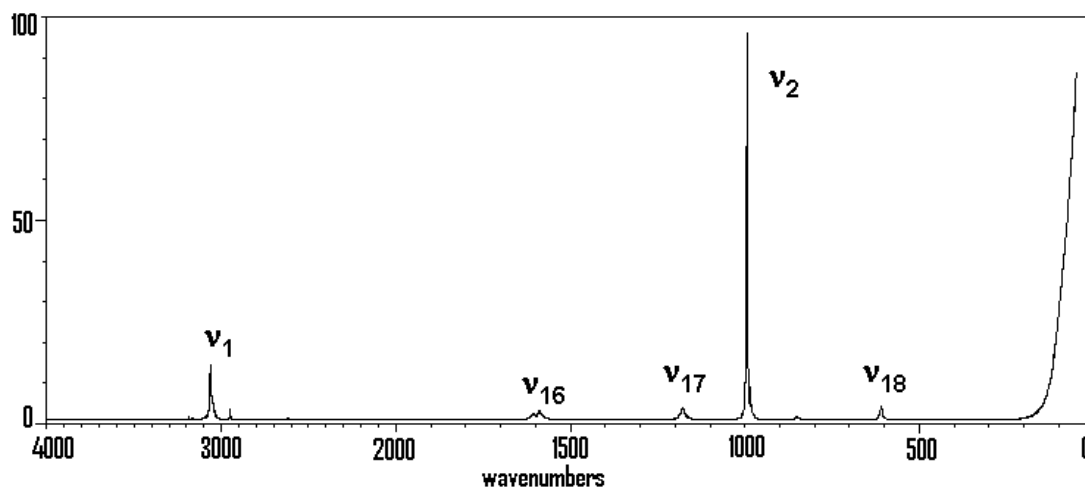


Figure 8.1. Benzene Raman spectra with 488 nm excitation <http://riodb01.ibase.aist.go.jp/sdbs/> (National Institute of Advanced Industrial Science and Technology, 10/11/2006)

8.2 Benzene Resonance-Raman Spectra

The resonance-Raman spectra of benzene are reported for excitation in the dipole forbidden ${}^1B_{2u}$ electronic transition band near 259 nm. Pre-resonance and

resonance gains are found by using small steps (0.12 to 0.25 nm) in wavelength around the excitation wavelength. The step size is determined based upon the limited bandwidth of the OPO output, which in our case is relatively large, and results in a full-width half-maximum of $\sim 40 \text{ cm}^{-1}$ (see Figure 5.6) which corresponds to a bandwidth of $\sim 0.25 \text{ nm}$ at 259 nm. The large bandwidth of the laser limited the practical resolution that is achievable, and the wavelength steps of the excitation source were selected to be equivalent to $\sim 1/2$ of the measured bandwidth. Thus, each wavelength has some overlap with the previous step of the excitation wavelength; however, the band center that contains the majority of the energy is shifted. An overlay of the vapor-phase absorption spectrum of benzene and the steps in the laser excitation wavelength is presented in expanded scale of Figure 8.2.

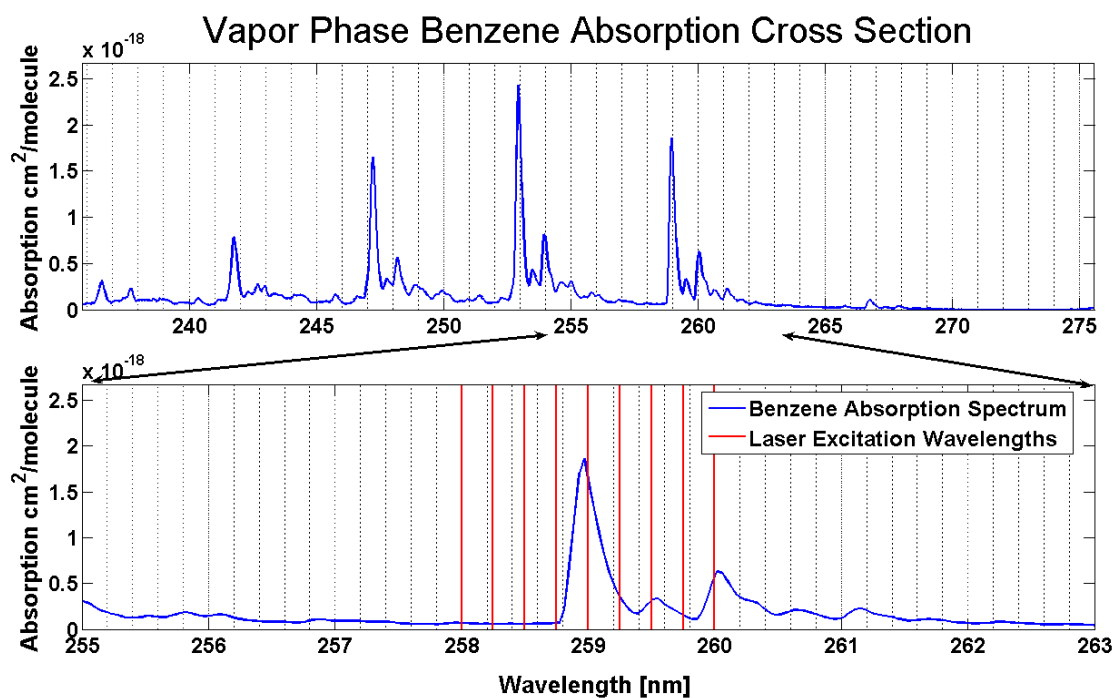


Figure 8.2. High resolution vapor phase benzene absorption spectra ${}^1\text{B}_{2u}$ band (blue, [Etzkorn, 1999]), and laser excitation wavelengths (red)

A comparison of the resonant (258.88 nm excitation) and off-resonant (430 nm excitation) Raman spectra of benzene is shown in Figure 8.2. All normalization corrections described in Chapter 6 have been performed, but the gain factor has not been included. The correction for the absorption is not performed in this figure in order to clearly display the data for comparison. Figure 8.3 is labeled with the modes of vibration corresponding to the results shown in the spectrum. The vibrational spectral features that are observed are due to ν_2 , ν_8 , and ν_{18} modes. The first triplet results from ν_2 , along with $2 \times \nu_8$, and $2 \times \nu_{18}$, and this pattern is then repeated as each mode combines with ν_2 ; this progression is summarized in Table 8.4. Thus the first set of triplet spectra consist primarily of ν_2 (993 cm^{-1}) along with the combination of $2 \nu_{18}$ ($606 + 606 \text{ cm}^{-1}$), and $2 \nu_8$ ($703 + 703 \text{ cm}^{-1}$). When resonance occurs, the particular resonating bonds are so strongly excited that we observe combinations and overtones occurring in the resulting spectra.

Table 8.4. Resonance-Raman Modes in Benzene Corresponding to Figure 8.3.

Benzene Resonant Raman 258.88 nm			
		$+\nu_2$	$+2\nu_2$
ν_2	$\sim 1010 \text{ cm}^{-1}$	$\sim 2006 \text{ cm}^{-1}$	$\sim 3000 \text{ cm}^{-1}$
$2\nu_{18}$	$\sim 1242 \text{ cm}^{-1}$	$\sim 2235 \text{ cm}^{-1}$	$\sim 3226 \text{ cm}^{-1}$
$2\nu_8$	$\sim 1413 \text{ cm}^{-1}$	$\sim 2400 \text{ cm}^{-1}$	$\sim 3400 \text{ cm}^{-1}$

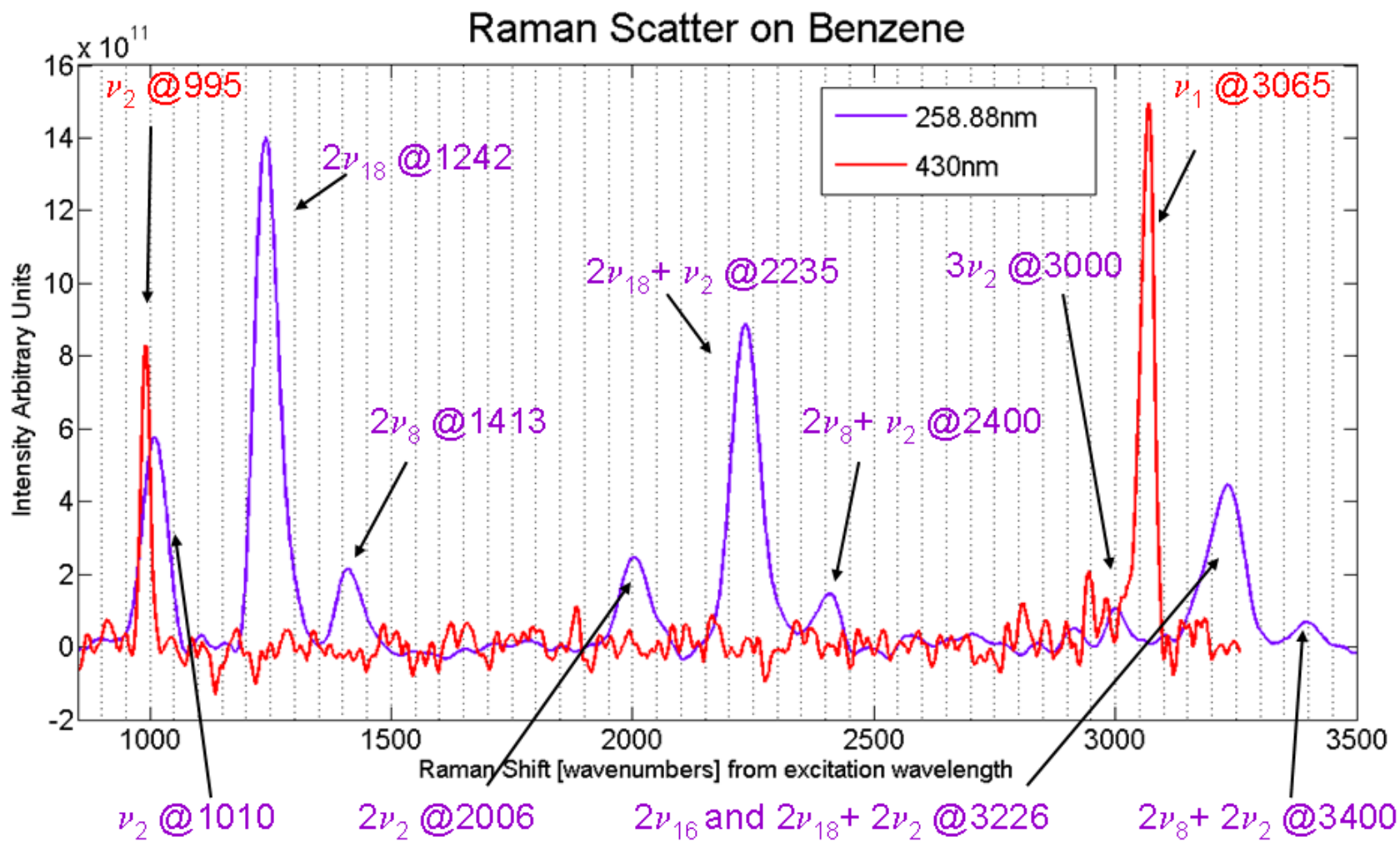


Figure 8.3. Benzene resonant and non-resonant Raman comparison

The resonance-Raman spectrum of benzene was recorded while stepping through a range of excitation wavelengths. Figure 8.4 shows the resonance enhanced Raman spectra for ν_2 and $2\nu_{18}$, for a selected range of wavelengths. The wavelength response of the system is considered to be uniform over the small tuning range used (2 nm). By stepping the excitation wavelength in 0.25 nm steps from 258.75 nm to 259 nm, one can clearly see a large increase in the Raman scattered signal. The Raman scattered line, which is barely detectable above the noise of the system is suddenly quite clearly defined as the resonance is approached. Figure 8.5 shows the full Raman spectra for benzene for four different wavelengths of excitation (258.88 nm, 259 nm, 259.12 nm, and 259.25 nm). The spectra seen in Figure 8.4 appear to shift with excitation wavelength which might suggest a strengthening of the bonds within the benzene molecule as the excitation wavelength is tuned across resonance.

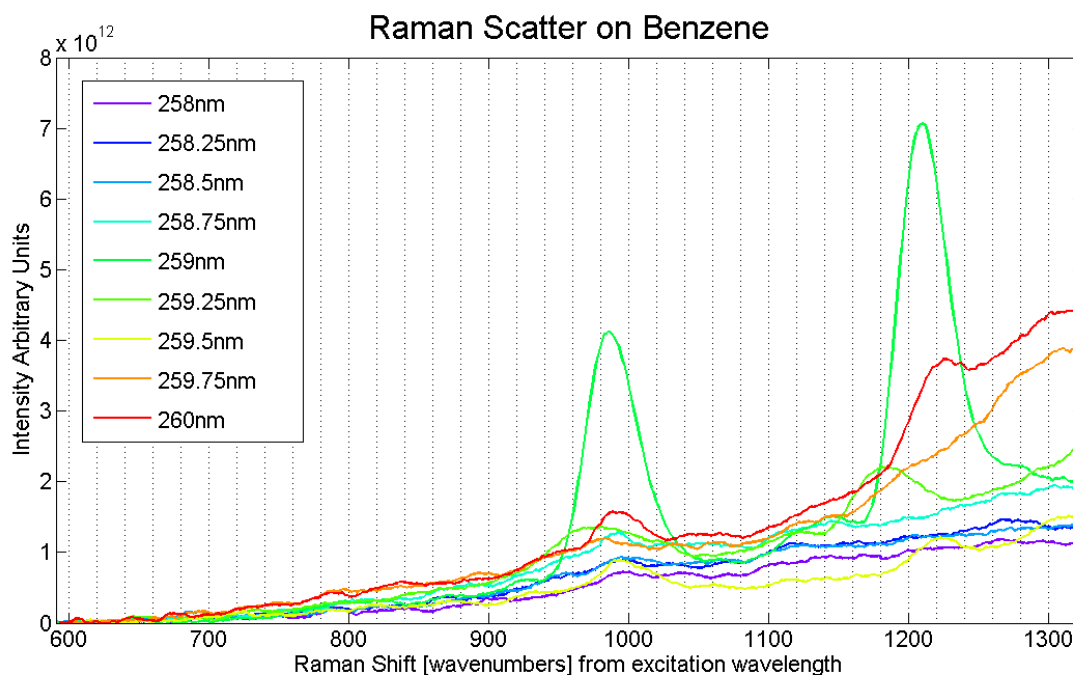


Figure 8.4. Resonant Raman spectra of benzene for nine different wavelengths of excitation 258–260 nm

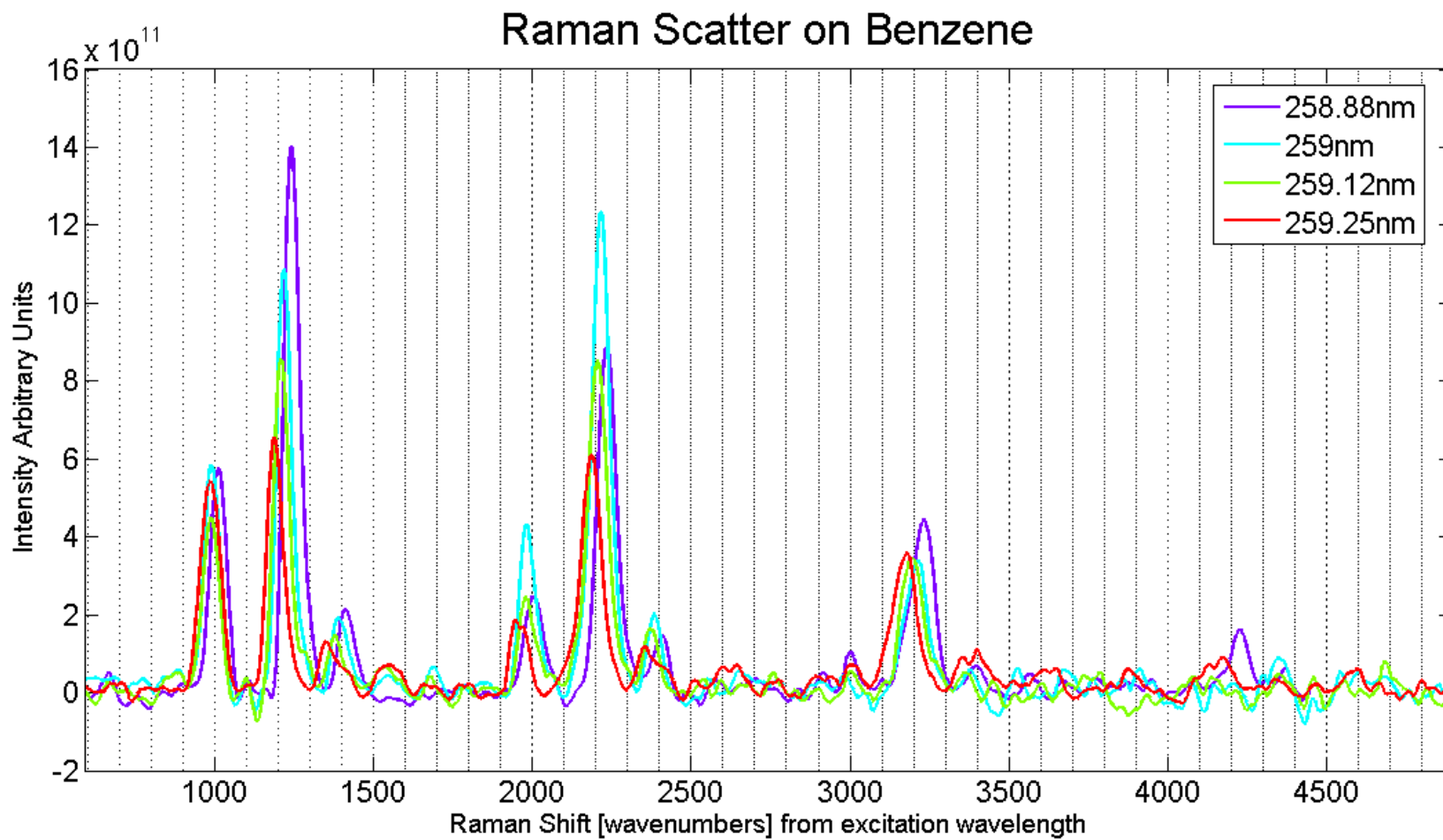


Figure 8.5. Resonance-Raman spectrum of benzene

Resonance-enhanced Raman scatter was also found when tuning across the absorption maxima located near 247.2 nm and 253 nm (see Figure 7.1). At 247.2 nm and 253 nm excitation, the maxima of the Raman scatter coincide with the peaks in the absorption spectra of the vapor phase benzene, as was the case for 259 nm excitation. The resonantly enhanced ν_2 and $2\nu_{18}$ is shown in Figure 8.6 for excitation with 247.2 nm, also with shifts in the excitation wavelength of ± 0.5 nm, and Figure 8.7 shows excitation with 253 nm along with excitation changes of ± 0.5 nm. The retrieved data are consistent with the idea that a bubble, or perhaps a collection of molecules that are no longer ordered enough to act like a liquid, becomes trapped between the liquid benzene and that sapphire window of the 90° scattering cell. This collection of molecules then acts like a vapor, and takes on the absorption characteristics of vapor-phase benzene.

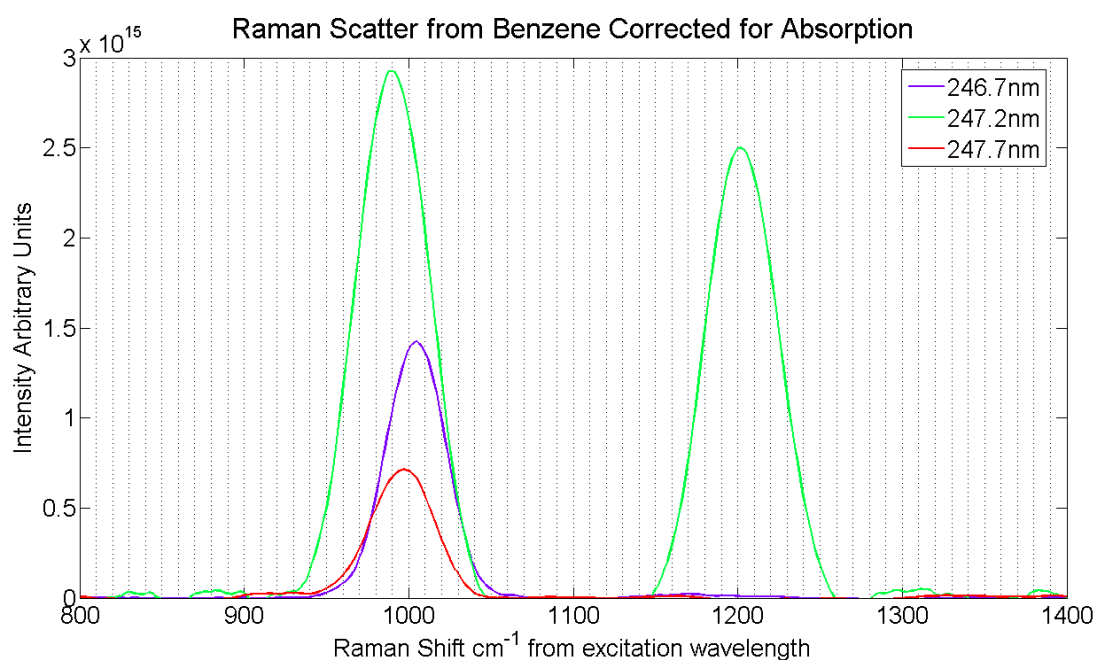


Figure 8.6. Resonance-enhanced Raman spectra around 247.2 nm.

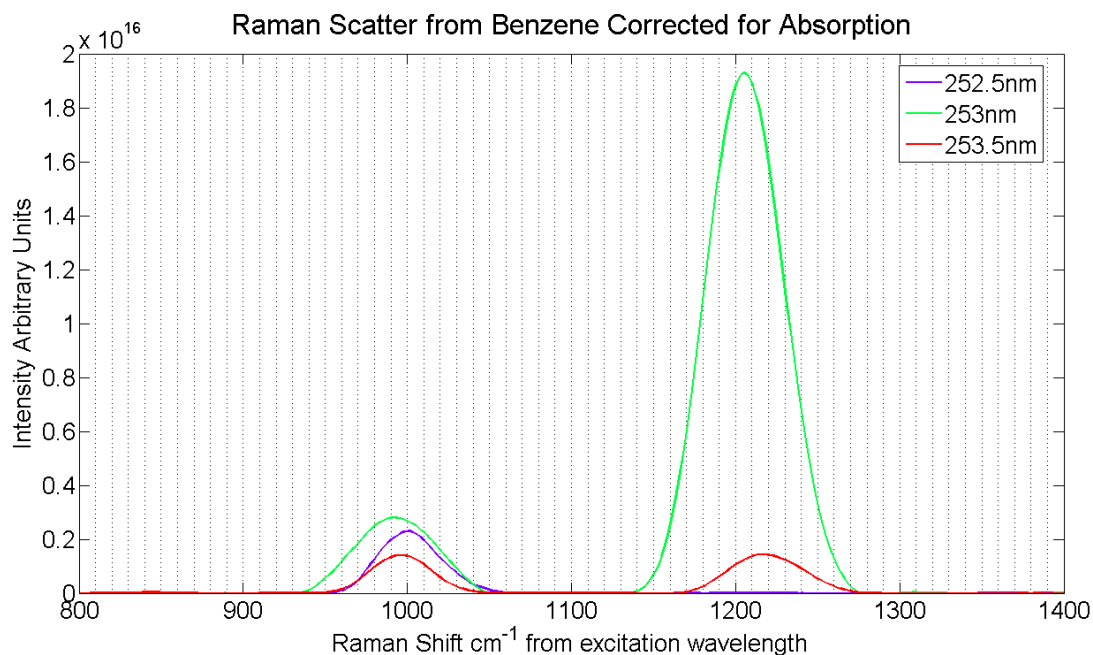


Figure 8.7. Resonance-enhanced Raman spectra around 253 nm

8.2.1 Concentration Effects

The concentration of benzene was varied to study the saturation effects of the Raman signal at several density levels. The ν_2 Raman line of benzene was recorded for four different concentrations of benzene in *n*-heptane as shown in Table 8.5.

Table 8.5. Benzene experiment concentrations

Concentration (Molarity)	Number Density (#/cm³)
0.25 M	$1.51 \times 10^{20} \pm 1.51 \times 10^{18}$
1 M	$6.02 \times 10^{20} \pm 6.02 \times 10^{18}$
5 M	$3.01 \times 10^{21} \pm 3.01 \times 10^{19}$
11.25 M (Pure)	$6.78 \times 10^{21} \pm 6.78 \times 10^{19}$

The ν_2 Raman lines for 11.25 M and 5 M were measured under both resonance and non-resonance excitation conditions; however, at the lower 1 M and 0.25 M concentrations the ν_2 line was only visible with resonance excitation. Figures 8.8 and 8.9 show the Raman spectra for different concentrations of benzene at different

excitation wavelengths under resonant (ultraviolet) and non-resonant (visible) conditions.

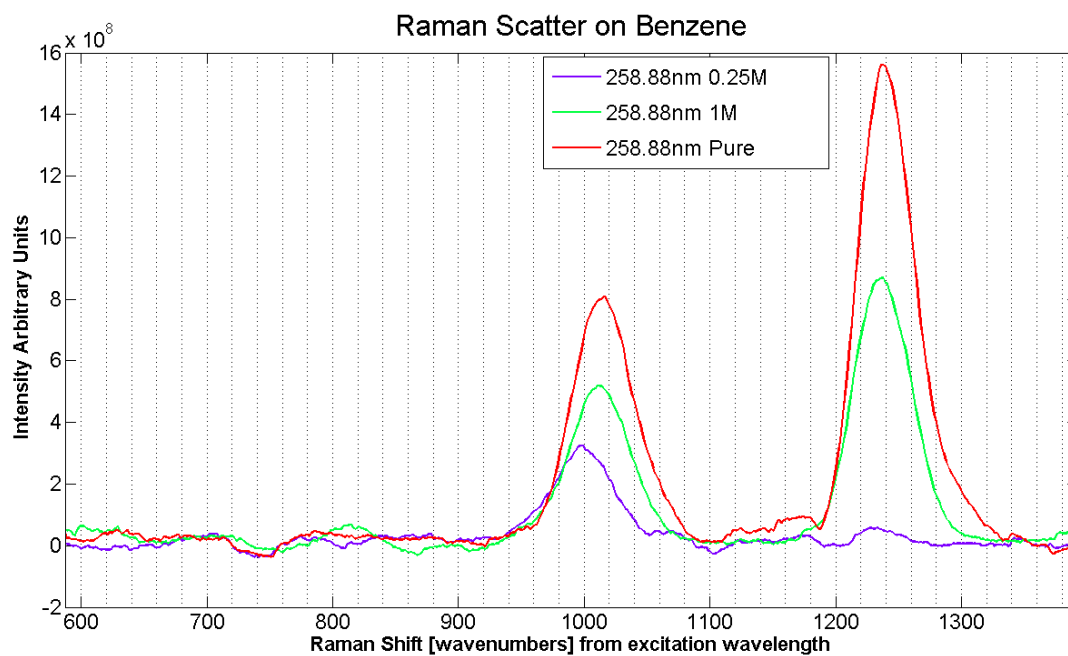


Figure 8.8. Concentration effects on Raman scattered intensity for resonant excitation

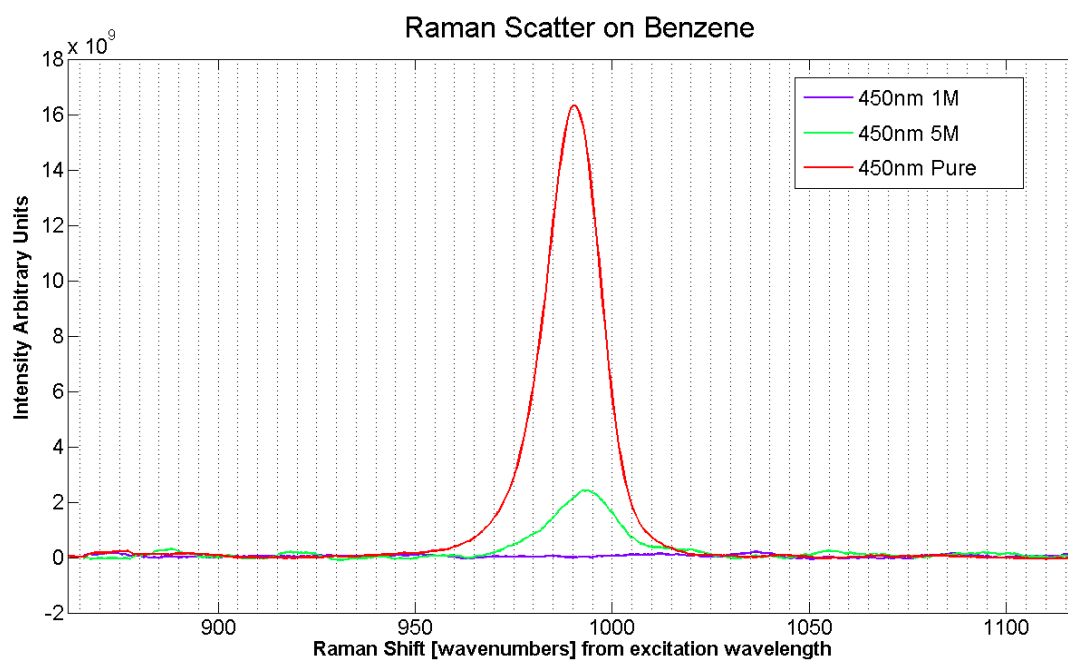


Figure 8.9. Concentration effects on Raman scattered intensity for visible excitation

As the concentration is decreased, the resonance-enhanced Raman scatter at 258.88 nm is the only means for detecting the presence of benzene above the noise floor for our system. The Raman scatter in the visible at 450 nm required much higher concentrations in order to detect a signal above the noise floor of the system. The problem from absorption arising at high concentrations does not exist when applied to lidar. In the free atmosphere concentrations of pollutants are generally low and dispersed, or may appear in trace concentrations as smears on surfaces.

8.2.2 Theoretical Mechanism of Scattering in Benzene $^1B_{2u}$ Region

We have studied the resonant-enhanced Raman scattering in benzene that occurs in the dipole forbidden transition $^1B_{2u}$ region. Because this transition is dipole forbidden, the A-term resonance-enhanced Raman scattering cannot occur. Examining the resonant spectra shows quite clearly that a number of overtones and combination modes are present. The overtones and combination modes are functions of A-term scattering, while pure fundamental modes are associated with B-term scattering. In order to reconcile this discrepancy, Zgierski [1977] described a process of interference between two modes, one allowed and one forbidden. Moving one step further, Korenowski *et al.* [1977] prepared a model of a special case of A-term scattering in the forbidden electronic transitions. By coupling a Raman active mode with a vibrational coupling mode, it is possible for “forbidden transitions to contribute to the scattering cross section of certain totally symmetric modes” [Korenowski *et al.* 1977]. Their approach makes use of the Born–Oppenheimer approximation, which allows the separation of the nuclear and electronic motions. As

envisioned, a significant nuclear displacement is needed in order to prevent overlap integrals from becoming zero, and it is not necessarily possible, or easy, to treat the separate motions of the atoms.

8.2.3 Comparison of Resonance-Raman Spectra of Benzene

The Raman spectra for benzene has been explored and recorded by many research scientists. A comparison with the data collected during this research with the results of Zeigler and Hudson [1981] are presented for the cases of benzene resonant and non-resonant Raman scattering. They recorded spectra of benzene Raman scattering when excited at 354.7 nm (3rd harmonic Nd:YAG) and at 212.8 nm (5th harmonic Nd:YAG, resonant) excitation and the results are shown in Figure 8.9. They obtained the resonant Raman spectra of benzene in the region near the dipole forbidden transition band, ${}^1B_{1u}$, using the 5th harmonic of the Nd:YAG laser excitation.

Zeigler and Hudson [1981], concluded that the D_{6h} symmetry contains only two totally symmetric normal modes of vibration ν_1 (CH-stretch) and ν_2 (ring-stretching). The two most intensely scattered Raman lines with non-resonant excitation are the ν_1 and ν_2 , observed in Figures 8.1 (488 nm excitation), 8.2 (430 nm excitation), and 8.10 (354.7 nm excitation, top). When near resonance, ν_2 is the only fundamentally enhanced mode of vibration, however, and ν_1 (CH-stretch mode 3062 cm^{-1}) is absent within Zeigler and Hudson's data. My results are consistent with the data collected by them when we compare Figures 8.3 and 8.10.

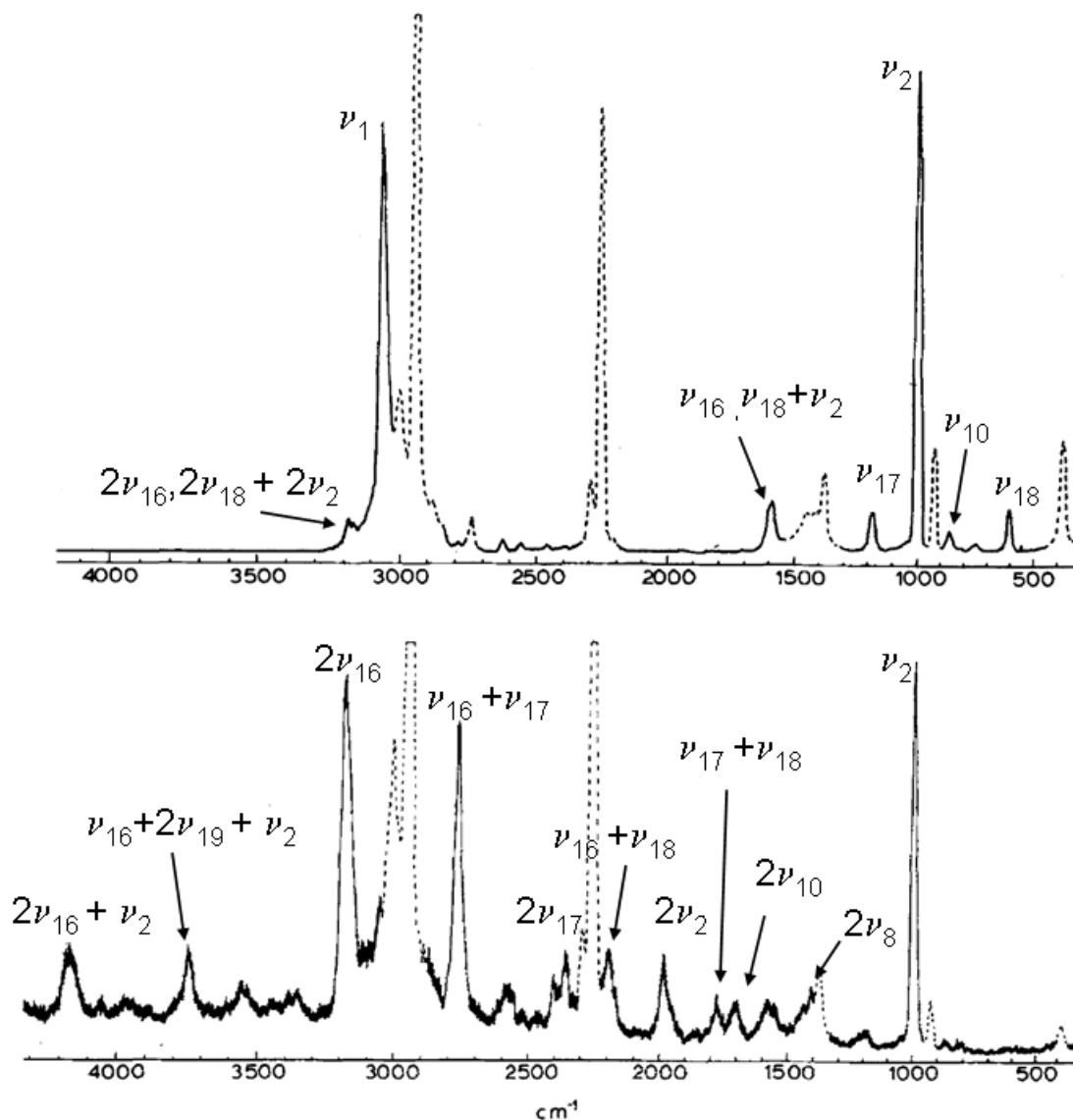


Figure 8.10. Benzene Raman spectra at 354.7 nm excitation (top) and 212.8 nm excitation (bottom) dotted lines are spectra due to the solvent acetonitrile. (The original plot has been changed to reflect the naming convention of Herzberg) [Ziegler and Hudson, 1981]

8.3 Toluene Raman Scatter

The Raman spectra of toluene, (C_7H_8) a mono-substituted benzene derivative, has been investigated and compared with previously published spectra. When resonance occurs the signals are enhanced, and the combinational and overtone modes are observed as in the case of benzene. Figure 8.11 shows the non-resonant

Raman spectra of toluene at 488 nm. Figure 8.12 shows the non-resonant Raman spectra of a 50% solution of toluene and acetonitrile with 514.5 nm excitation.

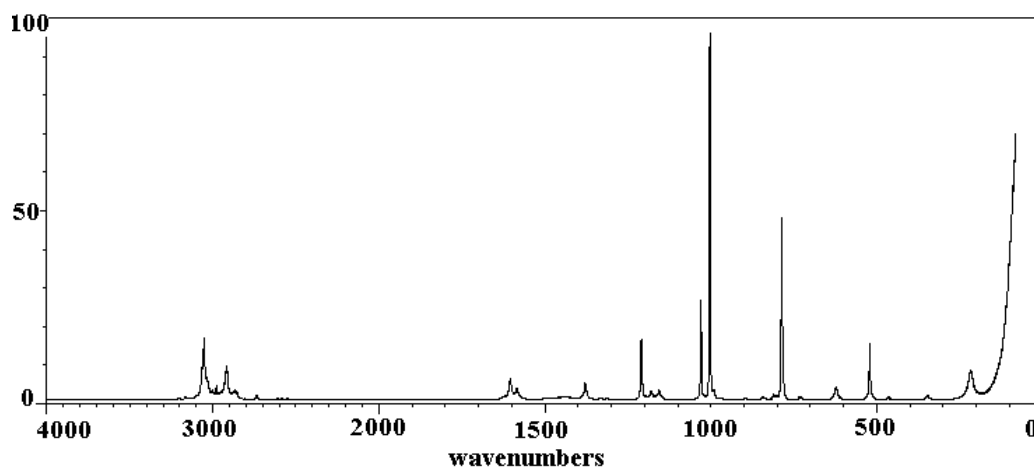


Figure 8.11. Toluene Raman spectra with 488 nm excitation <http://riodb01.ibase.aist.go.jp/sdbs/> (National Institute of Advanced Industrial Science and Technology, 10/11/2006)

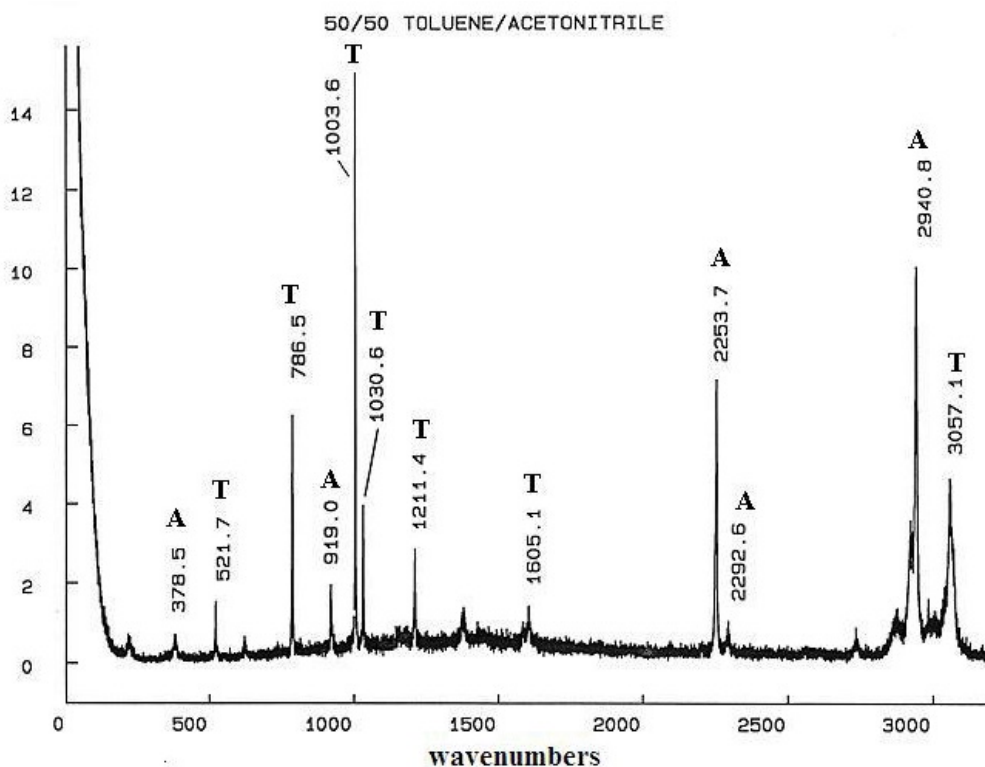


Figure 8.12. Toluene Raman spectra with 514.5 nm excitation. 'T' labels represent toluene lines, 'A' labels represent acetonitrile lines. <http://www.chemistry.ohio-state.edu/~rmccreer/freqcorr/images/toluene.html>

8.3.1 Resonance-Enhanced Raman Scattering in Toluene

A resonance enhancement of the Raman scattering in toluene has also been recorded. The resonant enhancement in toluene was also found to coincide with the vapor phase absorption peak. Tuning through the vapor phase absorption peak yields a maximum in the resonance Raman response at 266.83 nm, and the resonance Raman spectra is shown in Figure 8.13. The enhancement shows a narrowband of excitation around 266.83 nm in which the resonance Raman scattering occurs.

The Raman spectrum for resonant (266.83 nm) and non-resonant (430 nm) excitations can be seen in Figure 8.14. The resonant spectra of toluene like benzene, also contains many combinational and overtone modes.

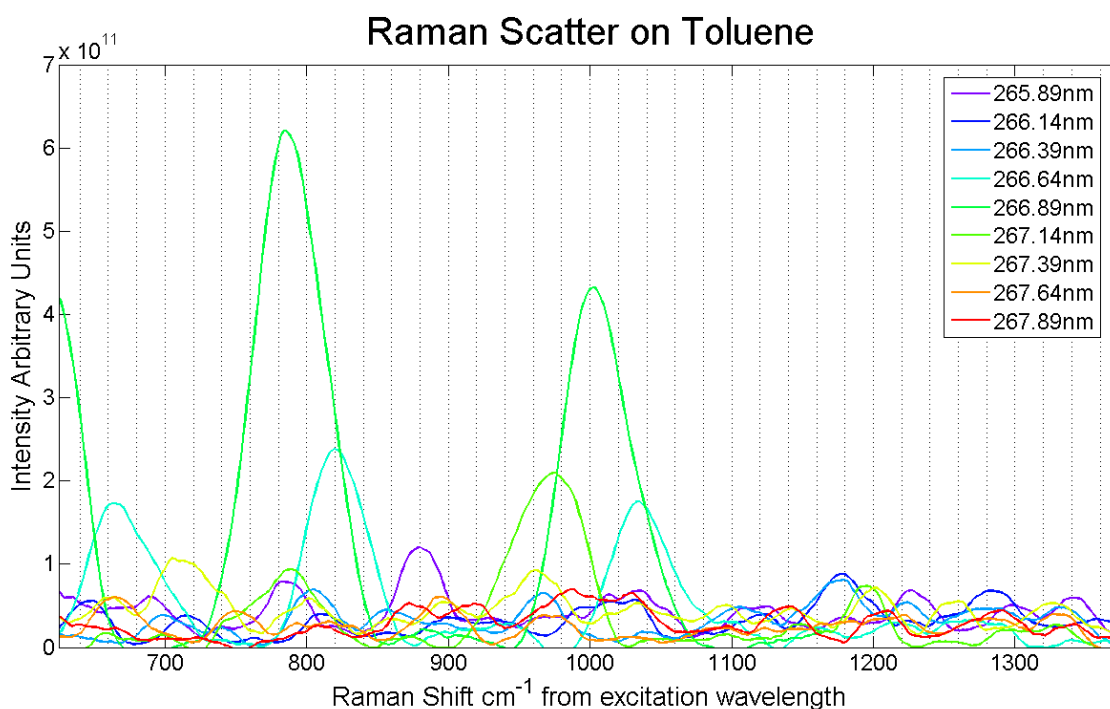


Figure 8.13. Toluene resonance-Raman spectra for excitation wavelengths around 266.83nm

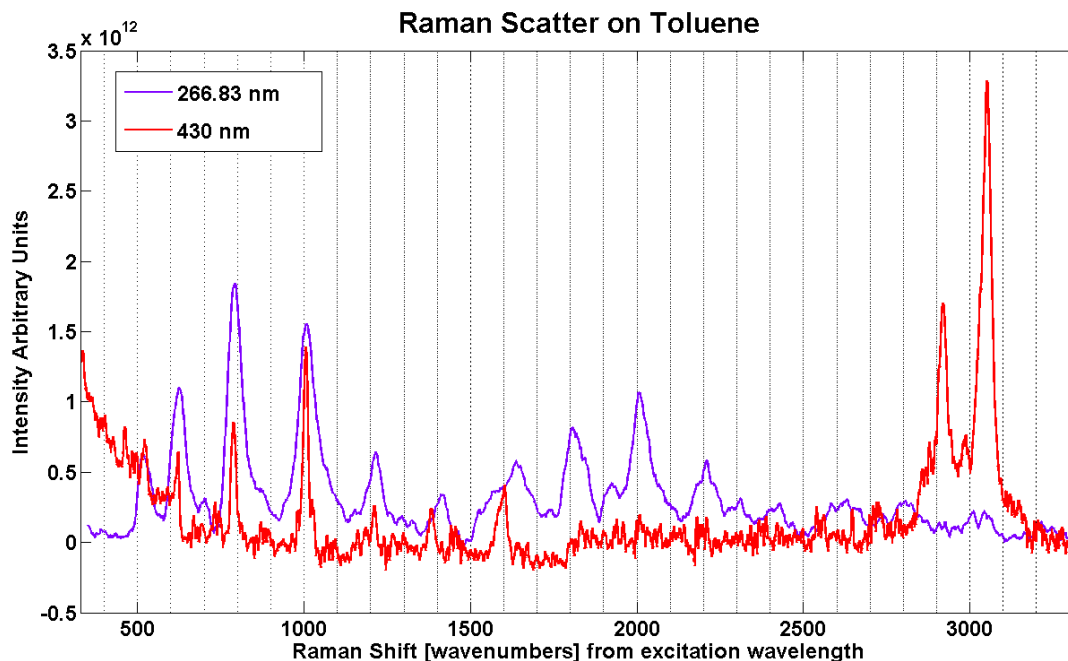


Figure 8.14. Resonance enhanced Raman scattering in toluene

As seen in Figure 8.14 the resonance excitation at 266.83 nm; are four strong fundamental modes at 625 cm^{-1} , 780 cm^{-1} , 1008 cm^{-1} , and 1215 cm^{-1} , that can also been seen in the non-resonant case. These modes are found to combine with the 1004 cm^{-1} (C=C stretch mode, similar to the benzene breathing mode) and create strong combinational lines at $\sim 1800 \text{ cm}^{-1}$ ($780 + 1004$), 2008 cm^{-1} (2×1004), and 2220 cm^{-1} ($1215 + 1004$). The fundamental 625 cm^{-1} mode is seen combined with the 1008 cm^{-1} mode, in the broad peak from 1585 cm^{-1} to 1650 cm^{-1} , resulting from the overlap of 2 fundamental modes around 1600 cm^{-1} and the aforementioned combinational mode. Similar to benzene, toluene has strong combinational modes that are coupled to the breathing mode.

8.4 Summary

A new region of resonance-enhanced Raman scattering within benzene has been identified. By tuning an OPO through the ${}^1B_{2u}$ absorption band in benzene around 259 nm, a resonance in the Raman scattering is examined. Also, at resonance a significant contribution to overtones and combinational modes are clearly observed in the benzene data collected. These modes have been compared with the previous work of Ziegler and Hudson [1981], who performed resonance measurements on benzene using 212.8 nm (5th harmonic Nd:YAG) excitation within the ${}^1B_{1u}$ forbidden electronic transition. As seen with previous resonance experiments in the ${}^1B_{1u}$ and ${}^1B_{2u}$ absorption bands of benzene, the modes that experience the greatest enhancement come from the e_{2g} vibration.

In both benzene and toluene, a strong resonance enhancement was found when tuning through their respective absorption peaks. The excitation energy is found to match the absorption frequency of the breathing modes of both toluene and benzene, resulting in strong combination modes with the fundamental breathing mode ($\sim 1000\text{ cm}^{-1}$).

Chapter 9: Summary, Conclusions, and Future Work

9.1 Summary

The objective of this dissertation is two-fold: first, devise a method to investigate resonance enhanced Raman scattering and, second, record and analyze the characteristics of resonance-enhanced Raman spectra. The research has investigated the resonance-Raman processes and determined how the prior work of our laboratory in developing Raman lidar [Philbrick *et al.* 2006] can be extended to take advantage of resonance processes for detection of trace levels of chemical species. In collaboration with Todd Chadwick (doctoral student at North Carolina State University in Professor Hans Hallen's Optics Laboratory) an experiment was setup, and the laboratory experiments were performed.

In the majority of the papers published on resonance enhanced Raman scattering, the wavelengths of excitation are located at common laser wavelengths, and these wavelengths do not normally align with any of the peaks in absorption for the electronic transitions. Several publications have reported resonance Raman in benzene with large wavelength steps [Ziegler and Hudson, 1981; Asher and Johnson, 1985; and in a few cases as finely as ~4 nm steps [Sension *et al.*, 1991; Gerrity *et al.*, 1985]. In absorption bands of species such as benzene, these step sizes leap over the fine structure of the ${}^1B_{2u}$ absorption band. In order to examine the true resonance enhancement of Raman scattering, a tunable laser must be matched precisely, or nearly precisely, the absorption lines. An Optical Parametric Oscillator (OPO) is used

to investigate the absorption structure of benzene with nearly continuous tuning of the laser beam, using step sizes as small as 0.12 nm to 0.25 nm.

The Raman setup utilized a 90° scattering geometry, meaning the beam paths of the excitation and scattered wavelengths were perpendicular to permit measurements in an extremely high optical density material. The samples for the experiment were held in a Teflon container to ensure no chemical reactivity, and the windows of the scattering cell were made of sapphire to assure high transmission over the ultraviolet region.

The Raman scattered light was collected via a matched lens system to collimate and focus the light into the Jobin Yvon Triple Spex 1877 spectrometer. The spectrometer was fitted with UV-blazed gratings for maximum throughput, and the Raman scattered light was then imaged utilizing an Andor EM-CCD camera with a quantum efficiency of 35% throughout the ultraviolet region.

The collected images of the spectrum were then processed using a sequence of MATLAB routines that were created for our data analyses. The primary goals of the MATLAB routines are to eliminate noise, improve signal quality by removing background, to smooth and filter the data, and also to plot and display the data for interpretation. The Raman scattered lines were corrected in order to calculate a resonance gain. Finally, the collected and plotted spectra were analyzed and interpreted in order to identify the dominant modes within the Raman scattered spectra.

9.2 Conclusions

High resolution absorption spectra of benzene (gas and liquid) have shown well defined absorption peaks in the region 230 nm to 270 nm. Resonance and pre-resonance-enhanced Raman scattering gains in this region were investigated using small steps (0.12 to 0.25 nm) in the excitation wavelength from a tunable laser to step through the forbidden ${}^1B_{2u}$ electronic transition of benzene. Resonance enhancement gains of 3 to 4 orders of magnitude over the normal Raman scattering signals are observed. Resonance enhancements occurring for excitation in the narrow bandwidth region near 259 nm (± 1 nm) have been examined with most interest (see Figure 8.4). The resonant enhancement is found to correspond more closely to the vapor-phase absorption spectra (at 247.2 nm, 253 nm, and 259 nm), than with the liquid absorption spectra. It may be possible that a bubble precursor, or perhaps a collection of molecules that are no longer sufficiently ordered to behave like a liquid, becomes trapped between the liquid benzene and the sapphire window. This layer responds to the absorption characteristics of the vapor phase benzene.

When the concentration of benzene was decreased, it became increasingly difficult to detect any normal Raman scattered intensity using visible wavelength scattering as shown in Figure 8.9; at even lower concentrations, the Raman scattering was still detected under conditions of resonance excitation as shown in Figure 8.8.

Finally, under resonance excitation at 259 nm, the Raman spectra of benzene shows a triplet of vibrational modes that are easily identifiable as overtones and combinational modes. The triplet is observed to repeat throughout the spectra

progressing by approximately 1000 cm^{-1} as combination modes with the ν_2 vibrational mode form.

9.3 Future Work

A continuation of the studies performed in this dissertation would be a worthwhile endeavor. An examination of the ${}^1\text{B}_{2u}$ absorption spectra of benzene (see Figure 7.1) shows many more absorption peaks, which could be potential targets for resonantly enhancing the Raman scattering. The continued use of an OPO laser cavity to tune through other peaks in the ‘fingerlike’ structure of the absorption of benzene should also result in resonant Raman scattering as the excitation scans the absorption spectral peaks. More in depth studies of the vapor-phase absorption peaks located at 247.2 nm and 253 nm should be undertaken.

The experiments described in this dissertation should also be repeated by replacing benzene (C_6H_6) with hexadeuterobenzene (C_6D_6). The effects of heavy hydrogen within the benzene molecule have been commonly studied in conjunction with the benzene molecule and lend additional information into the understanding of the vibrational modes.

Further interpretation of the Raman spectra of benzene and detailed investigations of the mechanisms by which the enhancement occurs should be undertaken. Because there are most likely to be significant nuclear displacements when resonant excitation is reached, it may not be logical to continue the use of the Born–Oppenheimer approximation. This factor would require developing an alternative analysis of the resonance enhancement within the ${}^1\text{B}_{2u}$ absorption region.

Through the examination of additional double- and triple-bonded materials, additional insight into the resonance processes could be retrieved, making it possible to study additional applications to lidar. Many polycyclic aromatic hydrocarbons are found in fossil fuels and are released with combustion. They can be found as particulates suspended in air. Adapting a lidar to take advantage of the resonance effect may allow increased detection and analysis of particulates.

In order to take advantage of the resonance-enhancement for application in Lidar two different scenarios are envisioned:

- 1) Replace the standard single wavelength laser with a tunable OPO cavity. This would allow wavelength changes when performing field measurements. By changing the wavelength it would be possible to resonantly excite different species without the need for specialized individual lidar systems. In order to efficiently detect the Raman scattered light a tunable etalon, variable filter array, or spectrometer is needed. Because the excitation wavelength is not a fixed wavelength, the Raman scattered returns will also no longer be fixed; as the wavelength of excitation is changed the scattered Raman spectra will also move to different wavelengths. Filtering the Raman spectra from the background signal levels will be a difficult obstacle to this experimental option.
- 2) Use of multiple solid state lasers (single wavelength) at properly chosen excitation wavelengths for resonance-enhancement of a family of molecules, or a specific type of bond. This would reduce the

difficulty caused by the background signal for variable wavelength excitation.

A type-II OPO cavity would improve resolution within the collected Raman spectra and permit a higher resolution study. Type-II OPO cavities maintain a more stringent phase-matching condition, which results in a narrower laser linewidth throughout the tuning region. A narrower laser linewidth would allow more detailed investigation of the absorption to be studied, and would help to avoid overlap of closely spaced Raman lines.

REFERENCES

- Abe, N., M. Wakayama and M. Ito. 1977. "Absolute Raman Intensities of Liquids," *Journal of Raman Spectroscopy*, Vol. 6, NO. 1.
- Albrecht, A.C. 1961. "On the Theory of Raman Intensities," *Journal of Chemical Physics*, Vol. 34, No. 5, pp. 1476–1484.
- Alpers, M., R. Eixmann, C. Fricke–Begemann, M. Gerding and J. Hoffner. 2004. "Temperature lidar measurements from 1 to 105 km altitude using resonance, Rayleigh, and Rotational Raman Scattering," *Atmospheric Chemical Physics*, Vol. 4, pp. 793–800.
- Andrews, D., 1930. "The Relation between the Raman Spectra and the Structure of Organic Molecules," *Physical Review*, Vol. 36, pp. 544–554.
- Ansmann, A., M. Riebesell, and C. Weitkamp. 1990. "Measurement of Atmospheric Aerosol Profiles with a Raman Lidar," *Optics Letters*, Vol. 15, No. 13.
- Apanasevich, P., and D. Ordabaev, 1966. "Stimulated Resonance Raman Scattering," *Zhurnal Prikladnoi Spektroskopii*, Vol. 4, No. 2, pp. 134–141.
- API. 1970. "Selected Ultraviolet Spectral Data (American Petroleum Institute Research Project 44)," Thermodynamics Research Center, Department of Chemistry, Texas A & M University. College Station, Texas. October.
- Asher, S. 1993. "UV Resonance Raman Spectroscopy for Analytical, Physical and Biophysical Chemistry Part 1," *Analytical Chemistry A*, Vol. 65, No. 2, pp. 59–66.

- Asher, S. 1993. "UV Resonance Raman Spectroscopy for Analytical, Physical and Biophysical Chemistry Part 2," *Analytical Chemistry A*, Vol. 65, No. 4, pp. 201–210.
- Asher, S., 1988. "UV Resonance Raman Studies of Molecular Structure and Dynamics: Applications in Physical and Biophysical Chemistry," *Annual Review of Physical Chemistry*, Vol. 39, pp. 537–588.
- Asher, S., 1984. "Ultraviolet Resonance Raman Spectrometry for Detection and Speciation of Trace Polycyclic Aromatic Hydrocarbons," *Analytical Chemistry* Vol. 56, pp. 720–724.
- Asher, S., and C. Johnson. 1985. "UV Resonance Raman Excitation Profile through the ${}^1B_{2u}$ State of Benzene," *Journal of Physical Chemistry*, Vol. 89, pp. 1375–1379.
- Asher, S., R. Bormett, X. Chen, D. Lemmon, N. Cho, P. Peterson, M. Arrigoni, L. Spinelli and J. Cannon. 1993. "UV Resonance Raman Spectroscopy Using a New CW Laser Source: Convenience and Experimental Simplicity," *Applied Spectroscopy*, Vol. 47, No. 5, pp. 628–633.
- Axdahl, E. Picture of Sundog. New Ulm. Mn.
<http://en.wikipedia.org/wiki/User:Axda0002>)
- Bayliss, N., and E. McRae. 1954. "Solvent Effects in the Spectra of Acetone, Crotonaldehyde, Nitromethane and Nitrobenzene," *Journal of Physical Chemistry*, Vol. 56, pp. 1006–1011.

- Beckmann, A., P. Baiertl, and W. Kiefer. 1986. "Theory of Coherent Anti-Stokes Continuum Resonance Raman Scattering in Diatomic Molecules," *Journal of Raman Spectroscopy*, Vol. 17, pp. 107–111.
- Behrendt, A., and T. Nakamura. 2002. "Calculation of the calibration constant of polarization lidar and its dependency on atmospheric temperature," *Optics Express*, Vol. 10. No. 16, pp. 805-817.
- Behringer, J., and J. Brandmuller, 1956. *Z. Elektrochem., Ber. Bunsenges. Physical Chemistry*, Vol. 60, pp. 643.
- Behringer, J., 1974. "The Relation of Resonance Raman Scattering to Resonance Fluorescence," *Journal of Raman Spectroscopy*, Vol. 2, pp. 275–299.
- Berlman, I., 1971. Handbook of Fluorescence Spectra of Aromatic Molecules. Academic Press, New York.
- Berman, J. and L. Goodman. 1987. "The a_{2g} Mode in Ground State Benzene," *The Journal of Chemical Physics*, Vol. 87, No. 3, pp. 1479–1487.
- Brown, David, A. Willitsford, K. Shi, Z. Liu, C.R. Philbrick 2006. "Advanced Optical Techniques for Measurements of Atmospheric Constituents," *Proceedings of the 28th Annual Review of Atmospheric Transmission Models*, Lexington, MA, June.
- Calleja, J., J. Kuhl and M. Cardona. 1978. "Resonant Raman Scattering in Diamond," *Physical Review B*, Vol. 17, No. 2, pp. 876–883.
- Callomon, J., T. Dunn, and I. Mills. 1966. "Rotational Analysis of the 2600 Å Absorption System of Benzene," *Philosophical Transactions of the Royal*

Society of London. Series A, Mathematical and Physical Sciences, Vol. 259,
No. 1104, pp. 499–532.

Carey, P.R., 1982. Biological applications of Raman and resonance Raman Spectroscopies, Academic Press, New York.

Chadwick C.T. 2008. “Investigation of resonance Raman spectroscopy utilizing tunable deep ultraviolet excitation for materials characterization and application utility with preliminary studies involving aromatic hydrocarbons,” Ph.D. Dissertation. North Carolina State University, Physics Department.

Chamberlain, O., P. Robrish and H. Rosen. 1976. “Investigation of the use of the Resonance Raman Effect as an Environmental Monitor,” Lawrence Berkeley Laboratory Energy and Environment Division. University of California/Berkeley.

Chen, C. and Sedlacek A. 1996. “Revisiting Raman Lidar: Application of New Techniques to Improve System Performance,” *SPIE* Vol. 2833.

Chen, C., D. Heglund., M. Ray., D. Harder., R. Dobert., K. Leung., M. Wu. and A. Sedlacek. 1997. “Application of Resonance Raman Lidar for Chemical Species Identification,” Brookhaven National Laboratory, Upton, New York. Conference 970465–19.

Clark, R. and T. Dines. 1986. “Resonance Raman Spectroscopy, and its Application to Inorganic Chemistry.” *Angew. Chem. Int. Ed. Engl.* Vol. 25, pp. 131–158.

Clemesha, B., G. Kent, and R. Wright. 1966. “Laser Probing the Lower Atmosphere,” *Nature*, Vol. 209, pp. 184–185.

- Cleveland, F., and P. Porcelli. 1950. "Raman Spectra of Hydrocarbons. V. n-Hexane, n-Heptane, 2-Methylpentane, 3-Methylpentane, 2,4-Dimethylpentane, and 2,3-Dimethylbutane," *The Journal of Chemical Physics*, Vol. 18, No. 11, pp. 1459-1461.
- Collins, G., 1932. "Raman Spectra of a Series of Octanols," *Physical Review*, Vol. 40. pp. 829-834.
- Collis, R., 1964. "Laser Radar Echoes from the Clear Atmosphere," *Nature*, Vol. 203, pp. 508.
- Cooney, J., 1968. "Measurements on the Raman Component of Laser Atmospheric Backscatter," *Applied Physics Letters*, Vol. 12, No. 2, pp. 40-42.
- Damen, T., C. Leite and S. Porto. 1965. "Angular Dependence of the Raman Scattering from Benzene Excited by the He-Ne cw Laser," *Physical Review Letters*, Vol. 14, No. 1, pp. 9-11.
- Dines, T. University of Dundee. 2008.
<http://www.personal.dundee.ac.uk/~tjdines/Raman/RRTHEORY.HTM>
- Ding, K., W. Kranitzky, S. Fischer, and W. Kaiser. 1980. "Structured UV-Spectrum of Naphthalene Obtained by Ultrafast Two-Pulse Excitation," *Chemical Physics Letters*, Vol. 72, No. 1, pp. 39-42.
- Dirac, P. 1939. "A New Notation for Quantum Mechanics," *Proceedings of the Cambridge Philosophical Society*, Vol. 35, p. 416.
- Dixon, J. M.; Taniguchi, M.; Lindsey, J. S. 2005. "PhotochemCAD 2. A Refined Program with Accompanying Spectral Databases for Photochemical Calculations," *Photochemical and Photobiology*, Vol. 81, pp. 212-213.

- Dollish, Francis R., W. Fateley and F. Bentley. 1974. Characteristic Raman Frequencies of Organic Molecules. John Wiley and Sons, New York.
- Dorfer, T., M. Schmitt, and J. Popp. 2007. "Deep-UV surface-enhance Raman Scattering," *The Journal of Raman Spectroscopy*, Vol. 38, pp. 1379–1382.
- Du, H.; Fuh, R.-C. A.; Li, J.; Corkan, L. A.; Lindsey, J. S. 1998. "PhotochemCAD. A Computer-Aided Design and Research Tool in Photochemistry and Photobiology," *Photochemical and Photobiology*, Vol. 68, pp. 141–142.
- Dudik, J., C. Johnson, and S. Asher. 1985. "UV Resonance Raman Studies of Acetone, Acetamide, and N-Methylacetamide: Models for the Peptide Bond," *Journal of Physical Chemistry*, Vol. 89. pp. 3805–3814.
- Dunn, T., 1966. Chapter 6: The Spectrum and Structure of Benzene. In Studies on Chemical Structure and Reactivity. Edited by J. Ridd. John Wiley and Sons, New York.
- Exckhardt, G., 1966. "Selection of Raman Laser Materials," *Journal of Quantum Electronics*, Vol. 2, No. 1, pp. 1–8.
- Elterman, L., 1951. "The Measurment of Stratospheric Density distribution with the Search Light Technique," *Journal of Geophysical Research*. Vol. 56, No. 4, pp. 509–520.
- Elterman, L., 1954. "Seasonal Trends of Temperature, Density, and Pressure to 67.6 KM Obtained with the Searchlight Probing Technique," *Journal of Geophysical Research*. Vol. 59, No. 3, pp. 351–358.
- Environmental Protection Agency. 2008. www.epa.gov

- Esposito, S. and C. Philbrick. 1998. "Raman/DIAL technique for ozone measurements." *Proceedings of the Nineteenth International Laser Radar Conference*, NASA/CP-1998-207671/PTI, p. 407-410.
- Etzkorn, T., B. Klotz, S. Sørensen, I.V. Patroescu, I. Barnes, K.H. Becker, and U. Platt "Gas-phase absorption cross sections of 24 monocyclic aromatic hydrocarbons in the UV and IR spectral ranges," *Atmospheric Environments*, Vol. 33, pp. 525-540.
- Fabelinskii, I. L. 1998 "Seventy Years of Combination (Raman) Scattering," From the History of Physics. *Physics – Uspekhi. Russian Academy of Sciences*, Vol. 41, No. 12, pp. 1229-1247.
- Faraday, M. 1825. "On New Compounds of Carbon and Hyrdogen, and on Certain Other Products Obtained during the Decomposition of Oil by Heat," *Philosophical Transactions of the Royal Society of London*, Vol. 115, pp.440-466.
- Faris, G. and R. Copeland. 1997. "Wavelength dependence of the Raman Cross Section for Liquid Water," *Applied Optics*, Vol. 36, No. 12, pp. 2686-2688.
- Favors, R.N., Y. Jiang, Y. L. Loethen and D. Ben-Amotz. 2005. "External Raman Standard for Absolute Intensity and Concentration Measurements." *Review of Scientific Instruments*, Vol. 76. 033108-1.
- Friedel, R. A., and M. Orchin. 1951. *Ultraviolet Spectra of Aromatic Compounds*. John Wiley and Sons. New York.
- Friedrich, D., and W. McClain. 1980. "Two Photon Molecular Electronic Spectroscopy," *Annual Review of Physical Chemistry*, Vol. 31, pp. 559-577.

- Fiocco, G. and L. Smullin. 1963. "Detection of Scattering Layers in the Upper Atmosphere (60–140 km) by Optical Radar," *Nature*, Vol. 199, pp 1275–1276.
- Gardner, C.S., D.C. Senft, and K.H. Kwon. 1988. "Lidar observations of substantial sodium depletion in the summertime Arctic mesosphere," *Nature*, Vol. 332, pp. 142–144.
- Gardiner, D.J., P. Graves, 1989. Practical Raman Spectroscopy, Springer Verlag, Berlin, 1989.
- Gelbwachs, J. and M. Birnbaum. 1973. "Fluorescence of Atmospheric Aerosols and Lidar Implications," *Applied Optics*, Vol. 12, No. 10, pp. 2442–2447.
- Gerrity, D., L. Ziegler, P. Kelly, R. Desiderio and B. Hudson. 1985. "Ultraviolet Resonance Raman Spectroscopy of Benzene Vapor with 220–184 nm Excitation," *The Journal of Chemical Physics*. Vol. 83, No. 7, pp. 3209–3213.
- Graselli, B., 1991. Analytical Raman Spectroscopy. John Wiley and Sons: New York.
- Graselli B., Snavely, and Bulkin, 1981. Chemical Applications of Raman Spectroscopy. John Wiley and Sons, New York
- Grimsditch, M., M. Cardona, J. Callega, F. Meseguer. 1981. "Resonance in the Raman Scattering of CaF₂, SrF₂, BaF₂ and Diamond," *Journal of Raman Spectroscopy*, Vol. 10, pp. 77–81.

- Haas, Y. and S. Zilberg. 1995. "The $\nu_{14}(b_{2u})$ Mode of Benzene in S_0 and S_1 and the Distortive Nature of the π Electron System: Theory and Experiment," *Journal of the American Chemical Society*, Vol. 117. pp. 5387–5388.
- Harmon, P.A., S. A. Asher. 1988. "Differentiation between resonance Raman scattering and single vibrational level fluorescence 5100 cm^{-1} above the ${}^1B_{2u}$ origin in benzene vapor by means of excitation profiles. *Journal of Chemical Physics*, Vol. 88, No. 5, March.
- Harrison, G.R., R. Lord, and J. Loofbourow. 1948. Practical Spectroscopy, Prentice–Hall, Englewood Cliffs, New Jersey.
- Herzberg, G., and Teller, E. 1933. *Zhurnal of Physical Chemistry* Vol. B21, pp. 410.
- Hibben, J.H., 1939. The Raman effect and Its Chemical Applications, Reinhold, New York.
- Hippler, J., J. Troe. and H. Wendelken. 1983. "UV Absorption Spectra of Vibrationally Highly Excited Toluene Molecules," *Journal of Chemical Physics*, Vol. 78, No. 9, pp. 5351–5357.
- Hirschfeld, T., 1973. "Remote Spectroscopic analysis of ppm–level air pollutants by Raman spectroscopy." *Applied Physics Letters*. Vol. 22, No.1.
- Hochenbleicher J.G., 1976. "A laboratory study for a resonance Raman lidar system." *Applied Spectroscopy*, Vol. 30, No. 5.
- Hong, H. K. 1977a. "Theory of Resonant Raman Scattering in the Strong Vibronic Coupling Limit—a Green's Function Approach," *Journal of Physical Chemistry*, Vol. 67, No. 2, pp. 801–812.

- Hong, H. K. 1977b. "Theory of Resonant Raman Scattering. III. Toward the Total Synthesis of Molecular Spectra and Raman Excitation Profiles Within the Generalized Vibronic Theory and from an exciton-in-molecule Point of View," *Journal of Physical Chemistry*. Vol. 68, No. 3, pp. 1253–1263.
- Inaba, 1976. Chapter 5: Detection of Atoms and Molecules by Raman Scattering and Resonance Fluorescence in Laser Monitoring of the Atmosphere, E. D. Hinkley, ed. (Springer-Verlag, Berlin)
- Inagaki, T. 1972. "Absorption Spectra of Pure Liquid Benzene in the Ultraviolet," *The Journal of Chemical Physics*. Vol. 57, No. 6, pp. 2526–2530.
- Johnson, C., M. Ludwig and S. Asher. 1986. "Ultraviolet Resonance Raman Characterization of Photochemical Transients of Phenol, Tyrosine, and Tryptophan," *Journal of the American Chemical Society*, Vol. 108, pp. 905–912.
- Kato, Y. and H. Takuma. 1971. "Absolute Measurement of Raman-Scattering Cross Sections of Liquids," *Journal of the Optical Society of America*, Vol. 61, No. 3, pp. 347–350.
- Kato, Y. and H. Takuma. 1971. "Experimental Study on the Wavelength Dependence of the Raman Scattering Cross Section," *The Journal of Chemical Physics*, Vol. 54, No. 12, pp. 5398–5402.
- Kekulé A. 1865. "Sur la constitution des substances aromatiques," *Bulletin de la Societe Chimique de Paris*, Vol. 3. No. 2, pp. 98–110.

- Keller–Rudek, H. and G. Moortgat. 2007. *MPI–Mainz–UV–Vis Spectral Atlas of Gaseous Molecules*. www.atmosphere.mpg.de/spectral-atlas-mainz
- Kistiakowsky, G. and A. Solomon. 1937. “The Ultraviolet Absorption Spectrum of Benzene,” *Journal of Chemical Physics*, Vol. 5, pp. 609–616.
- Knight, D. and W. White. 1989. “Characterization of Diamond Films by Raman Spectroscopy,” *Journal of Material Research*. Vol. 4, No. 2, pp. 385–393.
- Kobayasi, T., and H. Inaba, 1970. “Laser–Raman Radar for Air Pollution Probe,” *Proceedings of the IEEE*, Vol. 58, pp. 1568.
- Koningstein, J. and B. Jakubinek. 1974. “Exciting Frequencies and Depolarization Ratios for Resonance Raman Effects,” *Journal of Raman Spectroscopy*, Vol. 2, pp. 317–324.
- Korenowski, G., L. Ziegler and A. Albrecht. 1978. “Calculations of Resonance Raman Cross Sections in Forbidden Electronic Transitions: Scattering of the 992 cm^{-1} mode in the ${}^1\text{B}_{2u}$ Band of Benzene,” *Journal of Chemical Physics*, Vol. 68, No. 3, pp. 1248–1252.
- Kramers, H. A. and W. Heisenberg, 1925. *Zeitschrift f. Physik*, Vol. 48. No. 15.
- Krasser, W., H. Ervens and A. Fadini. 1980. “Raman Scattering of Benzene and Deuterated Benzene Chemisorbed on Silica–supported Nickel,” *Journal of Raman Spectroscopy*, Vol. 9, No. 2, pp. 80–84.
- Kumar, Y., D. Rao, M. Murthy and M. Krishnaiah. 2007. “Resonance Lidar System for Mesospheric Sodium Measurements,” *Optical Engineering*, Vol. 46, No. 9.
- Lang, DR. L. 1961. Absorption Spectra in the Ultraviolet and Visible Region.

- Academic Press Inc., Publishers New York. 1961 V.1 and V.14
- LaPlant, F. and D. Ben-Amotz. 1995. "Design and Construction of a Microscope-based Raman System," *Review of Scientific Instruments*, Vol. 66, pp. 3537–3544.
- Leite, R. and S. Porto. 1966. "Enhancement of Raman Cross Section in CdS due to Resonant Absorption," *Physical Review Letters*, Vol. 17. No. 1, pp. 10–12.
- Leonard, D.A., 1967. "Observation of Raman Scattering from the Atmosphere using a Pulsed Nitrogen Ultraviolet Laser," *Nature*, Vol. 216, No. 142,
- Levenson, M., Kano, S., 1989. Introduction to Nonlinear Laser Spectroscopy. Academic Press, Inc. New York.
- Lin-Vien, D.; Colthup, N.B.; Fateley, W.B. and Graselli, J.G. 1991, The Handbook of Infrared and Raman Characteristic Frequencies of Organic Molecules. Academic Press: Boston, 1991.
- Long, D., 2001. The Raman Effect: A Unified Treatment of the theory of Raman Scattering by Molecules. John Wiley and Sons, New York.
- Lueck, H., T. Swinney, B. Hudson and D. Friedrich. 1996. "Resonance Raman Studies of Benzene Derivatives with Strong Conjugation: Nitrile Substitution." *Chemical Physics Letters*, Vol. 258, pp. 80–86.
- Maiman, T. H. 1960. "Stimulated Optical Radiation in Ruby." *Nature*, Vol. 187, pp. 493–494
- Matousek, K., Towrie, M., Parker, A.W. 2000. "Fluorescence Suppression in Raman Spectroscopy using a High Performance Picosecond Kerr Gate," *Laser*

Science and Development – Lasers for Science Facility. Central Laser Facility Annual Report.

- Martin, R. and Damen T. 1971. “Breakdown of Selection Rules in Resonance Raman Scattering,” *Physical Review Letters*, Vol. 26, No. 2, pp. 86–88.
- Mayo, D., F. Miller, and R. Hannah. 2004. Course Notes of the Interpretation of the Infrared and Raman Spectra. John Wiley and Sons, New York.
- McCreery, R. 2000. Raman Spectroscopy for Chemical Analysis. John Wiley and Sons. New York.
- McCreery, R. 2008. <http://www.chemistry.ohio-state.edu/~rmccreer/freqcorr/images/toluene.html>. Accessed January 2008.
- Measures, R.M., 1991. Laser Remote Chemical Analysis, in *Chemical Analysis Series Vol. 94*, R.M. Measures, Ed., John Wiley and Sons: New York.
- Measures, R.M., 1984. Laser Remote Sensing: Fundamentals and Applications. John Wiley and Sons. New York.
- Melfi, S. H., J. D. Lawrence, and M. P. McCormick, 1969. “Observation of Raman scattering by water–vapor in the atmosphere,” *Applied Physics Letters*, Vol. 15, pp. 295–297.
- Melfi, S.H., 1972. “Remote measurements of the atmosphere using Raman scattering,” *Applied Optics*, Vol. 11, pp. 1605.
- Melveger, A.J., 1978. Resonance Raman spectroscopy as an analytical tool, The Franklin Institute Press, Philadelphia.
- Meyer–Arendt, J., 1989. Introduction to Classical and Modern Optics. Prentice–Hall.

- Murrell, J. 1963. The Theory of the Electronic Spectra of Organic Molecules. John Wiley and Sons, New York.
- Mysen, B.O., L.W. Finger, D. Virgo and Seifert. 1982. "Curve-fitting of Raman Spectra of Silicate Glasses," *American Mineralogist*, Vol. 67, pp. 686–695.
- National Institute of Advanced Industrial Science and Technology 10/11/2006.
<http://riodb01.ibase.aist.go.jp/sdbs/>.
- National Institute of Standards and Tables. [<http://physics.nist.gov>, accessed January, 2007].
- Nobel Prize Organization. http://nobelprize.org/nobel_prizes/physics/laureates/
- Novitsky, Edward, A. Willitsford, C. R. Philbrick, 2005. "Vertical Profiles of Aerosol and Particulate Matter Obtained from a Multistatic Lidar," *AAAR PM Supersites Conference*, Feb. 7–11, 2005, Atlanta, GA.
- Palafox, M. A., 2000. "Scaling Factors for the Prediction of Vibrational Spectra. I. Benzene Molecule," *Journal of Quantum Chemistry*, Vol. 77. pp. 661– 684.
- Pauling, L. and G. Wheland. 1933. "The Nature of the Chemical Bond. V. The Quantum–Mechanical Calculation of the Resonance Energy of Benzene and Naphthalene and the Hydrocarbon Free Radicals," *Journal of Chemical Physics*. Vol. 1, pp. 362–374.
- Penney, C.M., 1974. "Absolute rotational Raman Cross Section for N₂, O₂, and CO₂," *Journal of the Optical Society of America*, Vol. 64, No. 5.
- Penney, C.M., 1968. "Light Scattering in Terms of Oscillator Strengths and Refractive Indices," *Journal of the Optical Society of America*, Vol. 59. No. 1, pp. 34–42.

- Penney, C.M. and W. Morey. 1973. "Study of Resonance Light Scattering for Remote Optical Probing," Accession Number: 74N20316; Document ID: 19740012203; Report Number: NASA-CR-132363, SRD-73-125
- Philbrick, C.R., Z. Liu, H. Hallen, D. Brown, A. Willitsford. 2006. "Lidar Techniques Applied to Remote Detection of Chemical Species in the Atmosphere," *Proceedings of the International Symposium on Spectral Sensing Research, ISSSR.*
- Philbrick, C. R., Ryan, W. F., Clark, R.D., B. G. Doddridge., 2003 "Advances in Understanding Urban Air Pollution from the NARSTO-NE-OPS Program," *Proceedings of the American Meteorological Society 5th Conference on Atmospheric Chemistry*, (Long Beach, California, Feb.8-12, 6.1, 2003)
- Philbrick, C. R. and K. Mulik 2000. "Application of Raman Lidar to Air Quality Measurements," *Proceedings of the SPIE Conference on Laser Radar Technology and Applications*, pp. 22-33, 2000.
- Philbrick, C.R., D. B. Lysak, Jr., M. O'Brien and D. Harrison 1997. "Lidar Measurements of Atmospheric Properties," in *Proceedings of the Electromagnetic/Electro-Optics Performance Prediction and Products Symposium*, Naval Post Graduate School, Monterey CA, 385-400, June 1997.
- Philbrick, C.R., 1996. "Lidar Atmospheric Profile Sensor (LAPS): A Remote Sensing Prototype," *Proceedings of the 18th Annual Conference on Atmospheric Transmission Models*, 6-8 June 1995, PL-TR-96-2080, Special Report 278, Phillips Laboratory, Hanscom AFB MA 01731, pp. 27.

- Philbrick, C.R., J. Bufton and C. Gardner. 1985. "A Solid State Tunable Laser for Resonance Measurements of Atmospheric Sodium," *Proceedings of Tunable Solid State Lasers for Remote Sensing Conference*, Stanford, CA. October 1–3, pp. 42–46.
- Photons Systems, 2004, "UV Raman spectroscopy: Photon Systems directions and approaches – A discussion of UV Raman spectroscopic applications of Photon Systems deep UV lasers." April 21, 2004.
<http://www.photonsystems.com/sub/about/publications.php>
- Poultney, S., M. Brumfield and J Sivitier, Jr. 1977. "Quantitative Remote Measurements of Pollutants from Stationary Sources using Raman Lidar," *Applied Optics*, Vol. 16. No. 12, pp. 3180–3182.
- Radle, W. F. and C. A. Beck. 1940. "An Experimental Study of Near Ultraviolet Absorption Spectrum of Benzene," *Journal of Chemical Physics*, Vol. 8. No. 7. pp. 507–513.
- Raman, C.V., 1928. "A Change of Wavelength in Light Scattering," *Nature* (London), Vol. 121, pp. 619.
- Raman, C.V. and K. Krishnan. 1928. "A New Type of Secondary Radiation," *Nature* (London), Vol. 121, pp. 501.
- Raman, C.V. and K. Krishnan. 1928. "A Theory of the Optical and Electrical Properties of Liquids," *Proceedings of the Royal Society of London. Series A*, Vol. 117. No. 778. pp. 589–599.

- Raman, C.V. and K. Krishnan. 1929. "The Production of New Radiations by Light Scattering. Part 1," *Proceedings of the Royal Society of London. Series A*, Vol. 122, No. 789, pp. 23–25.
- Rosen, H., P. Robrish, and O. Chamberlain, 1975. "Remote detection of pollutants using resonance Raman scattering." *Applied Optics*, Vol. 14, pp. 2701.
- Ross, P., S. Van Bramer and M. Johnston. 1996. "Ultraviolet Photodissociation of Gas-Phase Alcohols, Amines, and Nitroalkanes," *Applied Spectroscopy*. Vol. 50, No. 5, pp. 608–613.
- Schomacker, K.T., and J.K. Delaney. 1986. "Measurements of the Absolute Raman Cross Sections of Benzene," *Journal of Chemical Physics*. Vol. 85, pp 4240–4247.
- Schrotter, K. T., H. W. Klockner and A. Weber. 1979. Raman Spectroscopy of Gases and Liquids, Topics in Current Physics. Vol. 11, Springer, New York. Chapter 4.
- SDBSWeb : Spectral Database for Organic Compounds
<http://riodb01.ibase.aist.go.jp/sdbs/> (National Institute of Advanced Industrial Science and Technology, 10/11/2006)
- Sedlacek, A.J., 1995. "Remote sensing of the atmosphere by resonance raman Lidar." *Optical Remote Sensing of the Atmosphere Sixth Topical Meeting*, Salt Lake City, Utah, Feb. 6–10.
- Sedlacek, A.J., and C. Chen, 1995. "Remote detection of trace effluents using resonance Raman Spectroscopy." *Safeguard, Safety and Nonproliferation*

Division, Brookhaven National Laboratory.

http://www.osti.gov/bridge/product.biblio.jsp?osti_id=115629

- Sedlacek, A. and C. Finfrock. 2001. "Ultraviolet Raman Spectral Signature Acquisition: UV Raman Spectral Fingerprints," Environmental Sciences Department. Brookhaven National Laboratory. Upton, Long Island, New York. BNL-69453 <http://www.doe.gov/bridge>
- Sension, R., R. Brudzynski, S. Li and B. Hudson. 1991. "Resonance Raman Spectroscopy of the B_{1u} region of Benzene: Analysis in terms of Pseudo-Jahn-Teller Distortion," *Journal of Chemical Physics*, Vol. 96, No. 4, pp. 2617-2628.
- Sension, R., R. Brudzynski and B. Hudson. 1991. "Vacuum Ultraviolet Resonance Raman Studies of the Valence Excited States of Benzene and Benzene- d_6 : The E_{1u} State and a Putative A_{2u} State," *Journal of Chemical Physics*, Vol. 94, No. 2, pp. 873-882.
- Shaik, S., A. Shurki, D. Danovich. and P. Hiberty. 1996. "Origins of the Exalted b_{2u} Frequency in the First Excited State of Benzene," *Journal of the American Chemical Society*, Vol. 118, pp. 666-671.
- Shorygin, P.P., 1947. "Theory of Dispersion Spectroscopy of Vibrational Resonance Raman Scattering (Review) *Zh. Fiz. Khim.* Vol. 21, pp. 1125.
- Skinnger, J. G. and W. G. Nilsen. 1968. "Absolute Raman Scattering Cross-Section Measurement of the 992 cm^{-1} Line of Benzene," *Journal of the Optical Society of America*, Vol. 58, No. 1,

- Smith, E., and G. Dent. 2005. *Modern Raman Spectroscopy: A Practical Approach*. John Wiley and Sons, New York.
- Smullin, L. and G. Fiocco. 1962. "Optical Echoes from the Moon," *Nature*, Vol. 184, pp. 1267.
- Spiro, T.G. 1987. Biological applications of Raman spectroscopy – Volume 2
Resonance Raman Spectra of Polyenes and Aromatics, John Wiley and Son: New York.
- Spiro, T.G. 1977. "Resonance Effects in Vibrational Scattering from Complex Molecules," *Annual Review of Physical Chemistry*. Vol. 28. pp. 501–521.
- Sponer, H., G. Nordheim, A. Sklar, and E. Teller. 1939. "Analysis of the Near Ultraviolet Electronic Transition of Benzene," *The Journal of Chemical Physics*. Vol. 7, pp. 207–220.
- Strommen, D.P., K. Nakamoto, *Laboratory Raman Spectroscopy*, John Wiley and Sons, New York, 1984.
- Sur, A., J. Knee and P. Johnson. 1982. "The ${}^1B_{2u} \leftarrow \leftarrow {}^1A_{1g}$ Two-Photon Spectra of Several Isotopes of Benzene by Supersonic Beam-Multiphoton Ionization Spectroscopy," *The Journal of Chemical Physics*. Vol. 77, No. 2, pp. 654–668.
- Synge, E.H., 1930. *Philosophical Magazine*. Vol. 9. 1014.
- Tolles, W.M., J.W. Nibler, J.R. McDonald, A.B. Harvey, 1977. "A Review of the Theory and Application of Coherent Anti-Stokes Raman Spectroscopy (CARS), *Applied Spectroscopy*, Vol. 31, No. 4, pp. 253-339.

- Tsu, R., J. Gonzalez and I. Hernandez. 1978. "Observation of the Splitting of the the E_{2g} Mode and Two-Phonon Spectrum in Graphites," *Solid State Communications*, Vol. 27, pp. 507–510.
- Udagawa, Y., N. Mikami, K. Kaya. and M. Ito. 1973. "Absolute Intensity Ratios of Raman Lines of Benzene and Ethylene Derivatives with 5145 Å and 3371 Å Excitation," *Journal of Raman Spectroscopy*. Vol. 1, pp. 341–346.
- Usachev, A., T. Miller, J. Singh, F. Yueh, P. Jang and D. Monts. 2000. "Optical Properties of Gaseous 2,4,6-Trinitrotoluene in the Ultraviolet Region," *Applied Spectroscopy*. Vol. 55 No. 2, pp. 125–129.
- Varsanyi, G., 1969. Vibrational Spectra of Benzene Derivatives. Academic Press, New York.
- Wagner, J., C. Wild and P Koidl. 1989. "Resonant Raman Scattering of Amorphous Carbon and Polycrystalline Diamond Films," *Physical Review B*. Vol. 40, No. 3, pp. 1817–1825.
- Whetten, R., S. Grubb, C. Otis, A. Albrecht and E. Grant. 1985. "Higher Excited States of Benzene: Polarized Ultraviolet Two-Photon Absorption Spectroscopy," *The Journal of Chemical Physics*. Vol. 82, No. 3, pp. 1115–1134.
- Whiffen, D. 1956. "Intensities in the Raman Spectrum of Benzene," *Proceedings of the Physical Society A*, Vol. 69, pp. 375–380.
- Willitsford, Adam, C. T. Chadwick, H. Hallen, C. R. Philbrick "Resonance Raman

- Measurements Utilizing a Tunable Deep UV Source.” *Proceedings of SPIE Defense Security Symposium, 2008. Laser Radar Technology and Applications XIII*.
- Willitsford, Adam, C.R. Philbrick 2005. “Lidar Description of the Evaporative Duct in Ocean Environments,” Proc. SPIE Vol. 5885, *Remote Sensing of the Coastal Oceanic Environment*, pp. 140–147.
- Wilson, E. B. Jr. 1934. “The Normal Modes and Frequencies of Vibration of the Regular Plane Hexagon Model of the Benzene Molecule,” *Physical Review*. Vol. 45, pp. 706–714.
- Wood, R. and G. Collins. 1932. “Raman Spectra of a Series of Normal Alcohols and other Compounds,” *Physical Review*. Vol. 42, pp. 386–393.
- Zgierski, M., M. Pawlikowski and B. Hudson. 1995. “Theory of Resonance Raman Scattering in Benzene Derivatives,” *Journal of Chemical Physics*. Vol. 103, No. 4, pp. 1361–1374.
- Zgierski, M. 1977. “Interference between Resonance and Preresonance Raman Scattering.” *Journal of Raman Spectroscopy*. Vol. 6, No. 1, pp. 53–56.
- Ziegler, L. 1986. “Resonance Rotational Raman Scattering of Symmetric tops: A probe of molecular Photodissociation,” *Journal of Chemical Physics*, Vol. 84, No. 11, pp. 6013–6026.
- Ziegler, L., and B. Hudson. 1981. “Resonance Raman Scattering of Benzene and Benzene-d₆ with 212.8 nm excitation,” *The Journal of Chemical Physics*, Vol. 74, No. 2, pp. 982–992.

Ziegler, L., and B. Hudson. 1980. "The Thermal Blooming Spectrum of Liquid Benzene in the Near Ultraviolet," *The Journal of Chemical Physics*, Vol. 71, No. 1, pp. 113–116.

Ziegler, L., and B. Hudson. 1983. "Vibronic Coupling Activity in the Resonance Raman Spectra of Alkyl Benzenes," *The Journal of Chemical Physics*, Vol. 79, No. 3, pp. 1134–1137.

Zincova, M. *Picture of Green Flash*. San Francisco, CA.

http://mintaka.sdsu.edu/GF/explain/obs_colors.html

APPENDIX A: Picture of C.V. Raman in his laboratory with an optical spectrograph and the first photograph of Stokes and anti-Stokes 'Raman' spectra of liquid benzene when excited with a quartz mercury arc lamp.

[<http://www.photonics.cusat.edu/Article5.html>]






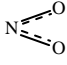
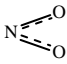




Figure A.1. C.V. Raman and first Raman Spectra

APPENDIX B: Characteristic Raman Scattering Frequencies [Lin-vien *et al.*, 1991]

Molecules with similar bonds may contain similar Raman shifts; below is a summary of the bond type (vibrating group) and the typical range of energy (cm^{-1}) shifts that accompany them.

Table B.1. Characteristic Raman Group Frequencies

Frequency (cm^{-1})	Vibrating Group	Type of Compound
445–550	S—S	aliphatic disulfides
490–522	C—I	aliphatic compounds
510–594	C—Br	aliphatic compounds
570–650	C—Cl	aliphatic compounds
600–700	C—SH	mercaptans
630–705	C—SH	aliphatic compounds
700–1100	C—C	aliphatic compounds
750–850		para derivatives of benzene
884–899		cyclopentane and mono derivatives
939–1005		cyclobutane and derivatives
990–1050		benzene and mono to tri. subst. benzenes
1020–1075	C—O—C	aliphatic compounds
1085–1125	C—OH	aliphatic compounds
1120–1130	C=C=O	aliphatic compounds
1188–1207		cyclopropane and derivatives
~1190	SO ₂	aliphatic compounds
1216–1230	—S=O	aliphatic compounds
~1340		aliphatic compounds
~1380		aliphatic compounds
1380		naphthalene and derivatives
1590–1610		benzene derivatives
1610–1640	N=O	aliphatic compounds
1620–1680	C=C	aliphatic compounds
~1630	C=N	aliphatic compounds
1654–1670	C=N	aliphatic compounds
1650–1820	C=O	aliphatic compounds
1695–1715	C=O	aliphatic compounds
1974–2260	C≡C	aliphatic compounds
2150–2245	C≡N	nitriles

~2570	S—H	aliphatic compounds
2800–3000	C—H	aliphatic compounds
3000–3200	C—H	aliphatic compounds
3150–3650	O—H	aliphatic compounds
3300–3400	N—H	aliphatic compounds
4160	H—H	H ₂

APPENDIX C: ULTRAVIOLET (200–400 nm) - Mercury Vapor Emission Lines and Relative Intensities (NIST-

http://physics.nist.gov/PhysRefData/ASD/lines_form.html)

The low pressure mercury vapor lamp has been extensively studied and the emission lines are shown in Table C.1.

Table C.2. Mercury Vapor Lamp Emission Spectra

Observed Wavelength	Relative Intensity	Observed Wavelength	Relative Intensity
Air (nm)		Air (nm)	
224.755	5	269.938	50
230.206	20	275.278	80
232.32	15	275.971	20
234.057	5	280.346	40
234.543	20	280.443	30
235.248	20	280.534	2
237.832	100	280.677	2
238	20	285.694	50
239.938	40	289.3601	150
239.973	20	292.541	60
240.049	10	296.7283	1200
244.106	5	302.1504	300
244.69	20	302.347	120
246.406	15	302.561	30
248.2	40	302.749	50
248.272	30	312.5674	400
248.382	40	313.1555	320
253.477	90	313.1844	320
253.6521	15000	334.1484	80
256.386	25	365.0158	2800
257.629	25	365.484	300
257.891	5	366.2887	80
262.519	15	366.3284	240
263.978	5	370.144	30
265.204	250	370.417	35
265.369	400	380.166	30
265.513	100	390.187	20
267.491	5	390.637	60
269.883	50		

APPENDIX D: UV Excitation Laser – Optical Parametric Oscillator (OPO)

The excitation laser used for the resonance Raman experiments was a Type-1 OPO from U-Oplaz, and is discussed in detail within Chapter 5. The schematic of the complete laser setup is shown in Figure D.1. The OPO cavity was pumped with the third harmonic of the Spectra Physics INDI Nd:YAG laser seen in Figure D.2. The pump laser at 354.7 nm had a 10 Hz repetition rate and a 7 ns pulse width. The pump beam was reduced in size and coupled into the OPO cavity. Within the OPO laser cavity, the beam was angle-tuned with a β -BBO crystal. The tuning angle of the crystal was used to control the wavelength of the laser output (~430 nm – 710 nm). The output of the OPO cavity was then frequency doubled to generate a tunable UV output (~215 nm – 355 nm). Figure D.3 shows the OPO cavity and frequency doubler for the tunable UV output. Finally four laser beams that are still collinear (pump beam, tunable color, tunable uv, and idler), are separated using a Pellin Broca prism seen in Figure D.4.

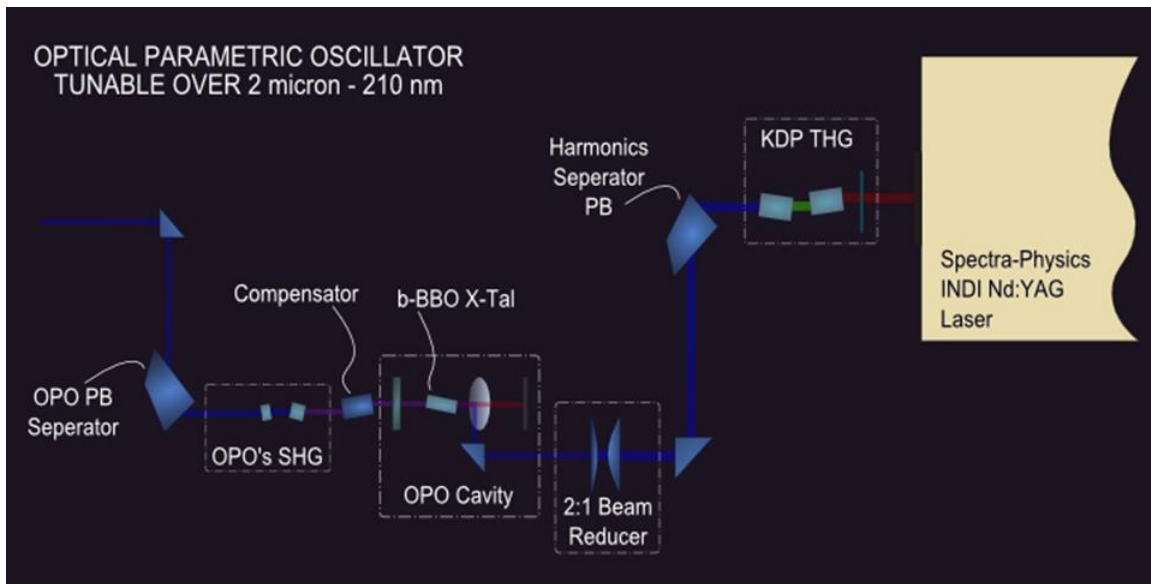


Figure D.1. Overall schematic of UV excitation laser [Chadwick, 2008]

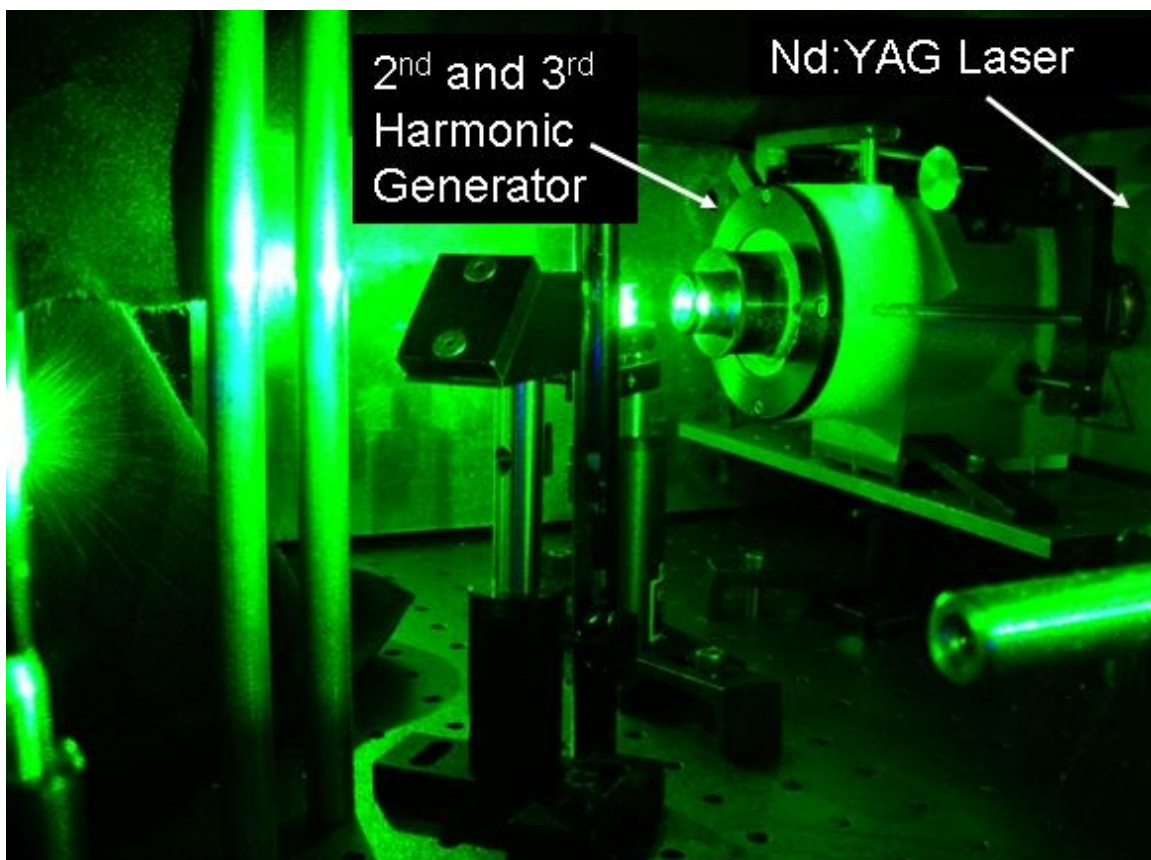


Figure D.2. Spectra Physics Nd:YAG laser with 2nd and 3rd harmonic generator

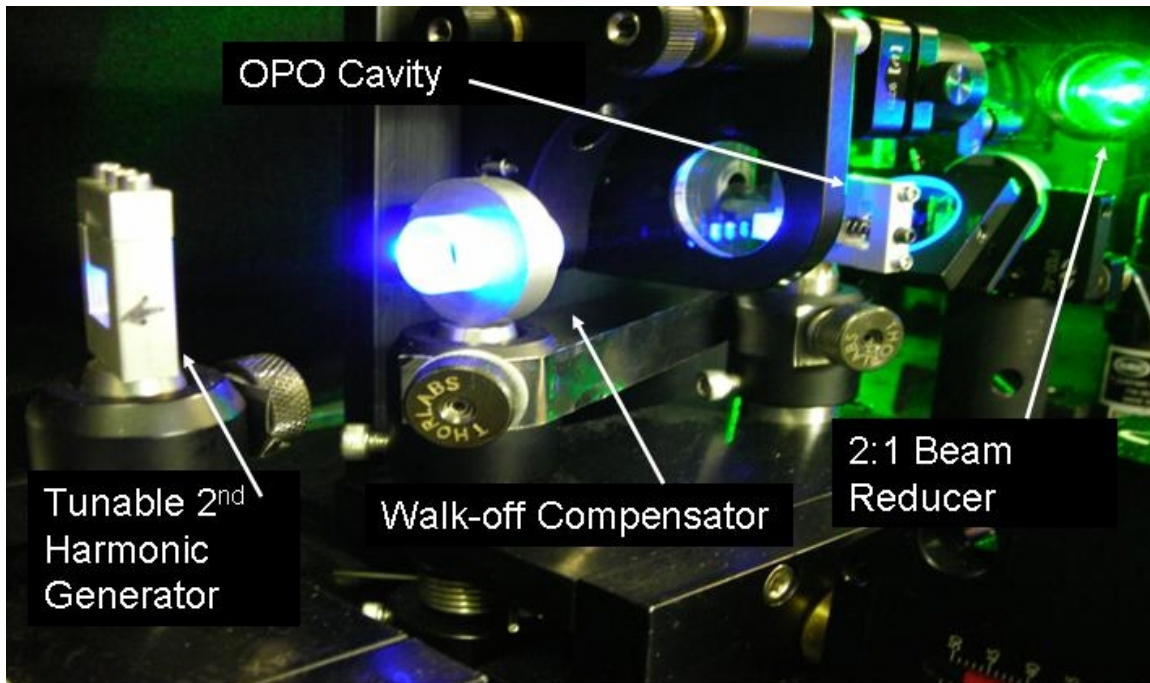


Figure D.3. Optical Parametric Oscillator cavity and tunable 2nd harmonic generator

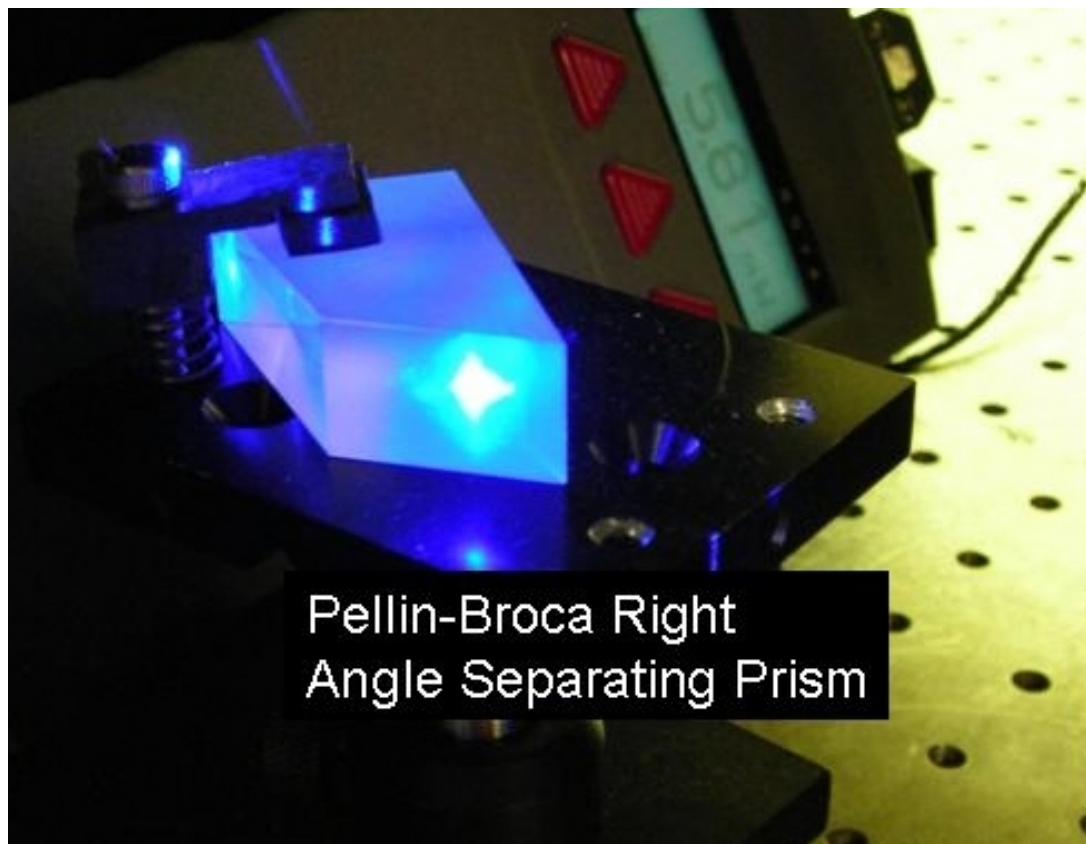


Figure D.4. Pellin-Broca prism

APPENDIX E: Teflon Sample Holders for 90° Raman Scattering Experiment

During the resonance Raman experiments, two different sample holders were used. The first one was made completely of Teflon, and is shown in Figure E.1. The second sample holder was constructed out of Teflon with an aluminum face and is shown in Figure E.2. The first sample holder (Figures E.3 and E.4) constructed completely out of Teflon had windows at both sides allowing absorption measurements by sending a laser straight through the sample. The second sample holder has a larger clear aperture making the 90° Raman scattering experiments easier to perform and yields less stringent requirements on alignment see Figures E.5 and E.6. The sample holders and their specific utilization are discussed in detail within Chapter 5.

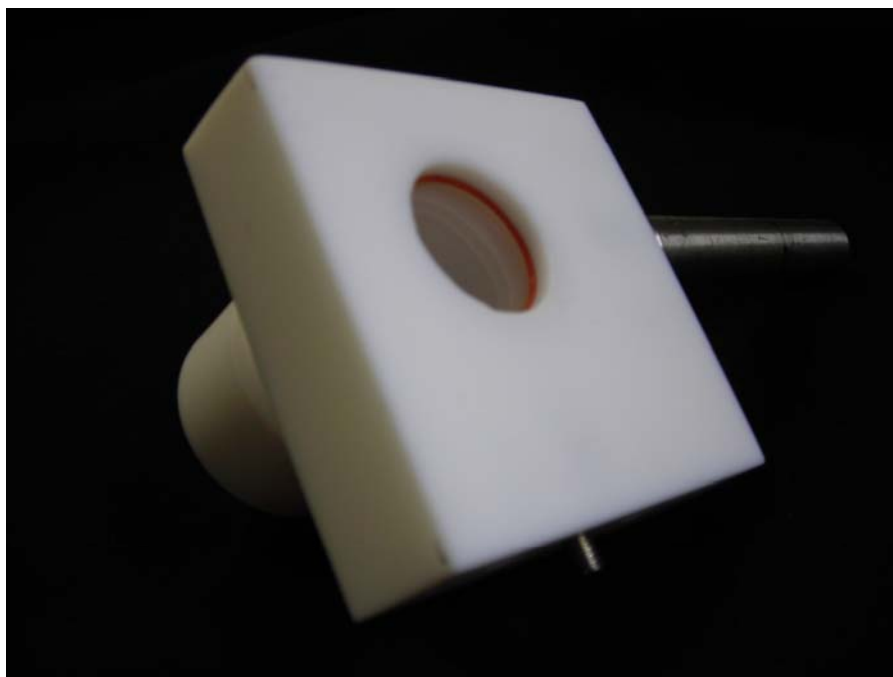


Figure E.1. Teflon sample holder for 90° scattering and absorption measurements



Figure E.2. Teflon sample holder for 90° scattering measurements

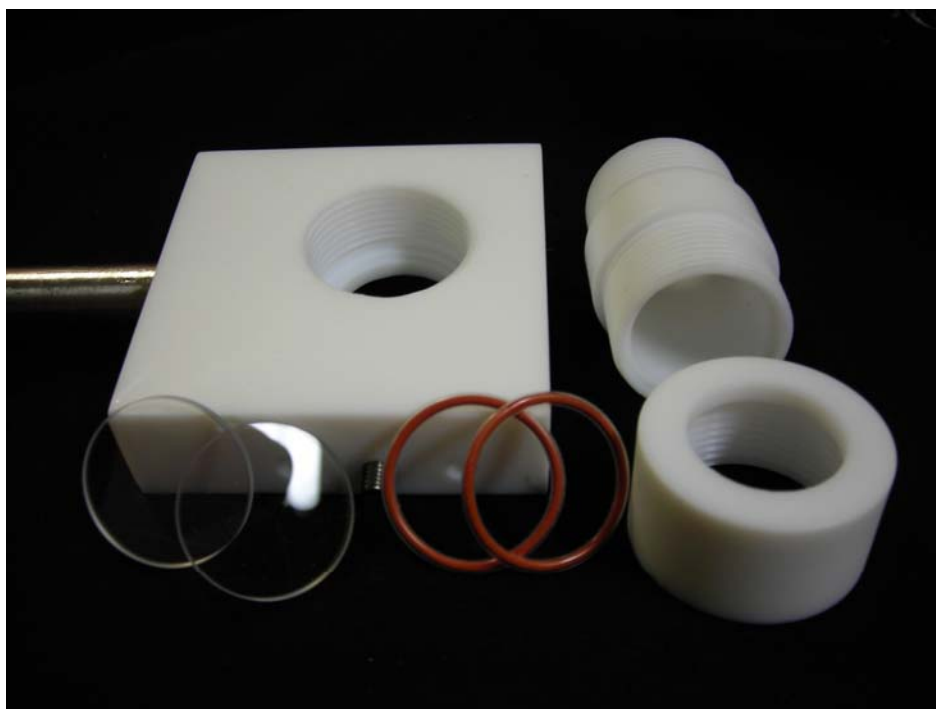


Figure E.3. Breakdown of Teflon sample holder (quartz windows, Teflon O-Rings, Teflon container, and Teflon end caps)



Figure E.4. Close-up of Teflon sample holder with Teflon coated O-ring

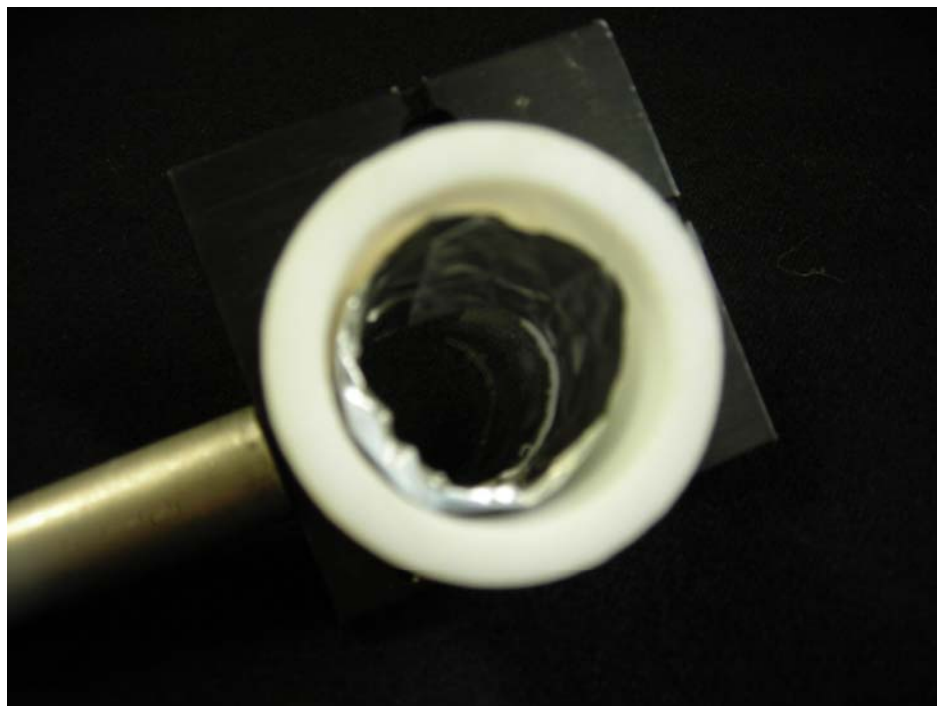


Figure E.5. Close-up of 90° scattering holder with aluminum foil surround and Teflon stopper removed

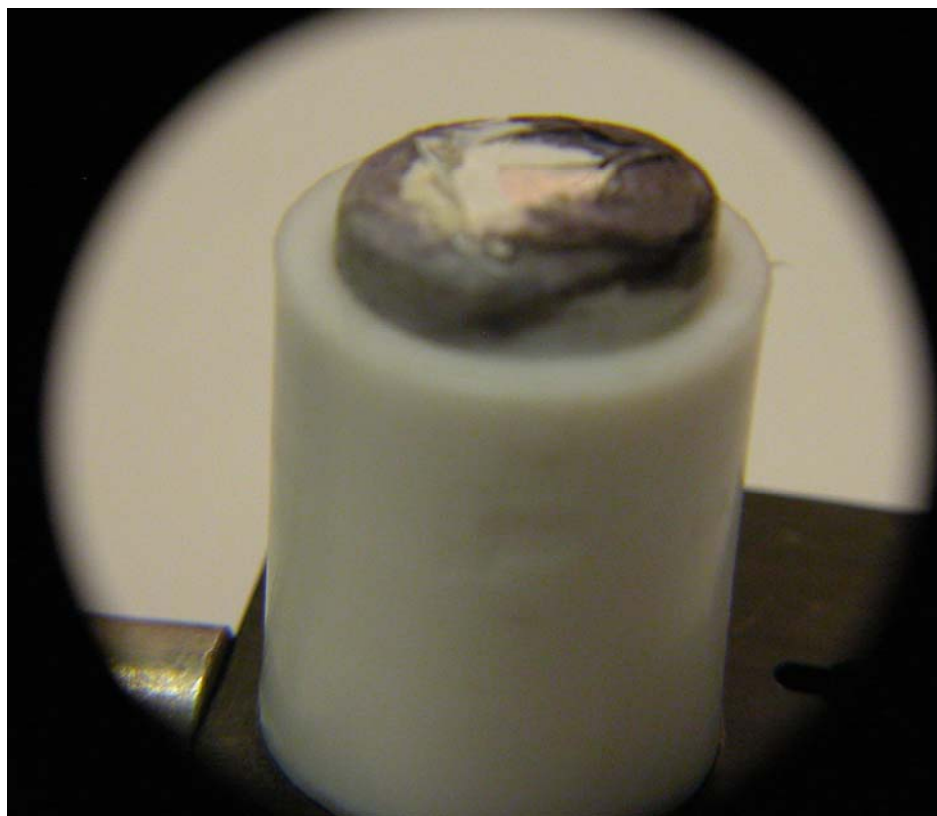


Figure E.6. Teflon holder with stopper

APPENDIX F: MATLAB code for corrections and Noise Reduction.

MATLAB code for reading a '.fits' file and then performing a basic normalization that includes power and wavelength; finally noise removal ('meteor removal'), and signal averaging are provided. MATLAB was chosen as the primary tool with which all data would be processed for a number of reasons:

- (1) MATLAB easily handles large sets of data;
- (2) MATLAB has a large library of built-in functions that have shown their utility to the scientific community;
- (3) Perhaps most importantly the author is well versed in using MATLAB.

The routines shown in Appendix F are used to read in a '.fits' file. The '.fits' files are the raw data files recorded by the Andor EM-CCD camera. The files are read into MATLAB using 'readSpectraSingleAndor.m', and they are subsequently processed by first removing any bad pixels ('spikeRemovalAndorSimple.m'). The data are then averaged and corrected for power variations and wavelength dependence. The resultant data are sent to 'quadPlot.m' for plotting and ease of display. The file names should be of a particular form, e.g., '258.88nm excitation 263.73nm center 1300uW - 2minutes.fits'. This form ensures that all parameters necessary for normalization and plotting are properly accounted for. Files needed for executing the program are readSpectraSingleAndor.m, spikeRemovalAndorSimple.m, setupPlotColors.m, quadPlot.m.

To execute the program, one should have all needed *.fits files in the same directory as the *.m files. The program is run with readSpectraSingleAndor(fileName, power), where the power is the power of the laser in mW.

```

function [correctedData, wn] = readSpectraSingleAndor(fileName,
power)
%reads a single file and displays the colormap as well as the
average lines
%pass power in mw

%parse filename to retrieve useful information
[excitation rem] = strtok(fileName);
[junk rem] = strtok(rem);
[center rem] = strtok(rem);
center = str2num(center(1:end-2));

%read spectra in
A = fitsread(fileName);
data = A;

%removes spikes and averages data
[averageData, compressedImage] = spikeRemovalAndorSimple(data);

[rows columns] = size(compressedImage);
averageData = sum(compressedImage)./rows;

%-----normalize data-----
-%
%normalize for power (power should be in mW)
modified = averageData./power;
normData = averageData./power;

%correct for wavelength
wl = str2num(excitation(1:end-2));
correctedData = modified .* wl^4;
normData = normData .* wl^4;
%%%%%%%%%%%%%%%%%%%%%%%%%%%%%%%%%%%%%%%%%%%%%%%%%%%%%%%%%%%%%%%%%%%%%%%%
%%

%%%%%%%%%%%%%%%%%%%%%%%%%%%%%%%%%%%%%%%%%%%%%%%%%%%%%%%%%%%%%%%%%%%%%%%%
%%
%-----setup wavelength/wavenumber range for plotting-----
-%
start = center - 2.844;
stop = center + 2.844;
wavelengths = linspace(start, stop, 512);
exwavenumbers = (str2num(excitation(1:end-2))* 10^-7)^-1;
leftWavelength = ((center - 2.844));
rightWavelength = ((center + 2.844));
wl = linspace(leftWavelength, rightWavelength, 512);
wn = (wl.*10^-7).^ -1;
wn = exwavenumbers - wn;
%%%%%%%%%%%%%%%%%%%%%%%%%%%%%%%%%%%%%%%%%%%%%%%%%%%%%%%%%%%%%%%%%%%%%%%%
%%

%plot 4 plots on 1 (image, compressed image, averageData)
quadPlot(normData, correctedData, A, compressedImage, excitation,
num2str(center), wn, 0, 1);

```

MATLAB file for spike and 'meteor' removal

```

function [averageData, compressedImage] =
spikeRemovalAndorSimple(data)
%compressedImage is the image with the 'meteors' removed
%data to average is the average data with meteor rows removed.

[rows columns] = size(data); %use size to determine how far to step
through matrix
badrows = zeros(1,columns); %setup dummy matrix in order to easily
retrieve bad row.

m = 1;
n = 1;
index = 1;

while( m < rows + 1)
    while( n < columns + 1)
        if (abs(data(m,n)) > 10000) %step through each row and
column, if value is above 10000
            %remove point, saturated due to 'meteor', this value may
            %change depending on camera behavior.
            badrows(m) = 1;

            end
            n = n + 1;
        end
        n = 1;
        m = m +1;
    end

m = 1;
count = 0;
dataToAverage = zeros(1,columns);
compressedData = [];
n = 1;
while(m < rows + 1)

    if(badrows(m) ~= 1) %if badrows is not equal to 1 then we have
a good row and use for average
        dataToAverage = dataToAverage + data(m,:);
        count = count + 1;
        compressedData(n,:) = data(m,:);
        n = n + 1;
    end
    m = m + 1;
end

compressedImage = compressedData;
averageData = dataToAverage./count;

```

MATLAB file for plotting 4 plots on 1, to compare noise removal with original.

```
function quadPlot(averageData, modified, colorMapOriginal,
colorMapFix, excitation, center, wavelengths, wlorwn, log)

figure

%plots original colormap
h = subplot(4,1,1);
pcolor(wavelengths, 1:512, colorMapOriginal);
shading interp
caxis([0 1000]);
xlim([wavelengths(1), wavelengths(end)]);
title(['Raman Scatter of Benzene with ' excitation], 'FontSize',
18);

[row column] = size(colorMapFix);
%plots the compressedImage ('meteor removal') colormap
subplot(4,1,2)
pcolor(wavelengths, 1:row, colorMapFix);
shading interp
caxis([0 1000]);
xlim([wavelengths(1), wavelengths(end)]);

%plots the average in either a linear or log scale
subplot(4,1,3)
if(log == 1)
    semilogy(wavelengths, averageData);
else
    plot(wavelengths, averageData);
end
xlim([wavelengths(1), wavelengths(end)]);
set(gca, 'XGrid', 'on');
set(gca, 'XMinorgrid', 'on');

%plots the final fixed average
subplot(4,1,4)
plot(wavelengths, modified);
xlim([wavelengths(1), wavelengths(end)]);
set(gca, 'XGrid', 'on');
set(gca, 'XMinorgrid', 'on');
if(wlorwn == 1)
    xlabel('Raman Scatter Wavelength nm', 'FontSize', 14);
else
    xlabel(['Raman Shift from ' excitation ' cm^-1'], 'FontSize',
14);
end
```

APPENDIX G: MATLAB Code for the reading, normalization, and stitching of multiple files together in order to display a full Raman spectra ($\sim 4000\text{ cm}^{-1}$).

The following routines are used to search all files in the directory and stitch together the spectra. After stitching and normalization is complete the spectra are plotted. If more than one excitation wavelength is in the directory, then they will also be stitched and plotted on the same plot with different color schemes. The file names should be of a particular form e.g. '258.88nm excitation 263.73nm center 1300uW - 2minutes.fits' This form ensures that all parameters necessary for normalization and plotting are properly accounted for.

Files needed are multiPlotStitch.m, getFilesStitch.m, readSpectraSingleAndor.m, redundantPointsRemoval.m, spikeRemovalAndorSimple.m, setupPlotColors.m, slidingavg.m.

To execute the program, one needs to have all *.fits files in the same directory as the *.m files. The multiPlotStitch(offset, material) is run with offset equal to 1 if one wants to offset the spectra for easier viewing, and the material is a Raman scattering medium such as benzene, toluene, diamond.


```

function multiPlotStitch(offset, material)
%offset ==1 then offset otherwise on top
%note any text behind a '%' are comments and are not executed in

Matlab (this text also appears green)

a = dir;

m = 1;
check =1;
handles = [];
prnLambdas = [];
plotData = [];
highestWavelengthSeen = 0;
lambda = [];
[stop junk] = size(a);

count = 0;
n =1;
%get a count for number of files with different excitation
wavelengths
while(m < stop+1)
    fileName = a(m).name;
    [tok1 rem] = strtok(fileName);
    [j k] = size(tok1);

    if(k > 3)
        if(tok1(end-1:end) == 'nm') %if last 2 characters are 'nm'
then file
            if(str2num(tok1(1:end-2)) > highestWavelengthSeen) %want
to count each excitation wavelength %once
                highestWavelengthSeen = str2num(tok1(1:end-2));
                lambda(n) = str2num(tok1(1:end-2));
                count = count + 1;
                n = n + 1;
            end
        end
    end
    m = m + 1;
end
m=1;

[red green blue] = setupPlotColors(count);
colorNumber = 1;

figure
axes('FontSize', 10);
while(m < count+1)
    [wnnew datanew] = getFilesStitch(lambda(m));
    wn = wnnew;
    data = datanew;

```

```

excitationWavelength = num2str(lambda(m));
    if(offset ==1)

        h = plot(wn, data + 0.2*(count-colorNumber)*10^12,
'Color', [red(colorNumber)...
          green(colorNumber) blue(colorNumber)],
'LineWidth', 2);
    else
        h = plot(wn, data, 'Color', [red(colorNumber)...
          green(colorNumber) blue(colorNumber)],
'LineWidth', 2);
    end

    plotData(colorNumber).data = data;
    plotData(colorNumber).wn = wn;

    colorNumber = colorNumber + 1;
    hold on

    handles = [handles h];
    if(check == 1) %first time through loop
        prnLambdas = [num2str(excitationWavelength) 'nm'];
        check = 2;
    else %setup plot handles
        prnLambdas = char( prnLambdas,
[num2str(excitationWavelength) 'nm'] );
    end

    m = m + 1;
end

%plot labels
title(['Raman Scatter on ' material], 'FontSize',24);
xlabel('Raman Shift [wavenumbers] from excitation
wavelength','FontSize',14);
ylabel('Intensity Arbitrary Units','FontSize',14);
xlim([wn(1) wn(end)]);
legend(handles, prnLambdas);
set(gca, 'XGrid', 'on');
set(gca, 'XMinorgrid', 'on');

```

```

function [wnnew datanew] = getFilesStitch(wavelength)

a = dir;

m = 1;
check =1;
handles = [];
prnLambdas = [];
plotData = [];
datanew = [];
wnnew = [];
[stop junk] = size(a);
z=1;
while(m < stop+1)
    fileName = a(m).name;
    [tok1 rem] = strtok(fileName);

    [j k] = size(tok1);
    if(k > 3)
        if(tok1(end-1:end) == 'nm') %then we have a file we want to
process otherwise move to the next one.
            if(str2num(tok1(1:end-2)) == wavelength)

                fileName
                [excitationWavelength rem] = strtok(fileName);
                excitationWavelength =
str2num(excitationWavelength(1:end-2)); %remove nm label

                [junk rem] = strtok(rem);
                [centerWavelength rem] = strtok(rem);
                centerWavelength = str2num(centerWavelength(1:end-
2)); %remove nm label

                [junk rem] = strtok(rem);
                [power rem] = strtok(rem); %power is in uw

                power = str2num(power(1:4))/1000; %convert to mW

                %all normalization and noise removal is done in
readSpectraSingleAndor
                %background correction, power correction, wavelength
correction
                %and noise removal.
                [data wn] = readSpectraSingleAndor(fileName, power);

                if(z > 1)
                    [data wn] = redundantPointsRemoval(datanew,
wnnew, data, wn);
                end
                datanew = data;
                wnnew = wn;

                z = z + 1;
            end
        end
    end
end

```

```
        end
    end

    m = m + 1;
end

%datanew = slidingavg(datanew, 10);
[rows columns] = size(datanew);
background = sum(datanew(1:99))/100; %region used for background
reduction will depend on image
datanew = datanew - background;
datanew = slidingavg(datanew,10);
```



```
function [data wn] = redundantPointsRemoval(data1, wn1, data2, wn2)

%%dumps first points in next image...
indices = find( (wn1(end) - wn2) > 0);
if(~isempty(indices))
    firstpoint = indices(end);
    data = [data1 data2(firstpoint+1:end)];
    wn = [wn1 wn2(firstpoint+1:end)];
else
    data = [data1 data2];
    wn = [wn1 wn2];
end

%filters last points in previous image (fixes right side drop due to
%filter
% indices = find( (wn2(1) - wn1) < 0);
% if(~isempty(indices))
%     firstpoint = indices(1);
%     data = [data1(1:firstpoint) data2];
%     wn = [wn1(1:firstpoint) wn2];
% else
%     data = [data1 data2];
%     wn = [wn1 wn2];
% end
```

```

function [averageData, compressedImage] =
spikeRemovalAndorSimple(data)

[rows columns] = size(data);
badrows = zeros(1,columns);

m = 1;
n = 1;
index = 1;

average = sum(data)./rows;

while( m < rows + 1)
while( n < columns + 1)
    if (abs(data(m,n)) > 10000) %removes any points with values
above 10000
        badrows(m) = 1;          %this value may change
depending on intensity of saturated pixels
    end
    n = n + 1;
end
n = 1;
m = m + 1;
end
m = 1;
count = 0;
dataToAverage = zeros(1,columns);
compressedData = [];
n = 1;
while(m < rows + 1)

    if(badrows(m) ~= 1) %go back through and eliminate the found
saturated pixels and the entire row
        %due to bleed through.
        dataToAverage = dataToAverage + data(m,:);
        count = count + 1;
        compressedData(n,:) = data(m,:);
        n = n + 1;
    end
    m = m + 1;
end

compressedImage = compressedData;
averageData = dataToAverage./count;

```

```
function [r g b] = setupPlotColors(size);  
%sets up a rainbow plot scale making it easier to see the change in  
the  
%Raman spectra as the excitation wavelength is changed  
  
H = linspace(.75,0,size);  
S = linspace(1,1,size);  
V = linspace(1,1,size);  
  
k = 1;  
while(k < size+1)  
    [r(k) g(k) b(k)] = hsv2rgb([H(k) S(k) V(k)]);  
    k = k+1;  
end
```



```

function out = slidingavg(in, N)
%   OUTPUT_ARRAY = SLIDINGAVG(INPUT_ARRAY, N)
%
%   The function 'slidingavg' implements a one-dimensional filtering,
%   applying a sliding window to a sequence. Such filtering replaces the
%   center value in
%   the window with the average value of all the points within the
%   window. When the sliding window is exceeding the lower or upper
%   boundaries of the input
%   vector INPUT_ARRAY, the average is computed among the available
%   points. Indicating with nx the length of the the input sequence, we
%   note that for values
%   of N larger or equal to 2*(nx - 1), each value of the output data
%   array are identical and equal to mean(in).
%
%   * The input argument INPUT_ARRAY is the numerical data array to
%   be processed.
%   * The input argument N is the number of neighboring data points
%   to average over for each point of IN.
%
%   * The output argument OUTPUT_ARRAY is the output data array.
%
%   © 2002 - Michele Giugliano, PhD and Maura Arsiero
%   (Bern, Friday July 5th, 2002 - 21:10)
%   (http://www.giugliano.info) (bug-reports to
michele@giugliano.info)
%   Taken from Matlab file Exchange AHW
%   Two simple examples with second- and third-order filters are
%   slidingavg([4 3 5 2 8 9 1],2)
%   ans =
%   3.5000  4.0000  3.3333  5.0000  6.3333  6.0000  5.0000
%
%   slidingavg([4 3 5 2 8 9 1],3)
%   ans =
%   3.5000  4.0000  3.3333  5.0000  6.3333  6.0000  5.0000
%
if (isempty(in)) | (N<=0)
% If the input array is empty or N %is non-positive,
disp(sprintf('SlidingAvg: (Error) empty input data or N null.'));
% an error is reported to the %standard output and the
return;
% execution of the routine is %stopped.
end % if

if (N==1)
% If the number of neighbouring %points over which the sliding
out = in;
% average will be performed is '1', %then no average actually occur
and
return;
% OUTPUT_ARRAY will be the copy of %INPUT_ARRAY and the execution of
the routine
end % if
% is stopped.

```

```

nx = length(in); % The length of the input data
structure is acquired to later evaluate the %'mean' over the
appropriate boundaries.

if (N>=(2*(nx-1)))
% If the number of neighbouring %points over which the sliding
out = mean(in)*ones(size(in));
% average will be performed is large %enough, then the average
actually covers all the points
return;
% of INPUT_ARRAY, for each index of %OUTPUT_ARRAY and some CPU time
can be gained by such an approach.
end % if
% The execution of the routine is %stopped.

out = zeros(size(in)); % In all the other situations, the
initialization of the output data %structure is performed.

if rem(N,2)~=1 % When N is even, then we proceed in
taking the half of it:
m = N/2; % m = N / 2.
else % Otherwise (N >= 3, N odd), N-1 is
even ( N-1 >= 2) and we proceed taking %the half of it:
m = (N-1)/2; % m = (N-1) / 2.
end % if

for i=1:nx, % For
each element (i-th) contained in the %input numerical array, a check
must be performed:
if ((i-m) < 1) & ((i+m) <= nx) % If not
enough points are available on the %left of the i-th element..
out(i) = mean(in(1:i+m)); % then
we proceed to evaluate the mean from the %first element to the (i +
m)-th.
elseif ((i-m) >= 1) & ((i+m) <= nx) % If
enough points are available on the left %and on the right of the i-
th element..
out(i) = mean(in(i-m:i+m)); % then
we proceed to evaluate the mean on 2*m %elements centered on the i-
th position.
elseif ((i-m) >= 1) & ((i+m) > nx) % If not
enough points are available on the %righth of the i-th element..
out(i) = mean(in(i-m:nx)); % then
we proceed to evaluate the mean from the %element (i - m)-th to the
last one.
elseif ((i-m) < 1) & ((i+m) > nx) % If not
enough points are available on the %left and on the righth of the i-
th element..
out(i) = mean(in(1:nx)); % then
we proceed to evaluate the mean from the %first element to the last.
end % if
end % for i

```

APPENDIX H: Etzkorn absorption Spectra of Benzene from the MPI–Mainz Spectral Atlas.

The vapor-phase absorption spectrum of benzene is shown in the Table H.1. The absorption spectra was recorded by Etkorn *et al.*, 1999, and was retrieved from the *MPI-Mainz-UV-VIS Spectral Atlas of Gaseous Molecules*, www.atmosphere.mpg.de/spectral-atlas-mainz. The data shown in Table H.1 were used in a two-fold manner: first the data were used as a guide to help determine the proper wavelength of excitation, and, secondly they were used to calculate the absorption correction for the resonance gain calculation. A small sampling of the complete dataset is shown.

Table H.1. Benzene Vapor Phase Absorption Cross Section

Benzene Absorption	C₆H₆
Wavelength [nm]	Absorption (cm²/molecule)
235.78879	5.77E-20
235.82768	5.85E-20
235.86657	5.54E-20
235.90547	6.02E-20
235.94436	5.67E-20
235.98325	6.68E-20
236.02214	6.66E-20
236.06103	6.62E-20
236.09992	6.70E-20
236.13882	5.01E-20

APPENDIX I: Etzkorn absorption Spectra of Toluene from the MPI–Mainz Spectral Atlas.

The vapor phase absorption spectrum of toluene is shown in Table I.1. The absorption spectrum was recorded by Etzkorn *et al.*, 1999, and was retrieved from the *MPI-Mainz-UV-VIS Spectral Atlas of Gaseous Molecules*, www.atmosphere.mpg.de/spectral-atlas-mainz. The data shown in Table I.1 were used in a two-fold manner: first the data were used as a guide to help determine the proper wavelength of excitation and, secondly they were used to calculate the absorption correction for the resonance gain calculation. A small sampling of the complete dataset is shown.

Table I.1. Toluene Vapor Phase Absorption Cross Section

Toluene Absorption	C ₇ H ₈
Wavelength [nm]	Absorption cm ² /molecule
250.452275	4.30E-20
250.4912	3.92E-20
250.530125	2.92E-20
250.56905	3.27E-20
250.607975	3.65E-20
250.6469	6.84E-20
250.685825	8.59E-20
250.72475	9.11E-20
250.763675	1.03E-19
250.8026	8.48E-20
250.841525	1.01E-19
250.88045	1.01E-19

APPENDIX J: MATLAB code for absorption correction and gain calculation

The following code is utilized to calculate the absorption correction for resonance gain calculation for both benzene and toluene. The code calculates the effective penetration depth (depth from which scattering occurs) of the excitation laser. As the laser is tuned onto resonance, the increase in absorption limits the scattering volume and, therefore, the number of scatterers. See description in Chapter 7.

The file names should be of a particular form, e.g., '258.88nm excitation 263.73nm center 1300uW - 2minutes.fits' This form ensures that all parameters necessary for normalization and plotting are properly included.

Files needed: absorptionCorrectionBenzene.m, absorptionCorrectionToluene.m, gain.m, weightingFactor.m, benzene-absorption.mat (see appendix H), toluene-absorption.mat (see appendix I).

To Execute: run either absorptionCorrectionBenzene.m or absorptionCorrectionToluene.m, where wl is the wavelength of excitation in nm, distance is the depth of focus for the lens system, wnshift is the shift of the Raman line in wavenumbers, and Molarity is the molar concentration of either benzene or toluene.

Absorption correction: the retrieval of the absorption coefficients for benzene

```

function [alphaExcitation, alphaRaman] =
absorptionCorrectionBenzene(wl, distance, wnshift, Molarity)
%e.g. wl = 259, distance = 0.01, wnshift = 995, Molarity = 11.25
%valid for wavelengths from 235nm to 270nm
%distance should be in m
%wavelength in nm
%wn shift in 1/cm
%Molarity in Moles/liter
%alphaExcitation is the absorption coefficient at the excited
wavelength
%alphaRaman is the absorption coefficient at the Raman scattered
wavelength

distance = distance*100; %convert to cm

NA = 6.02e23; %Avogadros #
numberDensityLiquid = Molarity * NA /1000; %1000cm^3 in 1 liter;

%numberDensityLiquid = 6.781*10^21; %molecules/cm^3
%from liquid benzene density 0.8786g/cm^3
%molecular mass = 78gram

load benzene-absorption.mat
%the absorption of Benzene can be found in Appendix E of this Thesis
%loads wavelengths and absorption for benzene
%from Etzkorn Atmos. Environ. 33 (1999) 525
%optical measurements at room temperature
%from the Hannelore Keller-Rudek, Geert K. Moortgat,
%      MPI - Mainz-UV-VIS Spectral Atlas of Gaseous Molecules,
%      www.atmosphere.mpg.de/spectral-atlas-mainz

%%%absorption at excitation wavelength
wlfind = wavelengths - wl;
index = find(wlfind > 0);
absExcitation = ( absorption(index(1)) + absorption(index(1)-1) ) /2;
%take average of 2 points around the wavelength of interest.
%%%-----%%%

%%%absorption at Raman scattered wavelength (self-absorption)
wn = wl2wn(wl);
ramanwn = wn - wnshift;
ramanwl = wn2wl(ramanwn);
wlfind = wavelengths - ramanwl;
index = find(wlfind > 0);
absRaman = ( absorption(index(1)) + absorption(index(1)-1) ) /2; %take
average of 2 points around the wavelength of interest.
%%%-----%%%
%%%in the case of Benzene the self absorption is small

```

```
alphaExcitation = numberDensityLiquid * absExcitation; %alpha is per  
cm.  
alphaRaman = numberDensityLiquid * absRaman; %alpha is per cm
```

Absorption correction: the retrieval of the absorption coefficients for toluene

```

function [alphaExcitation, alphaRaman] =
absorptionCorrectionToluene(wl, distance, wnshift, Molarity)
%e.g. wl = 266.8, distance = 0.01, wnshift = 800 or 1000, Molarity =
9.42
%valid for wavelengths from 235nm to 270nm
%distance should be in m
%wavelength in nm
%wn shift in 1/cm
%Molarity in Moles/liter
%alphaExcitation is the absorption coefficient at the excited
wavelength
%alphaRaman is the absorption coefficient at the Raman scattered
wavelength

distance = distance*100; %convert to cm

NA = 6.02e23; %Avogadros #
numberDensityLiquid = Molarity * NA /1000; %1000cm^3 in 1 liter;

%numberDensityLiquid = 5.6725*10^21; %molecules/cm^3
%from liquid toluene density 0.8669g/cm^3
%molecular mass = 92grams

load toluene-absorption.mat
%the absorption of Toluene can be found in Appendix F of this Thesis
%loads wavelengths and absorption for toluene
%from Etzkorn Atmos. Environ. 33 (1999) 525
%optical measurements at room temperature
%from the Hannelore Keller-Rudek, Geert K. Moortgat,
% MPI - Mainz-UV-VIS Spectral Atlas of Gaseous Molecules,
% www.atmosphere.mpg.de/spectral-atlas-mainz

%%%absorption at excitation wavelength
wlfind = wavelengths - wl;
index = find(wlfind > 0);
absExcitation = ( absorption(index(1)) + absorption(index(1)-1) ) /2;
%take average of 2 points around the wavelength of interest.
%%%%-----%%%%%%%%

%%%absorption at Raman scattered wavelength (self-absorption)
wn = wl2wn(wl);
ramanwn = wn - wnshift;
ramanwl = wn2wl(ramanwn);
wlfind = wavelengths - ramanwl;
index = find(wlfind > 0);
absRaman = ( absorption(index(1)) + absorption(index(1)-1) ) /2; %take
average of 2 points around the wavelength of interest.
%%%%-----%%%%%%%%
%%%%in the case of toluene the self absorption is small

```



```
alphaExcitation = numberDensityLiquid * absExcitation; %alpha is per  
cm.  
alphaRaman = numberDensityLiquid * absRaman; %alpha is per cm
```

Gain calculation: the retrieval of the absorption corrected gain values for benzene and toluene.

By changing the utilized absorption spectra it is possible to calculate the gain for either benzene or toluene e.g. load benzene-absorption.mat or load toluene-absorption.mat

```
function [absorptionOut, gain] = gain(wl, distance, wnshift, Molarity)
%valid for wavelengths from 235nm to 270nm
%distance should be in m
%wavelength in nm
%wn shift in 1/cm
%Molarity in Moles/liter

distance = distance*100; %convert to cm

NA = 6.02e23;
numberDensityLiquid = Molarity * NA /1000 %1000cm^3 in 1 liter;

%numberDensityLiquid = 6.781*10^21; %molecules/cm^3
%from liquid benzene density 0.8786g/cm^3
%molecular mass = 78gram

load benzene-absorption.mat
%load toluene-absorption.mat
%loads wavelengths and absorption for benzene
%from Etzkorn Atmos. Environ. 33 (1999) 525
%optical measurements at room temperature
%Hannelore Keller-Rudek, Geert K. Moortgat,
%MPI-Mainz-UV-VIS Spectral Atlas of Gaseous Molecules,
%www.atmosphere.mpg.de/spectral-atlas-mainz

%%%absorption at excitation wavelength
wlfind = wavelengths - wl;
index = find(wlfind > 0);
absExcitation = ( absorption(index(1)) + absorption(index(1)-1) ) /2
%take average of 2 points around the wavelength of interest.
%%%%-----%%%%%%%%%%

%%%absorption at Raman scattered wavelength (self-absorption)
wn = wl2wn(wl);
ramanwn = wn - wnshift;
ramanwl = wn2wl(ramanwn);
wlfind = wavelengths - ramanwl;
index = find(wlfind > 0);
absRaman = ( absorption(index(1)) + absorption(index(1)-1) ) /2 %take
average of 2 points around the wavelength of interest.
%%%%-----%%%%%%%%%%
%%%in the case of Benzene the self absorption is negligible...

alphaExcitation = numberDensityLiquid * absExcitation %alpha is per cm.
alphaRaman = numberDensityLiquid * absRaman %alpha is per cm
```

```
transmission = exp(-(alphaExcitation + alphaRaman) * distance);  
absorptionOut = 1 - transmission;
```

```
theta = 45; %45 degrees (wrt normal) for 90degree scattering setup  
weight = weightingFactor(theta, alphaRaman, alphaExcitation, distance)  
%distance [cm] and alpha [1/cm]...  
gain = distance / weight;
```

Gain calculation: the retrieval of the absorption corrected weighted line integral

```

function [weight] = weightingFactor(theta, alphaRaman, alphaExcitation,
length)
%for 90 degree scattering setup theta should be 45degrees
%alphaRaman and alphaExcitation are the retrieved alpha coefficients
from the gain function.
%length is the visible depth of penetration 1cm for resonance
experiment

%calculate values for integral...
%           length
%           /  -(alphaExcitation) * x/cos(theta)  -(alphaRaman) *
x/sin(theta)
% weight =  | e                                     e
dx
%           /
%           0
%
theta = deg2rad(theta);

%for x = 0 limit;
lowerLimit = (- cos(theta) * sin(theta)) / (alphaRaman * cos(theta) +
alphaExcitation * sin(theta));

upperLimit = (- exp(-length*(alphaRaman * csc(theta) + alphaExcitation
* sec(theta))) * cos(theta) * sin(theta)) / (alphaRaman * cos(theta) +
alphaExcitation * sin(theta));

weight = upperLimit - lowerLimit;

```

APPENDIX K: Comparison of Herzberg and Wilson vibrational mode labels

The vibrational modes in benzene have been given to common numbering schemes those determined by E. B. Wilson [1934] from Harvard and G. Herzberg from the National Research Council of Canada. The numbering scheme utilized throughout this thesis is that of G. Herzberg.

Table K.3. Benzene mode assignment comparison of Wilson and Herzberg

Comparison of Wilson and Herzberg Notation					
mode	Wilson	Herzberg	cm⁻¹	Allowed	Observed
a _{1g}	v ₂	v ₁	3191	R v.s.	3073.94
a _{1g}	v ₁	v ₂	994.4		993.06
a _{2g}	v ₃	v ₃	1367	Forbidden	Not. Obs
a _{2u}	v ₁₁	v ₄	707	R depol	845 (weak)
b _{2g}	v ₅	v ₇	990	Forbidden	Not. Obs
b _{2g}	v ₄	v ₈	707	Forbidden	Not. Obs (IR-s)
b _{1u}	v ₁₃	v ₅	3174	Forbidden	3059
b _{1u}	v ₁₂	v ₆	1010	Forbidden	Not. Obs
b _{2u}	v ₁₄	v ₉	1177.8	Forbidden	1309.4
b _{2u}	v ₁₅	v ₁₀	1149.7	Forbidden	1149.7
e _{1g}	v ₁₀	v ₁₁	847.1	R depol w	
e _{1u}	v ₂₀	v ₁₂	3181.1	Forbidden	IR Strong
e _{1u}	v ₁₉	v ₁₃	1494	Forbidden	IR Strong
e _{2g}	v ₇	v ₁₅	3174	Forbidden	Not Obs
e _{2g}	v ₈	v ₁₆	1607	R depol m	1591.33
e _{2g}	v ₉	v ₁₇	1177.8	R med	1177.78
e _{2g}	v ₆	v ₁₈	607.8	R depol m	608.13
e _{2u}	v ₁₇	v ₁₉	967	Forbidden	Not Obs
E _{2u}	v ₁₆	v ₂₀	398	Forbidden	405
E _{2g}	v ₁ +v ₆	v ₂ +v ₁₈	1609.52	R Depol m	

Vita

Adam Willitsford was born in Philadelphia, PA, to parents David and Brenda Willitsford. He graduated from Lafayette College Cum Laude in 2002 with a B.S. in Electrical and Computer Engineering and with a minor in Physics. He immediately began graduate school at Penn State University, during which he has worked as a research assistant in the Lidar Lab with Professor C. Russell Philbrick. During graduate school Adam married his wonderful wife, Abigail Stringer, on June 5th, 2004. He is a member of the SPIE and Optical Society of America. Adam is also a member of Eta Kappa Nu Electrical Engineering Honor Society and Tau Beta Pi National Engineering Honor Society. Adam is continuing his life-long learning process at the University of Louisville as a Research Scientist/Engineer. In his free time he enjoys playing soccer and working out at the gym.